

Single-Particle Orbit Tracking

Setup, Characterisation and Application

Der Universität Bayreuth
zur Erlangung des Grades eines
Doktors der Naturwissenschaften (Dr. rer. nat.)
genehmigte Abhandlung

von

Dominique Ernst

geboren am 28. April 1982
in Tirschenreuth

1. Gutachter: Prof. Dr. J. Köhler
2. Gutachter: Prof. Dr. M. Weiss

Tag der Einreichung: 27.09.2012
Tag des Kolloquiums: 14.12.2012

Abstract

Tracking of single nanoobjects (e.g. beads, proteins or molecules) is of fundamental interest in many research fields, particularly in the fields of biophysics and material sciences. Information such as the local viscosity or the structure around the tracer particle can be gathered on the nanometer scale. Further, the photophysical properties or conformational dynamics of the tracer can be studied without the need of immobilising them. Moreover, fundamental research with respect to diffusion processes like the normal Brownian motion or anomalous diffusion can be examined with the acquisition of single-particle trajectories.

In this thesis, the development and experimental realisation of an optical setup which records the 2-dimensional trajectories of single fluorescently labeled polystyrene beads, either 20 nm or 50 nm in diameter, with a high spatial and temporal resolution is introduced. Combining single molecule fluorescence techniques with a new method called *single-particle orbit tracking* the spatial position of the beads could be determined with an accuracy of less than 10 nm at a time resolution of 4 ms. The idea is to manipulate the excitation light spatially and temporally to locate a particle. In order to do so, special optics which deflect a laser beam and guide it on a circular path were used. Subsequently, this rotating beam is projected by a microscope into the sample with the diffusing particles. Due to the spatially and periodically modulated excitation light, the emission signal of the bead is modulated with the frequency of the rotation of the laser focus. The amplitude of the modulated emission signal depends on the position of the particle within the excitation orbit. An ingeniously developed algorithm calculates the position of the particle with respect to the centre of the orbit by demodulating the emission signal and restores the particle back to the orbit centre. Applying this method successively, the trajectory of the diffusing bead can be reconstructed. Besides the experimental realisation, the characterisation of the setup in terms of the spatial and temporal accuracy as well as the experimental shortcomings that influences the measured trajectories and hence, the interpretation of the data, were also the main topics of this work. For this purpose a reference sample of 20 nm sized beads in glycerol was used. The accuracies were studied mainly by computer simulations and the artifacts by experiments. The technical details of the setup and the characterisation results were published (publication P1).

The recorded trajectories were analysed with various methods, among which the commonly used mean squared displacement (MSD) yields the results with highest information. The diffusion coefficient as well as the diffusion behaviour could be quantified. With this method the obtainable accuracy in measuring the diffusion coefficient by the acquisition of single-particle trajectories was studied as a function

of the length of the trajectories and as a function of the number of fitting points that were used for a linear fit to the experimentally determined MSD-curves. As expected, the relative error of the determined diffusion coefficient gets better for longer trajectories. Further, an optimal number of fitting points for the linear approximation to the MSD-curves was found, which yields the most exact values for the diffusion coefficients and which is independent of the trajectory length. For the first time, experimental results on that issue were compared with theoretical predictions, where a good agreement was found. These findings were published (publication P2). By the use of the Stokes-Einstein relation the diffusion coefficients could further be converted to particle radii. A closer examination of these radii emphasises the influence of the afore mentioned number of fitting points. For the optimal value, significantly precise radii could be determined.

Finally, an application of the new setup is presented. In cooperation with the chair of experimental physics I (group of Prof. Dr. M. Weiss) of the University of Bayreuth, the diffusion behaviour of single nanoparticles in a complex fluid was studied. Background hereto is the investigation of biochemical reactions in a biological cell, whose kinetic is given by the diffusion of the corresponding reaction partners. Due to the high crowding of the cell compartments the diffusion is hindered. The diffusion behaviour in these systems is called anomalous and more exactly subdiffusive. Several theoretical models have been developed to explain this phenomenon, but yet without experimental verifications. Here, the diffusion of 50 nm sized polymer beads in the model system dextran (a highly branched biopolysaccharide) is investigated experimentally with high spatial and temporal resolution. The data were analysed in the group of the cooperation partner which yields a very good agreement with the model of “fractional Brownian motion”. These results were also published (publication P3).

A final outlook concerns possible technical advancements of the experimental setup, in particular to measure 3-dimensional trajectories, and several applications at which the tracking of single particles might be helpful for a better understanding of the system of interest.

Kurzdarstellung

Die räumliche Verfolgung einzelner Nanopartikel (z.B. Polystyrolkolloide, Proteine oder Moleküle) ist für viele Forschungsgebiete, vor allem in der Biophysik und den Materialwissenschaften, von großem Interesse. So können unter anderem Informationen über die lokale Viskosität oder über Strukturen in der Umgebung des Teilchens auf einer Nanometerskala gewonnen werden. Weiterhin können die photophysikalischen Eigenschaften oder die Konformationsdynamik der verfolgten Teilchen selbst studiert werden, ohne sie zu immobilisieren. Auch die Grundlagen von Diffusionsprozessen, wie zum Beispiel die Brownsche Bewegung oder anomales Diffusionsverhalten, können durch die Messungen von Trajektorien einzelner Teilchen untersucht werden.

In dieser Dissertation wird die Entwicklung und experimentelle Umsetzung eines optischen Aufbaus zur Messung von zweidimensionalen Trajektorien einzelner fluoreszenzmarkierter Polystyrolbeads mit einem Durchmesser von 20 nm bzw. 50 nm mit hoher räumlicher und zeitlicher Auflösung vorgestellt. Durch die Kombination von Einzelmolekülfluoreszenztechniken mit einer neuartigen Methode mit der englischen Bezeichnung „*single-particle orbit tracking*“ konnte eine räumliche Auflösung in der Positionsbestimmung der Beads von weniger als 10 nm bei einer Zeitauflösung von 4 ms erzielt werden. Die Idee dabei ist, das Anregungslicht räumlich und zeitlich zu manipulieren, um die Position eines Teilchens zu bestimmen. Dazu werden spezielle optische Bauelemente verwendet die einen Laserstrahl auf einen Kegelmantel ablenken. Nachfolgend wird dieser rotierende Laserstrahl mit Hilfe eines Mikroskops in die Probe mit den diffundierenden Teilchen projiziert. Aufgrund der räumlichen und periodischen Modulation des Anregungslichts ist auch das Emissionssignal des Teilchens mit der Frequenz des rotierenden Laserfokus moduliert. Die Amplitude des modulierten Emissionssignals ist von der Teilchenposition innerhalb des Orbits abhängig, welcher durch das fokussierte Anregungslicht erzeugt wird. Ein speziell entwickelter Algorithmus berechnet die Teilchenposition bezüglich des Mittelpunktes des Orbits indem das Emissionssignal demoduliert wird. Anschließend wird das Teilchen um den berechneten Wert zurück in die Mitte des Orbits verschoben. Sukzessive Anwendung dieser Berechnungsmethode liefert die rekonstruierte Trajektorie des Teilchens. Schwerpunkt dieser Arbeit war neben der technischen Realisierung, die Charakterisierung des Aufbaus in Bezug auf die räumliche und zeitliche Auflösung der Trajektorien, sowie auf experimentelle Unzulänglichkeiten, welche die gemessenen Trajektorien und damit auch die Interpretation der Messdaten, beeinflussen. Dazu wurde die Referenzprobe von 20 nm großen Teilchen in Glycerin verwendet. Die erreichbaren Auflösungsgrenzen wurden hauptsächlich durch den Einsatz computergestützter Simulationen verifiziert, wohingegen die Artefakte

experimentell untersucht wurden. Die diesbezüglich erzielten Ergebnisse sowie die technischen Details des Aufbaus wurden veröffentlicht (Publikation P1).

Die aufgenommenen Trajektorien wurden auf verschiedene Weise analysiert, wobei die weitverbreitete Methode des mittleren Verschiebungsquadrats (engl.: mean squared displacement, MSD), Ergebnisse mit dem höchsten Informationsgehalt lieferte. Sowohl der Diffusionskoeffizient als auch das Diffusionsverhalten konnte quantifiziert werden. Mit Hilfe dieser Analyse wurde die erreichbare Genauigkeit von Diffusionskoeffizienten durch Messungen von Einzelteilchentrajektorien in Abhängigkeit der Trajektorienlänge und der Anzahl an Fitpunkten, die für eine lineare Kurvenanpassung an die experimentell bestimmten MSD-Kurven verwendet wurde, untersucht. Die Analyse der Messdaten zeigte erwartungsgemäß, dass der relative Fehler des Diffusionskoeffizienten für längere Trajektorien kleiner ist. Weiterhin wurde eine optimale Anzahl an Fitpunkten für die MSD-Kurvenanpassung gefunden, die unabhängig von der Trajektorienlänge ist und die genauesten Werte für die Diffusionskoeffizienten liefert. Die experimentellen Ergebnisse dieser Untersuchung wurden erstmals mit theoretischen Vorhersagen verglichen, wobei eine gute Übereinstimmung gefunden wurde. Die Resultate wurden veröffentlicht (Publikation P2). Mit Hilfe der Stokes-Einstein Beziehung konnten weiterhin die Diffusionskoeffizienten in Teilchenradien umgerechnet werden. Eine genaue Betrachtung der Radien verdeutlicht den Einfluss der Anzahl an Fitpunkten. Für die optimale Anzahl an Fitpunkten wurden wesentlich präzisere Werte ermittelt.

Als Anwendung des neuen Aufbaus wurde in Kooperation mit dem Lehrstuhl Experimentalphysik I (Arbeitsgruppe von Prof. Dr. M. Weiss) der Universität Bayreuth das Diffusionsverhalten von einzelnen Polystyrolbeads in einer komplexen Flüssigkeit studiert. Hintergrund hierbei ist die Untersuchung biochemischer Reaktionen innerhalb einer biologischen Zelle, deren Kinetik durch die Diffusion der entsprechenden Reaktionspartner gegeben ist. Diese Diffusion ist durch die hohe Dichte an Zellkompartimenten stark eingeschränkt. Man spricht deshalb von einem anomalem Diffusionsverhalten, genauer gesagt von Subdiffusion. Verschiedene theoretische Modelle zur Beschreibung dieses Phänomens wurden entwickelt, wobei eine experimentelle Verifikation noch nicht möglich war. In dieser Arbeit wird die Diffusion von 50 nm großen Polystyrolbeads in dem Modellsystem Dextran (hochverzweigtes Biopolysaccharid) mit hoher räumlicher und zeitlicher Auflösung untersucht. Die Messdaten wurden in der Arbeitsgruppe des Kooperationspartners analysiert und zeigten eine sehr gute Übereinstimmung mit dem Modell „*fractional Brownian motion*“. Die Ergebnisse wurden ebenfalls veröffentlicht (Publikation P3).

Ein abschließender Ausblick befasst sich mit der technischen Weiterentwicklung des experimentellen Aufbaus, speziell mit der Messung 3-dimensionaler Trajektorien, und mit verschiedenen Anwendungsmöglichkeiten, bei denen die Bewegung einzelner Teilchen aufschlussreiche Erkenntnisse liefern können.

Contents

I	Introduction	1
1	Motivation	3
2	Theoretical & experimental background	5
2.1	Theory	5
2.1.1	Diffusion equation	5
2.1.2	Brownian motion	6
2.1.3	Trajectory analysis	8
2.2	Tracking techniques	10
2.2.1	CCD-Tracking	11
2.2.2	Orbit-Tracking	11
2.2.3	Alternative approaches	13
3	Materials	15
3.1	Beads and samples	15
3.2	Sample preparation	17
4	Simulations	19
4.1	General procedure	19
4.2	Spatio-temporal accuracy	22
4.3	Loosing a particle	25
5	The tracking setup	29
5.1	Optics & Hardware	29
5.2	A static particle	30
5.2.1	Simulation	31
5.2.2	Experiment	33
5.3	Artifacts & Corrections	34
6	Single-particle tracking: results & discussion	37
6.1	Analysing diffusion based on single-particle trajectories	38
6.1.1	Mean squared displacement analysis	38
6.1.2	Alternative approaches	42
6.2	Accuracy of diffusion coefficients	47
6.3	Particle sizes	48

6.4 Crowded Fluids	52
7 Outlook	57
Appendix	59
A Program code	59
B Harmonic approximation	61
Bibliography	63
List of publications	69
Danksagung	71
Erklärung	73
II Publications	75
P1. Setup for single-particle orbit tracking: artifacts and corrections	77
P2. Measuring a diffusion coefficient by single-particle tracking: Statistical analysis of experimental mean-squared-displacement curves	90
P3. Fractional Brownian Motion in Crowded Fluids	102

List of abbreviations

The following list of abbreviations summarizes all used parameters and gives an explanation of the symbols.

R	radius of the orbit
ν	frequency of the rotating focus
ω	angular velocity of the rotating focus ($\omega = 2\pi\nu$)
w	full width at half maximum of the focussed laser spot
I_0	maximum emission of a fluorescent particle placed directly in the focal spot
I_b	background emission
S_0	maximum number of emitted photons of a fluorescent particle placed directly in the focal spot
S_b	number of background photons
S_n	theoretical number of emitted photons during the sampling intervall δt
$S_{n,poiss}$	simulated number of emitted photons by the use of a poisson distribution
\bar{I}	mean emission intensity of the fluorescent tracer
x_p, y_p	real x and y coordinates of the particle
x_c, y_c	calculated x and y coordinates of the particle
x_s, y_s	x and y coordinates of the piezo stage
a	radius of the particle
D	diffusion coefficient
k_B	Boltzmann constant
T	temperature, at which the experiments were performed
η	visosity of the used fluids
α	anomaly parameter
n	number of fitting points used for a linear fit to the MSD curves
t	time
τ	lag time
Δt	time resolution of the experiments
Δr	spatial resolution
δt	sampling time of the experiments and the simulations
N_S	number of sampling data points
N	total number of data points of a trajectory
N_{seg}	number of data points of a cut segment
N_{ens}	number of trajectories an ensemble of segments consists of

R_x, R_y	radii of gyration
T	gyration tensor
A	asphericity
E	ergodicity breaking parameter
β	fraction of diffusion coefficients used for the analysis with the cumulative distribution function
MSD	mean squared displacement
CDF	cumulative distribution function
CTRW	continuous time random walk
OD	obstructed diffusion
FBM	fractional Brownian motion

Part I

Introduction

I may not have gone where I intended to go, but I think I have ended up where I needed to be.

Douglas Adams

1 Motivation

Brownian motion is a well known phenomenon that refers to the random jitter-like movement of microscopic particles in a homogenous fluid and is named after the botanist Robert Brown [1] who is known to be the first person who discovered this motion in the year 1827. Originally, the erratic movement of coal dust particles moving in alcohol was found by Jan Ingenhousz in the year 1785. Since he was not able to explain his finding properly, this issue was not pursued further until Brown investigated pollen grains in water under a light microscope, where he saw the random motion of the grains. The first systematic experiments were later performed by Thomas Graham in 1831 [2]. Inspired by this work, the german physicist Adolf Fick developed a continuum theory of diffusion processes in the year 1855 [3]. Finally, it took about 50 years (1906) until Albert Einstein and Marian von Smoluchowski introduced an atomistic theory for this phenomenon [4–6]. Nowadays these groundbreaking findings are exploited to examine various transport processes on a macroscopic as well as on a molecular length scale.

In many branches of research the investigation of diffusion processes is of great interest. For example the mixing behaviour of fluids and gases [7], the processes at the formation of new compounds in condensed matter physics [8] or the transport of vesicles and other cell compartments in a living cell [9] have been studied extensively. Typically, the determination of the involved transport coefficients like the diffusion coefficient is a general approach for characterising such systems. To examine the diffusion in soft matter environments, mostly fluorescence techniques were used. Prominent methods hereto were fluorescence recovery after photobleaching (FRAP) [10] or fluorescence correlation spectroscopy (FCS) [11, 12]. Prerequisite for this methods is the use of fluorescing or fluorescently labeled samples. For non-fluorescing samples, the technique of dynamic light scattering (DLS) is the method of choice to determine diffusional parameters. Nevertheless, all of the mentioned techniques have in common, that they average over an ensemble of diffusing particles. Using FRAP, a subensemble of fluorescent molecules is photodamaged by high excitation power. Due to the diffusion of the remaining intact particles the fluorescence is recovered. This yields the diffusion behaviour, but averaged over many diffusing particles. Using FCS the diffusion coefficient is provided by sequen-

tially averaging over the residence times in the detection volume of individually registered particles. In both methods the detection volume is restricted to the classical diffraction limit of light and moreover, a uniform behaviour of the particles is assumed, where possible size or shape dependencies of the particles were averaged out. Therefore new methods have to be invented which can follow individual nanoobjects and hence reporting their local diffusion properties.

Currently, the afore mentioned approaches were more and more replaced by single-particle tracking (SPT) techniques [13–24]. This newly developed techniques allow to follow the random movements of an individual particle with a high spatial resolution far beyond the diffraction limit of light microscopy together with a high temporal resolution. The biggest advantage of the use of these methods is the prevention of ensemble averaging effects. Local heterogeneities becomes accessible which assists a better understanding of the transport mechanisms at the nanometer scale which are hidden otherwise. Fascinating experiments have been performed, among which the motion of lipids in a biological membrane [25, 26], the diffusion of proteins and quantum dots in several media [27–29], the step like movement of motor proteins along a filament [30], or the infection pathway of a single virus [31] are prominent examples.

In this work, the aim is to study anomalous diffusion in a system that is comparable with the diffusion of proteins in a cell plasma. Among several theoretical models available to describe such a system, an experimental approach to figure out which model fits best is still missing. In order to do so, a sophisticated single-particle tracking setup has to be developed and also to be well characterised using standard samples and simulations.

Beauty is the first test: there is no permanent place in the world for ugly mathematics.

Godfrey Harold Hardy

2 Theoretical & experimental background

In this chapter I will provide the theoretical framework to diffusion processes and introduce experimental realisations for their investigation. The theoretical section treats the diffusion equation and the Langevin equation. While the first one is commonly used for continua, the second one provides a mathematical description for the diffusion process of a single particle, also called Brownian motion or random walk. Moreover, possible methods to analyse the trajectory of a single particle are given. The experimental section is a brief overview about prominent approaches to measure these trajectories. I will mainly focus on the orbit tracking technique, because it is the core part of this thesis.

2.1 Theory

A diffusion process is a transport process, that describes the spatial and temporal evolution of two or more substances with respect to each other. For example, if the concentration of a substance e.g. a gas, a liquid or particles is distributed imbalanced, a flow arises that equals the concentration throughout the whole system. This process is called diffusion. The reason for the dynamic behaviour, seen on a molecular length scale, is the thermal motion of the molecules, which leads to countless collisions and therefore also to forces that push the molecules or particles in a defined direction. Because this force is fluctuating constantly in magnitude and direction, the trajectory of the particles describes a random walk. In this section the basic equations to study diffusion processes and trajectories are introduced.

2.1.1 Diffusion equation

The substantial equation that is used to explain diffusion processes is the diffusion equation [32]. The motion of particles due to diffusion is described by a particle

current density \mathbf{j} , which arises due to a concentration gradient ∇c .

$$\mathbf{j} = -D\nabla c \quad (2.1)$$

This equation is called the first Fickian law. Beside the concentration gradient, the particle current density depends further on the diffusion coefficient D . The latter was developed in the works of Stokes and Einstein [4] and is defined as:

$$D = \frac{k_B T}{6\pi\eta a} \quad (2.2)$$

Here, k_B is the Boltzmann constant, T the temperature of the system, η the viscosity and a the hydrodynamic radius of the diffusing particles. With the use of the continuity equation (2.3)

$$\frac{d}{dt}c + \nabla \mathbf{j} = 0, \quad (2.3)$$

which has its origin in the law of conservation of particles, the diffusion equation is obtained:

$$\frac{\partial}{\partial t}c = D\nabla^2 c \quad (2.4)$$

In this form the diffusion coefficient is regarded as constant. The diffusion equation describes the dynamics of the concentration of particles or molecules. Strictly speaking, this equation holds true for a continuum of particles in an infinite space. To study single particle phenomena, the concentration has to be interpreted as a probability density to find a particle in space. However, in this work the diffusion of single particles is studied by measuring the trajectory of the particle. Hence, in the following the theoretical description of this stochastic motion is introduced.

2.1.2 Brownian motion

At this point it is worth mentioning, that the following theoretical derivations can be found in great detail in the book *An introduction to Dynamics of Colloids* written by J. Dhont [33]. The diffusion of a particle in a static viscous fluid can be understood as a random walk, also called Brownian motion. The mathematical description of such a stochastic process is based on the Langevin equation (eq. (2.5)).

$$m\ddot{\mathbf{r}}(t) = -\gamma\dot{\mathbf{r}}(t) + \mathbf{F}_s(t) \quad (2.5)$$

Here, the vector $\mathbf{r}(t)$ represents the position of a particle with mass m at the time t . The particle, that moves with respect to the liquid, experiences an accelerating force $\mathbf{F}_s(t)$ and a friction force $-\gamma\dot{\mathbf{r}}(t)$ where γ denotes the friction coefficient. For spherical particles with radius a in a fluid with viscosity η the friction coefficient is given by:

$$\gamma = 6\pi\eta a \quad (2.6)$$

The origin of the accelerating force are thermal fluctuations of the liquid molecules and the concomitant collisions with the particle. The force $\mathbf{F}_s(t)$ in equation (2.5) can be separated in a strength parameter K , and a stochastic variable $\boldsymbol{\epsilon}(t)$, representing the random orientation.

$$\mathbf{F}_s(t) = K\boldsymbol{\epsilon}(t) \quad (2.7)$$

The stochastic variable $\boldsymbol{\epsilon}(t)$, also known as white noise, fullfils two conditions. First, it is isotropic in space and second, two consecutive values (forces) in time are uncorrelated, i.e.

$$\langle \boldsymbol{\epsilon}(t) \rangle = 0 \quad (2.8)$$

$$\langle \boldsymbol{\epsilon}(t)\boldsymbol{\epsilon}(t') \rangle = \delta(t - t') \quad (2.9)$$

$$\langle \boldsymbol{\epsilon}(t)^2 \rangle = 1 \quad (2.10)$$

where $\langle \cdot \rangle$ denotes averaging over time or an ensemble. A distinct averaging method will be written as $\langle \cdot \rangle_T$ for time averaging and $\langle \cdot \rangle_E$ for ensemble averaging, respectively. The strength can be calculated from the fluctuation-dissipation-theorem:

$$\langle \mathbf{F}_s(t)\mathbf{F}_s(t') \rangle = K^2 \langle \boldsymbol{\epsilon}(t)\boldsymbol{\epsilon}(t') \rangle \quad (2.11)$$

$$= 2n\gamma k_B T \delta(t - t') \quad (2.12)$$

The fluctuation strength depends on the friction coefficient and the temperature. n is the number of dimensions. Here a 2-dimensional random walk is analysed, i.e. $2n = 4$. Combining equations (2.7) and (2.12) the stochastic force results to:

$$\mathbf{F}_s(t) = \sqrt{4\gamma k_B T} \boldsymbol{\epsilon}(t) \quad (2.13)$$

The total force ($m\ddot{\mathbf{r}}(t)$) is rapidly fluctuating on time scales of 10^{-14} s. Due to the normally relative large mass of the particle, the Brownian motion covers a typical time scale of 10^{-9} s. The system is highly overdamped and we can neglect the left-hand side of equation (2.5). The Langevin equation reduces to:

$$\dot{\mathbf{r}}(t) = \frac{1}{\gamma} \mathbf{F}_s(t) \quad (2.14)$$

Because of the random nature of the force, every realisation of equation 2.14 leads to a new trajectory of the particle.

The Langevin equation provides discrete steps of the particle movement with random orientation, that make up the trajectory. Such a trajectory can be simulated with an iterative Euler method. For a small time step τ the position of the particle at the time $t + \tau$ can be calculated from its position $\mathbf{r}(t)$ at time t by

$$\mathbf{r}(t + \tau) = \mathbf{r}(t) + \dot{\mathbf{r}}(t)\tau. \quad (2.15)$$

Using equations (2.13) and (2.14), this yields

$$\mathbf{r}(t + \tau) = \mathbf{r}(t) + \sqrt{\frac{4k_B T}{\gamma \tau}} \boldsymbol{\epsilon}(t) \tau \quad (2.16)$$

which incorporates an additional factor $1/\sqrt{\tau}$ for a proper description of the movement. This equation describes the Brownian motion of a particle and was applied in this thesis to simulate trajectories using a home-written Matlab program.

2.1.3 Trajectory analysis

In the following I will give an overview on possible methods to analyse a single-particle trajectory. In particular, these are i) the mean squared displacement as a function of a lag time τ (MSD(τ)) [34], ii) the spatial extend and shape, also termed asphericity [35, 36] and iii) the cumulative distribution function (CDF) of squared displacements [37, 38]. All of these methods will be used in section 6 for the analysis of experimental single-particle trajectories.

i) Mean squared displacement. The MSD can be calculated either time-averaged or ensemble-averaged, i.e. $\langle \Delta \mathbf{r}(t)^2 \rangle_T$ or $\langle \Delta \mathbf{r}(t)^2 \rangle_E$. The latter one requires a statistical relevant ensemble of trajectories, while the first one is commonly used for a few single trajectories with a high number of x,y-position pairs and is hence more suited for single-particle tracking experiments. The MSD of a particle after a time step τ is determined according to:

$$\langle \Delta \mathbf{r}(t)^2 \rangle_T = \langle (\mathbf{r}(t + \tau) - \mathbf{r}(t))^2 \rangle_T = \frac{4k_B T}{\gamma} \tau \quad (2.17)$$

Here the equations (2.16) and (2.10) were used to calculate the MSD. With the Stokes-Einstein equation (2.2) and equation (2.6) the diffusion coefficient can be determined.

$$\langle \Delta \mathbf{r}(t)^2 \rangle_T = 4D\tau \quad (2.18)$$

The linear dependence in time holds true for normal (Brownian) diffusion. But, for systems showing anomalous diffusion, the linear dependence breaks down and a power law with a scaling exponent α is introduced [39].

$$\langle \Delta \mathbf{r}(t)^2 \rangle_T = 4\tilde{D}\tau^\alpha \quad (2.19)$$

Here, the diffusion coefficient has to be interpreted as a generalized diffusion coefficient \tilde{D} , that explains the diffusion in the system under investigation. The anomaly parameter α is regarded as a strength for the anomaly and can be used to group the diffusion behaviour. Processes with an exponent $\alpha > 1$ are called superdiffusive

and those with $\alpha < 1$ subdiffusive. Only if $\alpha = 1$ Brownian motion is obtained. This value can be determined easily with logarithmic calculus of equation (2.19).

$$\log \langle \Delta \mathbf{r}(t)^2 \rangle_T = \alpha \log \tau + \log 4\tilde{D} \quad (2.20)$$

The slope represents the scaling exponent, which is obtained by a linear fit to the MSD data points, plotted in a logarithmic scale.

In an experiment only discrete positions are available, i.e. the time-averaged MSD of a single trajectory $\mathbf{r}(t)$ constituting N position determinations, has to be calculated for consecutive lag times $\tau = k\Delta t$ ($k = 1..(N - 1)$) according to

$$MSD_T(\tau) = \langle \Delta \mathbf{r}(k\Delta t)^2 \rangle_T = \frac{1}{N - k} \sum_{n=0}^{N-k} [\mathbf{r}(n\Delta t) - \mathbf{r}((n + k)\Delta t)]^2 \quad (2.21)$$

Here $\langle \cdot \rangle_T$ symbolizes time-averaging over the respective lag time. The alternative ensemble-average calculation is given as follows:

$$MSD_E(\tau) = \langle \Delta \mathbf{r}(k\Delta t)^2 \rangle_E = \frac{1}{N_{ens}} \sum_{m=1}^{N_{ens}} [\mathbf{r}_m(k\Delta t) - \mathbf{r}_m(0)]^2 \quad (2.22)$$

where N_{ens} denotes the number of trajectories the ensemble consists of and $\mathbf{r}_m(0)$ represents the starting position of each trajectory m .

ii) Shape of a trajectory. The average spatial extend of a trajectory can be estimated by the radii of gyration R_x and R_y . Hence, the gyration tensor \mathbf{T} of a 2-dimensional trace has to be calculated [35, 36].

$$T_{ij} = \frac{1}{N} \sum_{n=1}^N (r_i(n\Delta t) - \langle r_i \rangle) (r_j(n\Delta t) - \langle r_j \rangle) \quad (2.23)$$

Here, the indices i, j denote the x- and y-component of a position vector $\mathbf{r}(t)$ and the brackets $\langle r_i \rangle$ represent the corresponding centre of masses for the x-trace and the y-trace.

$$\langle r_{i,j} \rangle = \frac{1}{N} \sum_{n=1}^N r_{i,j}(n\Delta t) \quad (2.24)$$

Diagonalisation of \mathbf{T} yields the eigenvalues, i.e. the squared radii of gyration.

$$\mathbf{T} = \begin{pmatrix} R_x^2 & 0 \\ 0 & R_y^2 \end{pmatrix} \quad (2.25)$$

The eigenvectors defines the orientation of the respective gyration ellipse. The spatial extend of a trajectory changes with the number of data points and the mobility

of the tracer particle. An unambiguous criterion regarding the diffusion behaviour remains elusive.

A more suitable value is the asphericity A , providing a single parameter that determines the shape of a random walk [36].

$$A = \frac{\langle (R_y^2 - R_x^2)^2 \rangle}{\langle (R_y^2 + R_x^2)^2 \rangle} \quad (2.26)$$

The calculation of A requires averaging over a sub-ensemble ($\langle \cdot \rangle$) that can be obtained from cutting the trajectory into consecutive segments with an equal number of positions N_{seg} . For each of the segments, the radii of gyration were calculated (cf. eqn. 2.23 - 2.25) and the asphericity was determined according to equation (2.26). Trivial values for the asphericity are given for a perfect rod-like shape, where one of the radii of gyration is 0, leading to $A = 1$, and for a perfect spheric shape with equal radii, i.e. $A = 0$. For a random walk one finds $A = 4/7$ [35].

iii) Cumulative distribution function. An alternative method to investigate the diffusion process of a single particle is to calculate the (discrete) cumulative distribution function of the squared displacements Δr^2 at a certain lag time τ , i.e. $CDF(\Delta r^2, \tau)$ [37, 38]. In order to do so, the number of squared displacements smaller or equal to a given Δr^2 is counted according to

$$CDF(\Delta r^2, \tau) = \sum_{\Delta r^2(\tau) \leq \Delta r^2} P(\Delta r^2, \tau) \quad (2.27)$$

where $P(\Delta r^2, \tau)$ denotes the empirical distribution of the squared displacements for a lag time τ . This is done consecutively throughout a trajectory until the highest Δr^2 is reached.

2.2 Tracking techniques

Numerous kinds of setups have been invented to follow the 2- and even 3-dimensional motion of single particles [13, 17, 18, 20, 21, 23, 24, 29, 40]. Mostly, fluorescent techniques were used, which requires fluorescent particles. Therefore, either dye molecules, polymer beads that are loaded with dyes, or labeled proteins are possible tracers. For non-fluorescing particles, other microscopy techniques, e.g. dark field microscopy is a possible method. In the early years, simple video microscopy [17] was used to follow the 2-dimensional motion of single lipids and bigger molecules. Further developments leads to high standard CCD-tracking techniques that record the motion of a single particle with a high spatial and temporal resolution [18]. Besides the common CCD-tracking technique, other methods emerged, where the

spatial and temporal resolution as well as the total observation time have been improved further. In this section I will give a brief introduction to the widely used CCD-tracking method, explain the technique of single-particle orbit tracking, which was exploited in this thesis and give finally an overview to some alternative experimental approaches.

2.2.1 CCD-Tracking

Tracking techniques, that use a charged coupled device (CCD) as a detection unit are called CCD-tracking, which is the most wide-spread method for single-particle tracking [13, 17, 18, 20, 23, 29]. The principle is to record successive images of the sample with the moving particles. Each particle in a CCD-image is displayed as a diffraction limited spot, which is typically spread over some 10 pixels on the CCD-chip. A two-dimensional Gaussian fit to the spot is applied, where the centre of this fit gives the actual particle position with an accuracy of better than the classical diffraction limit of light. By doing so successively with all recorded frames, the trajectories of all the particles within the CCD-images are obtained. The advantage of this technique is the relatively simple experimental setup and the high position accuracy that can be obtained. Further, multiple single particles can be tracked simultaneously. Yet, this experimental approach often lacks a high temporal resolution, because the data storage of the images with a high information density is time consuming. At least sophisticated improvements have to be applied to avoid this shortcoming. Not only the time resolution is restricted, also the total observation time is, because the CCD-images need large computer memory. A video of about ten minutes can easily exceed 100 Gigabyte of hard drive space. To circumvent these limitations, other tracking techniques have been invented.

2.2.2 Orbit-Tracking

The basic idea of this method is to focus a laser beam in the focal plane of the sample and let this focal point rotates around a fluorescent particle. By acquiring the emission signal, which is modulated by the frequency of the rotating laser beam, the position of the particle can be traced. By demodulation of this signal the actual particle position can be calculated. Theoretically this approach was studied by Enderlein [41, 42] and successfully implemented by the groups of Gratton [40], Mabuchi [21] and Lamb [43]. In figure 2.1 the principle is shown schematically for two different particle positions (left hand side) with the corresponding emission signals (right hand side). For particles, that move between the centre and the rim of the orbit, the emission signal is periodically modulated as it is depicted in figure 2.1 (right hand side). A high modulation occurs for particles that are apart from the centre of the orbit (see fig. 2.1a), while it gets weak for particles that are close to the centre (see fig. 2.1b). The amplitude of the modulation changes as a function

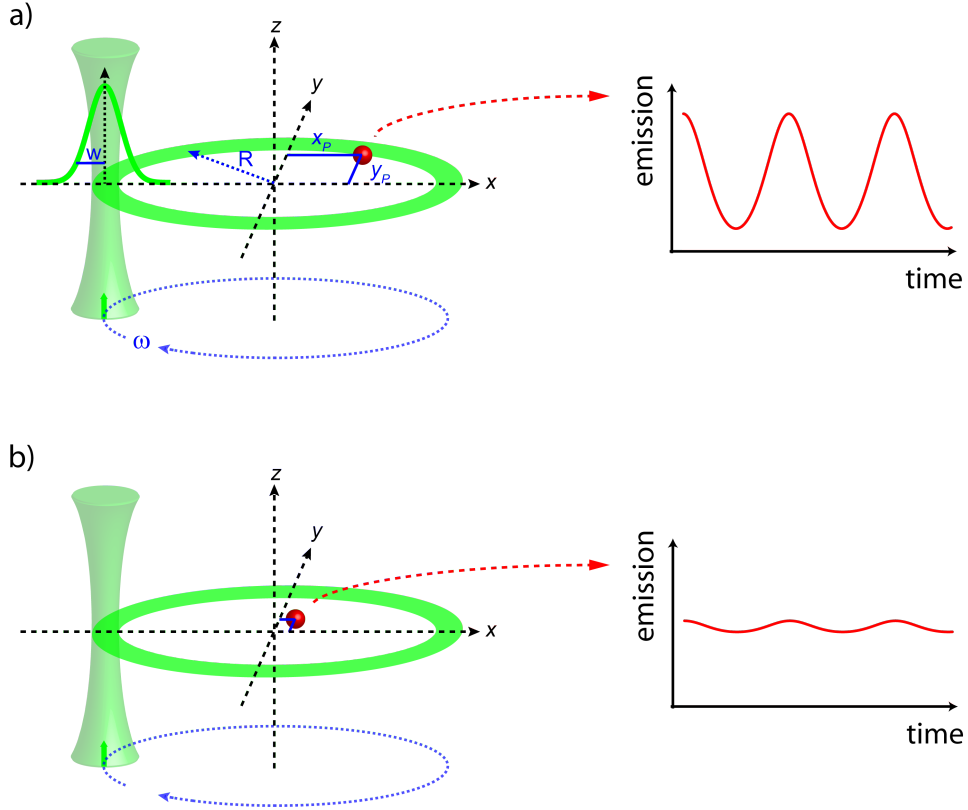


Figure 2.1: Schematic explanation of the orbit tracking technique. All necessary parameters, i.e. the radius of the orbit R , the angular velocity ω , the width of the focus w and the position of the particle x_p and y_p , drawn as a red sphere, are displayed. This scheme is not drawn to scale. In a) the particle is far off-centred, whereas it is close to the centre of the orbit in b). On the right hand side of the figure the corresponding emission intensities of the particle are sketched. Adapted from publication P1.

of the position. Hence, from the demodulation of the emission, the direction as well as the absolute distance from the centre of the orbit can be calculated.

The emission signal $I(t)$ depends on the relative position of the particle (x_p and y_p) and the rotating laser focus and can be written as follows [41, 42]:

$$I(t) = I_0 \exp\left(-\frac{2}{w^2}(x_p - R \cos(\omega t))^2\right) \exp\left(-\frac{2}{w^2}(y_p - R \sin(\omega t))^2\right) + I_b \quad (2.28)$$

Here, I_0 is the maximum emission intensity, i.e. the particle is at the position of the focal spot, R the radius of the orbit, w the $1/e^2$ -width of the laser focus, $\omega = 2\pi\nu$ the angular velocity of the rotating focus and I_b the background intensity. By using lock-in techniques, the position of the particle can be calculated from this emission

signal according to the equations

$$x_p(t) = \frac{w^2 \int_0^T I(t) \cos(\omega t) dt}{2R \int_0^T I(t) dt}, \quad y_p(t) = \frac{w^2 \int_0^T I(t) \sin(\omega t) dt}{2R \int_0^T I(t) dt}. \quad (2.29)$$

The integration boundaries are from 0 (begin of the position determination) to T , which is a time that corresponds to a multiple of the cycling time. Once the position of a particle with respect to the centre of the orbit is calculated, a feedback mechanism has to be implemented, that restores the particle back in the centre of the orbit. Generally, two possibilities exist to do so. On the one hand, this is beam scanning, where the whole light orbit is moved according to the new positions of the particle by applying the corresponding feedback signals to the optical elements that are responsible for the generation of the orbit. This are typically scanning mirrors or acousto optical deflectors. On the other hand, this is sample scanning, where the feedback signals are applied to hardware elements, that move the whole sample, which is mostly realised by a piezostage. The feedback loop is as follows: acquire emission signal, calculate position, restore particle in the centre of the orbit, and so on. Doing so successively, the whole trajectory of a particle can be reconstructed. This new setup for the recording of single-particle trajectories is quite powerful as it combines the spatial accuracy of a CCD camera with the temporal resolution of a single photon detector.

2.2.3 Alternative approaches

In the following some alternative approaches and new developments in the research field of single-particle tracking are introduced. All of them have in common, that they want to push forward the temporal and spatial accuracy of the position determinations.

In the research group of W. E. Moerner two ingenious methods have been invented. The first one is called the ABEL (**A**nti-**B**rownian **E**lectrokinetic) trap [15, 44, 45]. Here, a particle is trapped between four electrodes. As soon as the particle moves towards one of them a voltage to the corresponding electrode is applied that induces a flow field in the medium where the particle is diffusing and which pushes the particle back to the centre of the trap. The feedback mechanism is implemented by recording the motion of the particle with a CCD-camera. In a newer version of this setup, the afore explained orbit tracking is used to record the position of the particle [46], which is faster.

The second setup, that was developed in the group of Moerner modulates the point spread function (PSF) [24, 47]. By a spatial light modulator a double-helix PSF is generated, where the particle of interest is located within that double helix. In other words, a spatial cavity of light surrounds the particle. A movement in any direction is detected by the emission signal of the fluorescent particle. Computer

software is then able to reconstruct the position in three dimensions.

Another method was put forward by the group of H. Yang, in which the emitted light of a particle was split four times by prism mirrors [22]. Each part of the emission was acquired by a separate avalanche photo diode (APD). From the intensity ratios between the four detectors the position of the particle can be extracted. By a 3-dimensional piezostage this motion is compensated. The feedback signal of the piezo is used to determine the trajectory.

In principle all techniques have in common, that they probe the space around a particle, either by trapping the particle, by modulation of the excitation light, or by splitting the emission signal. From the acquired signal of the tracer particles, feedback mechanisms restore the initial position. Successive calculations and the use of sophisticated algorithms provide the reconstructed trajectory.

The good thing about science is that it's true whether or not you believe in it.

Neil deGrasse Tyson

3 Materials

For the characterisation and tracking experiments, two sizes of beads (20 nm and 50 nm) loaded with two different fluorescent dye molecules (nile red and rhodamine) and four kinds of sample substances (poly-vinyl-alcohol (PVA), glycerol, sucrose and dextran) were used. Among these, the combination of 20 nm sized beads in PVA is used for static experiments, where the beads are immobile. Further, another five combinations of beads/samples were used for the characterisation of the setup including the determination of the dynamic accuracies and for the investigation of anomalous diffusion. In the following paragraphs I will describe the characteristics of the beads as well as the preparation of the sample. The detailed preparation of the bead/sample-mixtures for the respective experiments can be found in the corresponding publications (publication P1: 20 nm beads in PVA and in glycerol, publication P2: 20 nm beads in glycerol, publication P3: 50 nm beads in sucrose and dextran).

3.1 Beads and samples

In order to characterise the tracking performance of the experimental setup and to measure diffusion processes, two different sizes of dye labeled beads were used. On the one hand these are 20 nm (diameter) sized polystyrene beads (Molecular Probes) that are loaded with the dye nile red and are further stabilized with carboxylate groups attached to the surface to avoid aggregation. According to the manufacturer, the beads are suspended in water at a concentration of 20 mg/ml. On the other hand these are polystyrene-based latex microspheres (Polysciences) with a diameter of 50 nm, that are labeled with the dye rhodamine. Here, the concentration of the stock solution is 200 mg/ml with no additional stabilizers. The molecular structure as well as the normalized fluorescence excitation and emission spectra of the two highly fluorescent molecules are displayed in fig. 3.1a,b. The spectra have been recorded with a commercial fluorescence spectrometer (Cary Eclipse, Varian). Therefore the respective beads were dissolved in millipore water and this solution was then filled in cuvettes. The fluorescence excitation and emis-

3 Materials

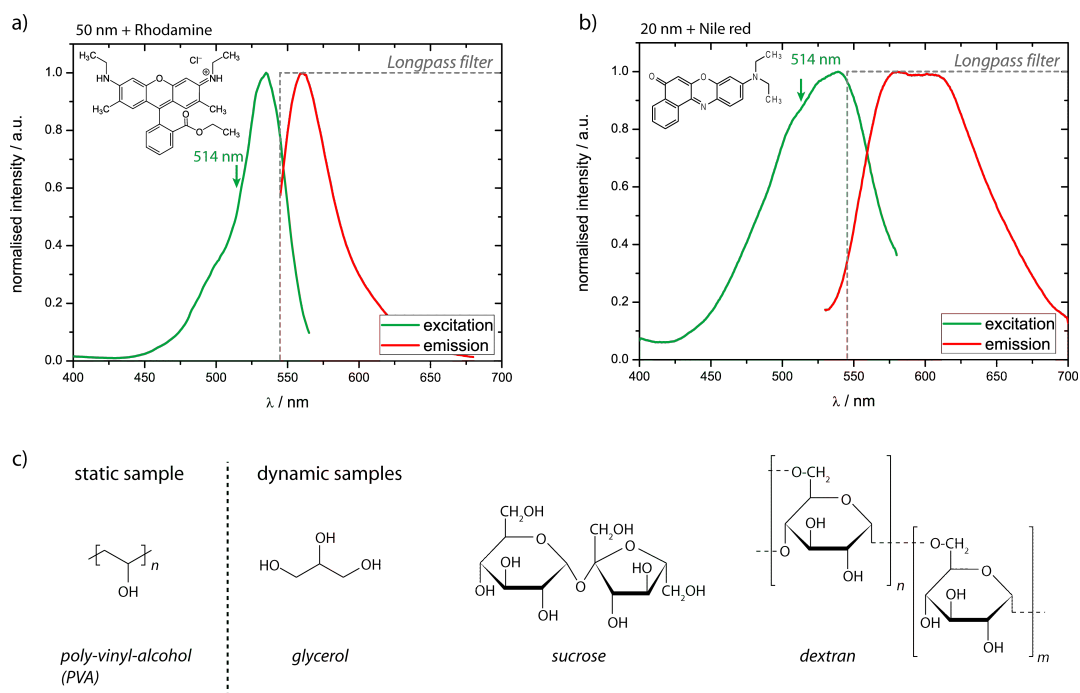


Figure 3.1: Samples. Normalized fluorescence excitation (green line) and emission (red line) spectra of the 50 nm sized beads loaded with the dye rhodamine (a) and the 20 nm sized beads loaded with the dye Nile red (b). For the spectra, both kinds of beads were dissolved in water. The green arrow marks the position of the laser excitation used in the tracking experiments. The step-like grey dashed line symbolizes the transmission characteristic of the detection filter. c) Chemical structures of the used samples for the static and dynamic experiments. (The two spectra for the 20 nm sized beads were recorded by Daniel Zalami.)

sion spectra of the beads with the dye rhodamine (fig. 3.1a) and the excitation spectrum of the beads with the dye Nile red (fig. 3.1b) show the typical shape for fluorescent molecules. But, the emission spectra of the beads with the dye Nile red exhibits a reduced maximum emission peak. This is attributed to the known effect of reabsorption and occurs for strong absorbers, especially when the concentration of the dyes is too high. Several possibilities have been tried to avoid the effect. For example by using a volume reduced cuvette, which is very thin, or by diluting the sample. But, due to a lack of suitable experimental equipment, it was not possible to record a better emission spectrum. Because the spectra were only used to define an appropriate detection filter that separates the absorption band from the emission band, the recorded emission spectrum was acceptable. Nevertheless, for a single bead, which is used in the measurements, the effect of reabsorption can be neglected. Due to the spectra, a dielectric long pass detection filter (HQ545LP, AHF) with a filter edge at 545 nm is used. Further, remaining excitation laser light with a wavelength of 514 nm (green arrow in fig. 3.1a,b) that is reflected from the

sample substrate, is suppressed. For details see publication P1. The transmission characteristic is symbolized by the grey dashed line in fig. 3.1a,b.

For the experiments, the beads are mixed with various fluids. This results basically in two kinds of samples. One where the particles are immobilised in a polymer matrix and one where the particles are moving. In the following they are called static sample and dynamic sample, respectively.

For the static sample, the polymer poly-vinyl-alcohol (PVA) is used, which is known to form a rigid polymer network where particles and molecules can be immobilised efficiently. For the dynamic samples, the widely known reference fluid glycerol, the simple sugar sucrose, and the more complex polysaccharide dextran is used. The chemical structures for all of the used fluids are shown in fig. 3.1c. For several reasons, the fluid glycerol was chosen for the characterisation experiments. First, in contrast to complex fluids like polymer solutions, liquid crystals or network forming fluids, glycerol and glycerol-water mixtures are simple fluids and thus featuring normal Brownian motion of an embedded tracer particle at room temperature. Second, the dependence of the viscosity on the temperature and the concentration is well documented [39]. For a given temperature and bead size this enables the choice of a time scale on which a diffusion process takes place, just by using a proper concentration. Moreover a comparison with theoretical values according to the Stokes-Einstein relation (eq. 2.2) is possible. And finally, the very high viscosity of pure glycerol of $\eta = 1.2 \text{ Pa s}$ [39] at a temperature of about 20°C allows it to follow the movement of very slow (normal) diffusing particles. For a first characterisation of an unknown setup this favours the measurements regarding the tracking performance.

The samples sucrose and dextran were used for the investigation of anomalous diffusion processes. Due to its chemical similarity to dextran, sucrose was used as a reference sample that shows normal diffusion behaviour, because no polymer-like network is formed, while the highly branched bio-polymer dextran mimicks the network structure of a cell membrane, where subdiffusive modes of motions of tracer particles have been observed [48, 49]. For more details see publication P3 and section 6.4. Furthermore, all the used samples are rather easy to handle and need no highly developed safety precautions, as it is for example necessary for biological samples like living cells or bacteria.

3.2 Sample preparation

In the following, the steps for preparing the static and dynamic sample are described. Figure 3.2 depicts both types schematically.

For the static sample the beads have been dissolved in a 5% PVA/water mixture resulting in a bead concentration of 50 pM. In a next step, which is mostly necessary when working with beads, the solution has to be ultrasonicated for about

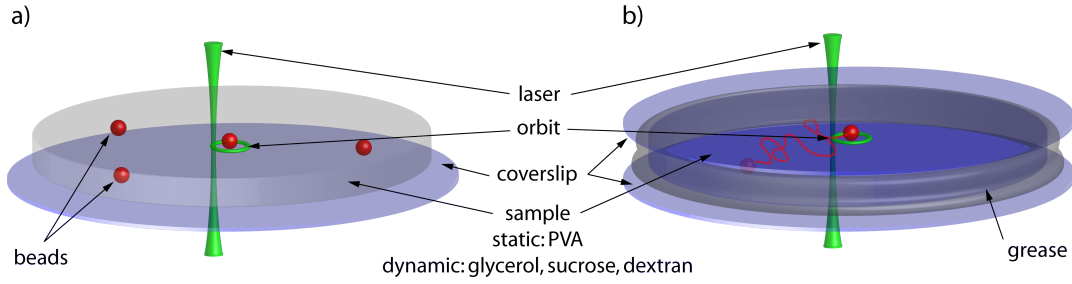


Figure 3.2: Schematic representation of the sample preparation. Both pictures show the focussed laser beam and the orbit that circles around a bead. a) Static sample with the beads fixed in a poly-vinyl-alcohol matrix; b) Dynamic sample with a bead diffusing in either glycerol, sucrose or dextran. The two coverslips are sealed on the edges with grease to prevent a flow of the sample.

10-15 minutes, to break up possible aggregates. Finally, a drop of about $25 \mu\text{l}$ was spin coated onto an acetone cleaned glass coverslip. Fig. 3.2a shows schematically the thin polymer film on the glass substrate with the embedded beads. Also the focussed laser beam and the light orbit, circling around a tracer particle are displayed. The static sample is used for basic characterisations of the setup and to determine the spatial accuracy of the position of the non-moving particle as a function of the temporal resolution.

The dynamic sample is prepared by diluting the corresponding stock solutions of the 20 nm and the 50 nm sized beads in water to a concentration of about 0.1 nM. Subsequently this solution was mixed with either glycerol, sucrose or dextran, resulting in a final bead concentration of about 2 pM. This very low concentration ensures, that the beads are well separated from each other. Possible aggregates are again destroyed by ultrasonication. Dependend on the experiment, a drop of the respective sample is sandwiched between two acetone cleaned coverslips. To prevent evaporation, which would induce a flow field in the sample, the edge of this home-built cuvette was sealed with high viscous grease (high-vacuum grease, Wacker). Fig. 3.2b displays schematically the cuvette with the moving beads (indicated by the red line) and the circling laser focus. The dynamic samples are used for an advanced characterisation of the tracking performance (publication P1), for the investigation of the analysis of particle trajectories (section 6.1 and publication P2), and to study anomalous diffusion processes (publication P3).

All experiments were carried out at a room temperature of $T = (21.0 \pm 0.5) ^\circ\text{C}$. At this point it is worth to note, that the concentration of the fluid in water and the concomitant change of the viscosity is determined by the final preparation step. The viscosity of the sample fluid changes slightly towards lower values when the bead solution is added.

I think nature's imagination is so much greater than man's, she's never going to let us relax.

Richard P. Feynman

4 Simulations

The characterisation of a new setup and in particular the determination of spatial and temporal accuracies, is quite hard, if no well defined and well designed reference system can be used. In these cases simulations are an effective tool to get a better understanding of the influences of important parameters like the emission intensity of the particle or the integration time during data acquisition. Furthermore, experimental results can be verified. Mostly, simulations are the first step to test an experimental idea.

In this chapter, I introduce simulations regarding the tracking performance of the planned setup. Therefore, in the first section the general procedure of the simulations are given, followed by a discussion about the achievable spatio-temporal resolution of the tracking setup in the subsequent section. Finally some limiting factors to track a particle are discussed. I want to mention, that similar simulations were performed in the literature, e.g. in the group of H. Mabuchi by A. Berglund [50] to characterise their setup.

4.1 General procedure

Based on Brownian dynamics, the motion of a fluorescent particle is simulated according to the overdamped Langevin equation (2.14) and the iterative Euler method (2.16) as already explained in the theory part (see section 2.1.2). The in such a way generated trajectories are called “simulated real”, in contrast to the “simulated reconstructed” trajectories, which are determined by the use of the derived position calculation algorithm (see eq. (2.29)). At this point it is worth to note, that in the experimental situation, the trajectories are called similarly “experimental real”, which describes the real diffusion of the particles and “experimental reconstructed”, which are the trajectories that are calculated from the emission signal of the tracer bead. The following table 4.1 helps to understand the used notation, where the entries stands for the origin of the corresponding trajectory. The trajectories with the notation “real” (simulated and experimental) do not contain any setup induced shortcomings and are only defined by the diffusion parameters a , η and T . (Mostly,

	simulated	experimental
real	Langevin equation	real diffusion
reconstructed	calculated by simulation of emission signal	calculated by acquisition of emission signal

Table 4.1: Summary of the explanation of the notation for the different types of trajectories, that were used in this thesis. The entries are the origins of the trajectories.

for the experimental trajectories the prefix “experimental” was abandoned.) The general procedure of the generation of a “simulated real” and a “simulated reconstructed” trajectory is described in fig. 4.1. The first one is quite easy, where an example for a typical random walk of a particle with a radius of $a = 10$ nm diffusing in a medium with viscosity $\eta = 1.2$ Pa s at a temperature of $T = 294$ K is shown in fig. 4.1a. The length of the trace is $t = 20$ s with a time resolution of $\Delta t = 4$ ms, resulting in $N = 5000$ data points. The here used parameter settings corresponds to a real tracking experiment, which I explain later in this thesis. However, for the description of the simulation procedure, these settings are just arbitrary numbers. The second one, i.e. the simulation of a “simulated reconstructed” trajectory, is more complicated. For a first approximation the following experimental properties have to be taken into account: a) the particle moves during the acquisition time Δt , b) the feedback mechanism has to be implemented and c) noise is superimposed to the emission intensity. Basis of all these calculations, is the simulation of the emission signal, i.e. equation 2.28. Because the emission signal in the experiment is acquired in terms of discrete photon packages S_n during the time resolution Δt , the simulation was programmed accordingly to match the experimental situation as good as possible. Therefore, a fast sampling time $\delta t \ll \Delta t$ is introduced. Further, this ensures that the movement of the particle during the acquisition time of Δt is considered. With this, the experimental property (a) is implemented. During the sampling time the emission signal $I(t)$ is regarded as constant, and the number of photons within one photon package results to

$$S_n = \int_0^{\delta t} I(t) dt \stackrel{I(t) \text{const.}}{=} I(t) \delta t. \quad (4.1)$$

Further, the time has to be transformed to discrete time steps $t \rightarrow n\delta t$. With this modifications the theoretical number of emitted photons S_n results to

$$S_n = \delta t S_0 e^{-\frac{2}{w^2}(x_p - x_s - R \cos(\omega n \delta t))^2} e^{-\frac{2}{w^2}(y_p - y_s - R \sin(\omega n \delta t))^2} + S_b \delta t. \quad (4.2)$$

Here, S_0 denotes the maximum number of emitted photons, i.e. the particle is at the position of the focal spot, S_b is the number of background photons, which is used as a constant offset, x_p and y_p are the actual position of the particle, which is unknown in the experiment, and x_s and y_s represents the implementation of

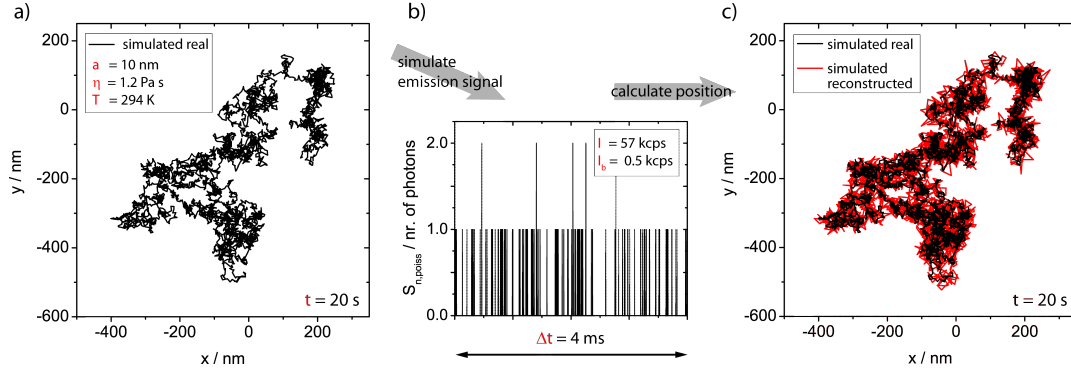


Figure 4.1: Principle scheme of the simulation of a particle trajectory. a) Simulated trajectory (black line), calculated with the use of the Langevin equation. This trace is regarded as the real trajectory. b) Simulated number of photons $S_{n,poiss}$ during one time interval Δt . c) Real (black line) and calculated (red line) trajectory according to the equation 4.3. The parameters marked in red (bead radius a , viscosity η , temperature T , elapsed time t , emission intensity I , background signal I_b and the time resolution Δt) can be set in the simulation.

the feedback mechanism (piezo stage in the experimental setup). With this, the second experimental property (b) is considered. The actual values for x_s and y_s are the preceding calculated values x_c and y_c (equations (4.3)). This ensures, that the particle is restored in the centre of the orbit. The values for the coordinates x_p and y_p were taken from the “simulated real” trajectory (*vide supra*). The aforementioned modifications also have to be applied to the equations for the position calculation, i.e. (2.29). This leads to:

$$x_c(t) = \frac{w^2}{2R} \frac{\sum_{n=1}^{N_S} S_n \cos(\omega n \delta t)}{\sum_{n=1}^{N_S} S_n}, \quad y_c(t) = \frac{w^2}{2R} \frac{\sum_{n=1}^{N_S} S_n \sin(\omega n \delta t)}{\sum_{n=1}^{N_S} S_n} \quad (4.3)$$

Here, the integrals have to be exchanged to sums. The upper bound of integration changes to the upper bound of the sum, i.e. N_S , which corresponds to the number of sampling intervals that is used for one position determination and is given by $N_S = \Delta t / \delta t$. In an experiment, this number is defined by the frequency of the focus rotation ν and the number of cycles P ($N_S = P / \nu \delta t$, see publication P1 for details). One has to be aware, that S_n is only a theoretical number of photons. To be as close as possible to an experimental situation, photon statistics, which is the basis of the emission of fluorescent dyes, has to be taken into account by a Poisson process (third experimental property (c)). Each “real” number of photons during one time bin δt is determined by a Poisson distribution with an expectation value of the theoretical number of photons S_n and is called $S_{n,poiss}$ in the following. A typical simulated number of photons during a time interval of $\Delta t = 4$ ms is shown in fig. 4.1b. Reasonable parameters were chosen, i.e. the width of the laser focus

was set to $w = 270$ nm, the radius of the orbit to $R = 190$ nm, which is the optimal value according to [50] where $R = w/2^{1/2}$ was determined, and the frequency of the focus rotation was set to $\nu = \omega/2\pi = 1$ kHz. The sampling time was $\delta t = 2 \mu\text{s}$, which results to a number of sampling intervals of $N_S = \Delta t/\delta t = 2000$. This corresponds to 4 periods of rotation of the focus. (Later in this thesis we will see, that this parameters match the experimental conditions.) From the number of simulated photons, the mean emission intensity of the tracer results to $\bar{I} = 57 \text{kcps}$ and the background intensity to $I_b = 0.5 \text{kcps}$ (kcps: kilo counts per second).

To calculate the coordinates x_c and y_c according to the equations (4.3), the simulated signal $S_{n,poiss}$ as well as the values $S_{n,poiss} \cos(\omega n \delta t)$ and $S_{n,poiss} \sin(\omega n \delta t)$ are accumulated during each 4 ms period (S_n in eqn. (4.3) was replaced by $S_{n,poiss}$). By successively repeating this procedure, the trajectory of the particle, i.e. $\mathbf{r}(t) = (x(t), y(t))$ can be reconstructed. Figure 4.1c displays both, the trajectory generated with the Langevin equation (black) and the trajectory, that is reconstructed. Beside some slight deviations according to the position uncertainties (noise and movement during signal acquisition), the “simulated reconstructed” trajectory matches the “simulated real” one.

To summarize, first a “fast” trajectory on a time scale of $\delta t = 2 \mu\text{s}$ is generated, that corresponds to the movement of the particle during the integration time Δt . Out of the positions of this trajectory, the signal $S_{n,poiss}$ is calculated, accumulated and multiplied with a cosine and sin function, necessary for the calculation of the particle position. Finally, the positions x_c and y_c are calculated according to 4.3. All simulations were performed using home-written Matlab programs. The source code of the generation of the “simulated real” and “simulated reconstructed” trajectories is given in the appendix A. This simulations are an effective tool

- to scan the parameter range (e.g. rotation frequency ν , time resolution Δt , orbit radius R , etc.), which is appropriate for the experiment to achieve the best tracking performance,
- to compare the results of simulations and experiments,
- and to study the influences of several experimental artifacts (e.g. noise and position averaging) or the influences of diffusion parameters (e.g. viscosity η or bead size a) on the analysis of the mean squared displacement and the concomitant interpretations.

4.2 Spatio-temporal accuracy

With the use of the afore described simulations of the reconstructed trajectories the tracking performance by means of the spatial and temporal accuracy is studied

as a function of the emission intensity and as a function of the diffusion coefficient. Starting point is the simulation of the number of photons $S_{n,poiss}$ that is used by the feedback algorithm to determine the position. The theoretical and Poisson distributed number of photons, i.e. S_n and $S_{n,poiss}$, during a time interval that corresponds to the time resolution of $\Delta t = 4$ ms for a moving bead is displayed in fig. 4.2a, represented in red and black, respectively. For a better visualization a low emission signal of $\bar{I} = 30$ kcps was chosen, otherwise the Poisson distributed number of photons are too crowded. The diffusion coefficient was set to $D = 43 \times 10^{-3} \mu\text{m}^2/\text{s}$. The signal for the theoretical number of photons S_n is periodic, but heavily fluctuating. The reason is the movement of the particle, during the integration time Δt . As already mentioned, the emitted photons depend on the position of the particle within the orbit. As soon as the movement happens on a faster time scale than the integration time, the periodic emission fluctuates accordingly. Because the Poisson distributed number of photons is calculated from the theoretical number of photons, the described behaviour (periodic and fluctuating emission) is carried forward to $S_{n,poiss}$. The density of photons ($S_{n,poiss}$) is high when S_n is high.

However, despite the fluctuations of the emitted photons, the feedback algorithm is still able to calculate the position of the particle, with an accuracy, that is determined by photon statistics (noise) and position averaging during data acquisition. Figure 4.2b shows two 1-dimensional “simulated reconstructed” trajectories with $N = 5000$ data points for the time resolutions $\Delta t = 0.5$ ms (blue) and $\Delta t = 9.0$ ms (red), both with a mean emission intensity of $\bar{I} = 157$ kcps and a diffusion coefficient of $D = 400 \times 10^{-3} \mu\text{m}^2/\text{s}$. It is trivial, that the particle simulated with the higher time resolution of $\Delta t = 9.0$ ms can move a larger distance, because the total observation time for the movement is $t = N\Delta t$ and hence, longer than for a particle simulated with $\Delta t = 0.5$ ms. However, rather than the covered distance, the position error in the trajectory is considered. Despite a larger number of photons, which favours the position determination, the “simulated reconstructed” trajectory determined with the time resolution of $\Delta t = 9.0$ ms appears more noisy than the trajectory determined with $\Delta t = 0.5$ ms. Obviously, the motion during the acquisition time is dominant. Dependent on the emission intensity and the mobility of the particle (diffusion coefficient), both effects contribute to the spatial accuracy. To determine this accuracy, the positional error of a trajectory has to be calculated. In order to do so, the root-mean-square (rms) error between the positions of the “simulated real” trajectory, x_c , and the positions of the “simulated reconstructed” trajectory, x_p , has to be determined.

$$\sigma_x = \sigma_{rms} = \sqrt{\frac{1}{N} \sum_{i=1}^N (x_{ci} - x_{pi})^2} \quad (4.4)$$

4 Simulations

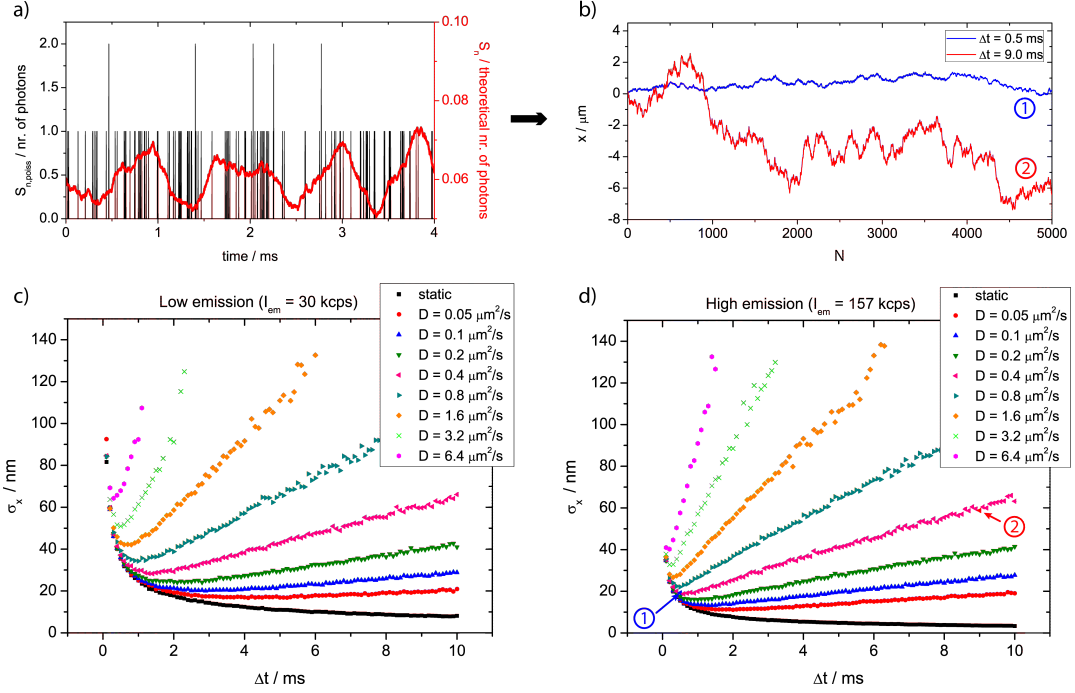


Figure 4.2: Simulation of the dynamic position accuracy. a) theoretical (red) and Poisson distributed (black) number of emitted photons within one time bin of Δt b) calculated position as a function of the number of position determinations N for a time resolution of $\Delta t = 0.5$ ms (blue) and $\Delta t = 9.0$ ms c), d) dynamic position accuracy for a high mean emission intensity (c) and a low mean emission intensity (d) as a function of the time resolution for various diffusion coefficients between the static case of $D = 0 \mu\text{m}^2/\text{s}$ and a fast particle motion of $D = 6.4 \mu\text{m}^2/\text{s}$. The two trajectories, simulated in b) are indicated in d) by the numbers 1 and 2. More details see text.

In fig. 4.2c,d the 1-dimensional spatial accuracy σ_x as a function of the time resolution Δt for diffusion coefficients between $D = 0 \mu\text{m}^2/\text{s}$ (static) and $D = 6.4 \mu\text{m}^2/\text{s}$ are shown for a low (fig. 4.2c) and a high (fig. 4.2d) mean emission intensity of $\bar{I} = 30$ kcps and $\bar{I} = 157$ kcps, respectively. The low emission signal corresponds to a typical emission of a single molecule, while the high signal corresponds to the typical emission of a fluorescent bead. Qualitatively, both graphs show the same results. With an increasing value of the time resolution (in everyday language: the time resolution gets worse) the spatial accuracy rapidly gets better until a minimum value is reached, from which it grows slowly. To explain this behaviour let us consider a given diffusion coefficient. For very low time resolutions the particle can be regarded as static and the position accuracy is getting better according to $\sigma_x \propto 1/\sqrt{\Delta t}$. This is evident for the spatial accuracy of the static particle (black data points in fig. 4.2c,d). For higher values of Δt the position of the particle gets blurred due to its movement during one time resolution step, i.e. the positional er-

ror is growing. Hence, it exists a minimum, where the best spatial accuracy can be achieved. For fast particles, i.e. high diffusion coefficients, the position averaging effect is more pronounced than for slow particles. A common comparison is the diffusion of a 20 nm bead in water, which has a diffusion coefficient of $D = 21.5 \mu\text{m}^2/\text{s}$. According to the presented simulations, the particle can not be tracked or at least a very high time resolution is required. For a successful tracking experiment, the particle has to be larger and/or the viscosity of the surrounding fluid has to be higher.

However, this two graphs (fig. 4.2c,d) serve as an orientation for setting suitable experimental parameters and to know the theoretical limits of the tracking performance. In advance, the experimentalist can check if the particles in the system he wants to investigate can be tracked and if so, which spatial accuracy can be expected. A problem occurs, if the simulated accuracies are compared with experimental ones. In an experiment the “real” position, which was necessary for this calculations, is not accessible and other methods for the determination of the spatial accuracy has to be used. One possibility is discussed in detail in publication P1, where the offset of the MSD-curve was used as an indicator for the spatial accuracy.

4.3 Loosing a particle

As long as the particle can be tracked, it stays inside the light orbit, generated by the rotating focus, and is restored to the centre of the orbit after every time period Δt . Hence, this means, that the emission intensity of the particle is kept constant during tracking. As soon as the particle gets lost, the emission intensity decreases immediately to the background intensity. Possible reasons to loose a particle are a weak emission signal or a high mobility.

The situations for a successful and a failed tracking were simulated for a bead with radius $a = 10 \text{ nm}$ at a temperature of $T = 294 \text{ K}$. The top graph of fig. 4.3a displays the 1-dimensional “simulated real” (black) and “simulated reconstructed” (red) trajectory of a slow diffusing bead with a high emission intensity. The parameters were set to $\bar{I} = 157 \text{ kcps}$ and $\eta = 1.2 \text{ Pa.s}$, which corresponds to a diffusion coefficient of $D = 17.95 \times 10^{-3} \mu\text{m}^2/\text{s}$. The reconstructed positions follow nicely the real trace. A detailed view is shown in the inset of fig. 4.3. The corresponding intensity trace (bottom graph of fig. 4.3a) yields the expected constant emission intensity, i.e. the particle is tracked continuously.

To simulate a tracking experiment, where the particle gets lost, a fast bead with a low emission intensity is used. The trajectories (real and reconstructed) are shown in the upper part of fig. 4.3b. Here, $\bar{I} = 21 \text{ kcps}$ and $\eta = 0.1 \text{ Pa.s}$, i.e. $D = 215.3 \times 10^{-3} \mu\text{m}^2/\text{s}$, were chosen. The diffusion is too fast and the emission is too low, to follow the movement of the particle. At a time of about 2.5 s the posi-

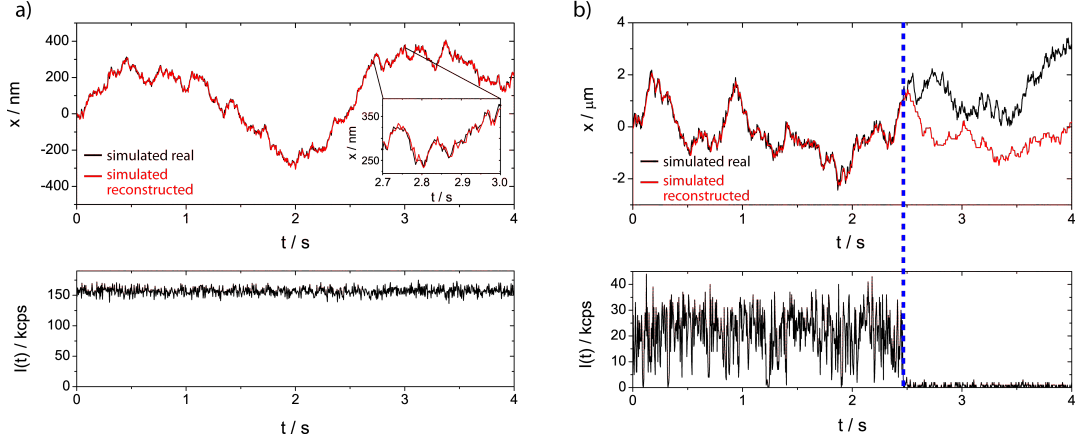


Figure 4.3: Results for the simulations of a fast and high emitting particle (a) and a slow and low emitting particle (b). The top graphs display the time traces of the true (black) and the calculated positions (red) and the bottom graphs of the intensity time trace. The inset in (a) is an enlarged view of the two trajectories. The blue dashed line in (b) indicates the time, where the particle is lost.

tion can not be calculated anymore and as mentioned above, the emission intensity drops instantly to the background level (indicated by the blue dashed line in fig. 4.3b). This happens for example, if the bead moves that fast, that it exceeds the rim of the orbit or if the emission is not high enough to calculate the position. This example explains nicely the criterion for a termination of a tracking experiment. As soon as the emission signal drops to the background level the measurement is stopped.

With a rough estimation, a limiting case for the 2-dimensional tracking performance can be determined for a high emission signal. The particle can definitely not be tracked, if the mean displacement between two consecutive positions is larger than the value for the radius of the orbit R , i.e. if

$$\begin{aligned}
 \sqrt{\langle \Delta \mathbf{r}(k\Delta t)^2 \rangle} &\geq R & \text{for } k = 1 & \quad (4.5) \\
 \Leftrightarrow 4D\Delta t &\geq R^2 \\
 \Rightarrow D &\geq \frac{R^2}{4\Delta t}
 \end{aligned}$$

By chance it could happen, that the particle can be tracked partially, but with a mean displacement larger than the radius of the orbit, a permanent tracking is not possible. For the parameters $\Delta t = 4$ ms and an orbit radius of $R = 190$ nm, the limiting diffusion coefficient is determined to $D = 2.26 \mu\text{m}^2/\text{s}$. This can also be compared with the values given in fig. 4.2d. Systems, that exhibits a larger diffusion coefficient than the determined one, can not be tracked with this settings. Coming back to the example of a 20 nm bead in water, successful tracking would

require a time resolution of about $\Delta t = 0.4$ ms, according to equation 4.6. In the following section the parameter limitations for the experimental setup are introduced. At this point I want to mention, that at the present stage of the setup it is not possible to track a 20 nm bead in water. The temporal accuracy has to be improved by a factor of 10.

A learning experience is one of those things that say, "You know that thing you just did? Don't do that."

Douglas Adams

5 The tracking setup

The main work of this thesis was the development of a new experimental setup that is capable of measuring single-particle trajectories with a high spatio-temporal resolution. It started from an empty optical table and ended with the successful implementation of single-particle tracking experiments. Among the afore mentioned various techniques, the orbit tracking method with sample scanning was chosen. This enabled the recording of successive positions of a particle for more than 10 minutes with a time resolution of 4 ms, resulting in trajectories with more than 1.5×10^5 positions. A spatial resolution of better than 10 nm was achieved. However, prior to the acquisition of evaluable trajectories, numerous characterisation experiments have to be performed, to identify possible shortcomings that disturb the measurements. This work was substantial, so that it was suited for a publication in the *Journal of the optical society of America A (JOSA A)* with the title "Setup for single-particle orbit tracking: artifacts and corrections", which can be found in part II (publication P1) and which is the major publication of this thesis. It includes the description of the experimental setup, its full characterisation and the first successful tracking experiments with this setup. In the following sections the content of this publication is summarized and additional results on the spatial tracking accuracy of a static particle are given.

5.1 Optics & Hardware

In principle, the experimental setup consists of a home-build confocal fluorescence microscope, a detection unit, and a laser beam deflection unit, which is the core part of the setup. Two acousto-optical deflectors (AOD) guide the laser beam (514 nm) on a circular path. This light orbit is projected into the microscope and is further reflected towards a water-immersion objective, that focuses the orbit into the plane of the sample, where the dye loaded particles are excited. The emission signal of the particles is then collected by the same objective and directed to either a CCD camera for widefield imaging or to an avalanche photo diode (APD) for tracking with high time resolution. The optical pathway was calculated with the aid of ray

transfer matrix analysis, because the mutual distances between all optical elements have to be as exact as possible. To operate the setup, an ingenious home-written program was used to implement the tracking algorithm for the calculation of the particle positions. This was done with a programmable measuring instrument, that is also responsible for the generation of all output signals, e.g. the piezo and AOD signals, and the acquisition of the emission signal, recorded by the APD. The use of only one single communication instrument between the PC and the setup made it possible to avoid hardware, like frequency generators, lock-in amplifiers or counter cards for the PC, and to have a perfect time synchronisation between all output and input signals, which is a prerequisite for this tracking method. Only if the output signals for the generation of the light orbit are synchronized with the data acquisition of the emission signal, a meaningful position of the particle can be calculated. The presented orbit tracking technique is able to reconstruct the 2-dimensional motion of the particle as long as this motion takes place in the plane of the orbit, which is also the xy -plane. The problem is now to keep the particle in this plane, e.g. by compensating for the particle motion in the 3rd dimension (z -axis). This was done by implementing a z -tracking algorithm, which was developed together with the diploma student Stefan Hain. The piezo with the mounted sample is wobbled up and down along the z -axis, i.e. also the particle is moved up and down and penetrates the orbit once in each direction. For every up (down) movement the z -position at which the particle features the highest emission is stored and serves as the new origin for the subsequent down (up) movement. This enabled the tracking over an extended period of time. Typically, tracking times of 10 minutes were used to analyse the diffusion processes, but it is possible to follow the motion of the tracer for more than 30 minutes. At the present stage of the setup the total recording time depends only on bleaching of the tracer beads and on the maximum scan range of the piezo ($100\ \mu\text{m}$ per axis). The important parameters of the setup are the orbit radius R , the frequency of the focus rotation ν and the number of rotation periods P , that were used for setting the time resolution ($\Delta t = P/\nu$) and the parameters for the z -tracking algorithm. The latter ones are a number of steps with a defined step size for the up and down movements of the piezo. These values have to be optimized separately for every new sample. Combining simulations, literature research and characterisation measurements allowed to define optimal settings for the remaining parameters. The values were found to be $R = 190\ \text{nm}$, $\nu = 1\ \text{kHz}$ and $P = 4$. Having a suitable set of parameters, a characterisation is necessary to learn the capability of the setup.

5.2 A static particle

The most basic characterisation is the investigation of a static particle. It is useful for studying the position accuracy without any disturbing effects due to the motion

of the particle. First this situation is again simulated to know the theoretical predictions, which are then compared with experimental data. Therefore, in the following two subsections I will explain the simulated as well as the experimental determined position accuracy of a static particle, followed by a comparison.

5.2.1 Simulation

The procedure of the simulation is similar to the already described one in chapter 4, with the difference, that the “simulated real” trajectory is now a fixed position. Here, it was set to $(x_p, y_p) = (0, 0)$, which corresponds to the centre of the orbit. With the feedback mechanism switched on, it does not matter at which starting position within the orbit the particle is placed. Because after the first position calculation, the feedback loop restores the particle back in the centre of the orbit with an accuracy, that is determined by acquisition limits (noise and position averaging during data acquisition). The simulation of the theoretical and the Poisson distributed number of photons, i.e. S_n and $S_{n,poiss}$ are shown in fig. 5.1a during the acquisition time of $\Delta t = 4$ ms. A particle at the $(0, 0)$ position should result in a constant value for the theoretical number of emitted photons, because in an ideal case, also x_s is zero and the expression $x_p - x_s$ in equation (4.2) vanishes.

$$\begin{aligned} S_n &= \delta t S_0 \exp \left\{ -\frac{2}{w^2} \underbrace{(-R \cos(\omega n \delta t))^2 + (-R \sin(\omega n \delta t))^2}_{=R^2} \right\} + S_b \delta t \quad (5.1) \\ &= \delta t S_0 \exp \left\{ -\frac{2R^2}{w^2} \right\} + S_b \delta t = const. \end{aligned}$$

The reason for the periodic signal are the photon statistics and the feedback mechanism. Due to the Poisson distributed emission, the calculated position is not exactly zero. Via x_s this non-zero position is fed back to the generation of the number of photons. Hence, the expression $x_p - x_s$ in equation 4.2 is non-zero, leading to a weak periodic signal S_n . The emission of photons, i.e. $S_{n,poiss}$ stays more or less constant, because the absolute values of S_n itself as well as the amplitude are quite small.

From the simulated number of photons, the position of the particle is reconstructed. Figure 5.1b displays the x-position time-trace for $N = 5000$ position determinations, for a time resolution of $\Delta t = 0.5$ ms (blue) and $\Delta t = 9.0$ ms (red). Both simulations were performed for a mean emission intensity of $\bar{I} = 157$ kcps. The high fluctuations in the position at a time resolution of $\Delta t = 0.5$ ms compared to $\Delta t = 9.0$ ms are ascribed to the reduced number of photons, that can be acquired during the time resolution of $\Delta t = 0.5$ ms. A higher photon count rate leads to a more accurate position determination. To quantify this positional noise, the error in calculating a position in one dimension, which also defines the spatial accuracy,

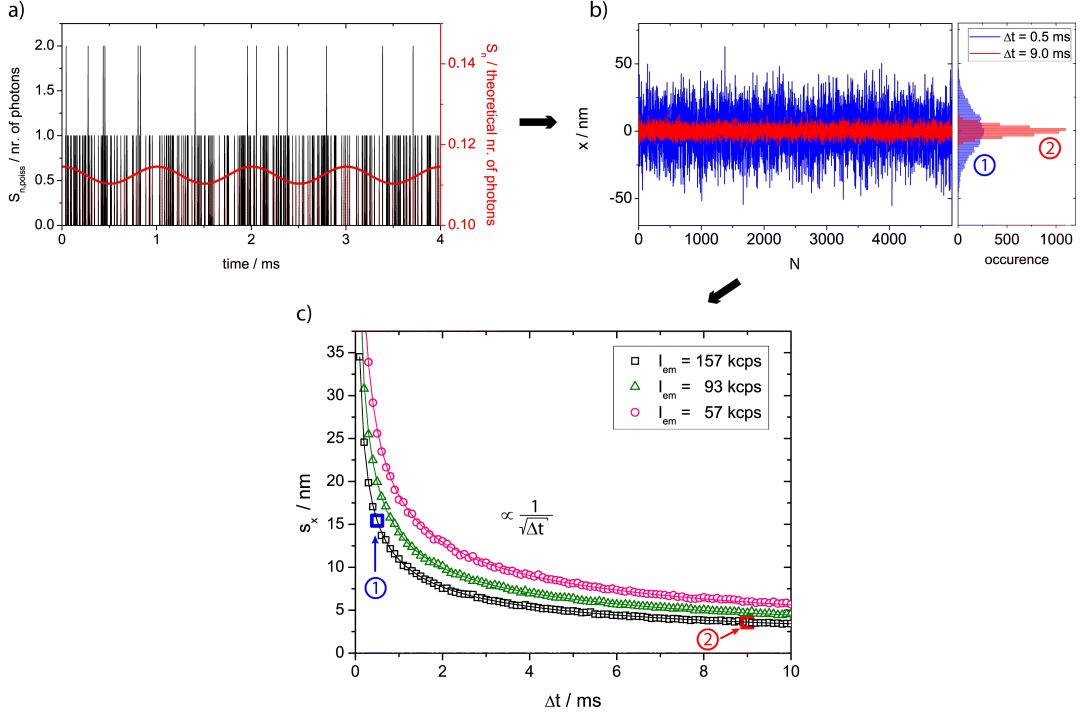


Figure 5.1: Simulation of the static position accuracy. a) simulated theoretical (red) and Poisson distributed (black) number of photons during the time resolution of 4 ms b) reconstructed positions for two different values of the time resolution, i.e. $\Delta t = 0.5 \text{ ms}$ (blue) and $\Delta t = 9.0 \text{ ms}$ (red), both with a mean emission intensity of $\bar{I} = 157 \text{ kcps}$ c) shows the data points of the spatio-temporal accuracy for three different mean emission intensities. (s_x) is the empirical standard deviation of the histograms shown in b). The two examples of subfigure b) are indicated by the numbers 1 and 2 in subfigure d). The full lines are fits to the data points according to the fit function $y = A/\sqrt{x} + B$. For more details see text.

is given by the empirical standard deviation s_x of the distribution of positions (see histograms in fig. 5.1b) according to

$$s_x = \sqrt{\frac{1}{N-1} \sum_{i=1}^N (x_{c,i} - \bar{x})^2} \quad \text{with} \quad \bar{x} = \frac{1}{N} \sum_{i=1}^N x_{c,i}. \quad (5.2)$$

Figure 5.1c displays the accuracies s_x for three different mean emission intensities, $\bar{I} = 157 \text{ kcps}$, $\bar{I} = 93 \text{ kcps}$ and $\bar{I} = 57 \text{ kcps}$, as a function of the time resolution Δt . The two highlighted points in blue and red corresponds to the time-traces shown in fig. 5.1b. As expected, the accuracy in determining the position of a static bead is getting better at higher mean emission intensities, due to the higher number of photons, that are available for the feedback algorithm. The solid lines are fits to

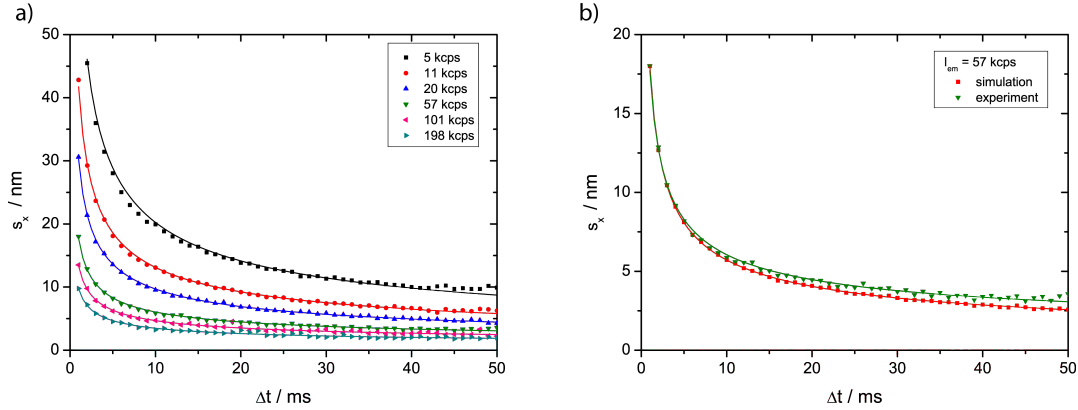


Figure 5.2: a) Static position accuracy for the x direction s_x versus time resolution Δt for varying emission intensities. b) Comparison between a simulation of the static position accuracy and the corresponding experiment at an emission intensity of $I_{em} = 57$ kcps.

the data points according to the fit function $y = A/\sqrt{x} + B$, where A and B are minor important parameters. The relevant point is the dependence $s_x \propto 1/\sqrt{\Delta t}$, which is nicely described by the data points.

However, this simulations tells us, that a position accuracy far below the classical diffraction limit of light can be achieved. For example, at a typical time resolution used in the experiments of $\Delta t = 4$ ms and a high mean intensity of $\bar{I} = 157$ kcps a position accuracy of $s_x = 5.3$ nm is possible. In general, for a given emission intensity the experimentalist has to find a trade off between a high spatial accuracy and a high time resolution.

5.2.2 Experiment

The experimental verification of the static position accuracy as it was simulated in the previous subsection gives the first results on the capability of the setup. In order to do so, a fluorescing polymer bead (20 nm in diameter) was immobilised in a polymer matrix (see chapter 3) and the position of the particle was calculated according to the feedback algorithm (see eq. (4.3)), for different time resolutions. This value is set by the number of rotation periods P of the laser focus that circles with a frequency of $\nu = 1$ kHz. For example, for $P = 2$ the time resolution results to $\Delta t = P/\nu = 2$ ms and so on. For each value of the time resolution a position time-trace is recorded for about 30 seconds and the spatial accuracy was determined by the empirical standard deviation of the distribution of positions, like it was done for the simulations. In figure 5.2a the experimentally determined spatial accuracies are displayed as a function of the time resolution for various mean emission intensities between $\bar{I} = 5$ kcps and $\bar{I} \approx 200$ kcps. The emission intensity could be varied by changing the excitation intensity. The solid lines are fits to the data points

according to the fit function $y = A/\sqrt{x} + B$ and should only serve as guides for the eye. However, the data points follow nicely the relation $s_x \propto 1/\sqrt{\Delta t}$, already shown in the simulations. Position accuracies of less than 5 nm could be achieved for the highest measured mean emission intensity and for time resolutions of $\Delta t > 5$ ms. Even for very low emitting particles the accuracy is far beyond the classical diffraction limit of light.

Additionally, for a mean emission intensity of $\bar{I} = 57$ kcps a comparison between the experiment and the simulation is shown in fig. 5.2b. The very first data points ($\Delta t < 5$ ms) coincide perfectly, while at an increasing time resolution the values for the spatial accuracy for the experiment levels off towards larger values. This is addressed to a weak drift of the whole setup. The longer the integration time, the more pronounced is a possible drift. Nevertheless, the experimental results agree with the predictions made by the simulations.

5.3 Artifacts & Corrections

Next, the setup was characterised with respect to experimental shortcomings to avoid misinterpretations of the measured trajectories. Four major artifacts could be determined, which influences the position determination. These are i) a systematic error in the tracking algorithm, ii) a (mis)alignment of the piezostage, iii) the finite signal-to-noise ratio of the emission signal and iv) the position averaging during data acquisition. In figure 5.3 each of these artifacts is depicted schematically and in the following, all of them are explained briefly, together with possible solutions to prevent them. The details can be found in publication P1.

The systematic error in the tracking algorithm (i) results from a mis-calculation of the position of the particle when it approaches the rim of the light orbit. The upper left image in figure 5.3 displays this behaviour schematically. For particle positions close to the centre of the orbit, the emission signal is in a first approximation modulated with a harmonic function (see appendix B). If the particle nears the rim of the orbit, the modulation gets anharmonic. The problem is, that the higher harmonics in the modulation of the emission signal, are neglected for the position calculation, which leads erroneously to smaller values of the particle position. This effect increases, the closer the particle is to the rim of the orbit. The graph in the upper left image of fig. 5.3 shows this behaviour, where the “reconstructed” radial position is plotted against the “real” one. To compensate for that error, a real-time correction function was applied, that corrects the position. The second artifact (ii) is the (mis)alignment of the piezostage (cf. fig. 5.3, upper right image). It is nearly impossible to mechanically align the xy-plane of the piezostage perfectly parallel with the plane of the orbit. It remains a slight tilt angle between the z-axis of the piezo and the axis of the orbit (optical axis). Thus, according to the z-tracking algorithm the periodic movement of the piezo provokes a periodic movement of

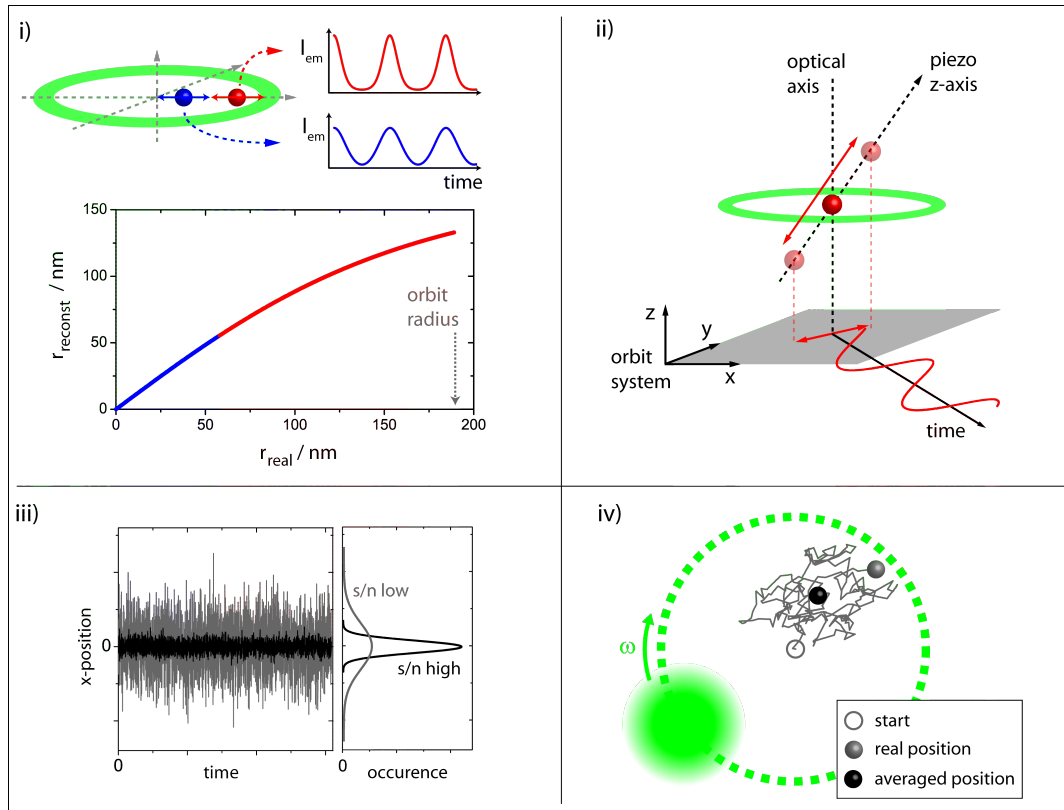


Figure 5.3: Schematic overview of the experimental shortcomings. *i)* Systematic error in the tracking algorithm. The blue and red sphere represent particle positions within the light orbit (green ellipse) where the emission signal is regarded as harmonic (blue) and anharmonic (red). This transition is not that strict, rather a continuous increase of the anharmonic parts is observed. The corresponding mis-calculation of the positions is depicted in the lower part of *i)*. *ii)* (Mis)alignment of the piezostage. The red sphere is a particle that moves along the z -axis of the piezo. This motion is projected to the xy -plane and hence superimposed to the trajectory. *iii)* Finite signal-to-noise ratio. The position time-trace as well as the corresponding histograms for a high s/n -ratio (black) and a low s/n -ratio (grey) are shown. *iv)* Position averaging during data acquisition. The grey trajectory has a length that corresponds to the time interval of the acquisition time. The start, end and average position of the trajectory are shown. Adapted from publication P1.

the particle along the z -axis of the piezo, which is projected to the xy -plane and hence superimposed to the “real” 2-dimensional trajectory. Therefore, prior to the evaluation of the trajectory, a lock-in analysis of the position time-trace is applied to determine the phase and the amplitude of the periodic motion. Once these parameters are known, the trajectory can be corrected for this oscillation. This two artifacts are called “setup induced”, because components of the setup (piezo,

tracking algorithm) are responsible for the errors, while the remaining two artifacts rather stem from acquisition limits. Artifact iii) is the finite signal-to-noise ratio (s/n-ratio), which is displayed schematically in the lower left part of figure 5.3. The higher the noise, i.e. the lower the s/n-ratio for a given signal, the less precise a position can be determined. The consequence of this artifact is noticed after the MSD analysis of the trajectory and results in a positive offset to the MSD data points. This can simply be corrected by subtracting this offset. The last artifact, that was found is the position averaging during the acquisition of the emission signal (iv), which leads to a blurring of the position. The lower right image in figure 5.3 displays the trajectory of a particle during the acquisition time Δt , with the final “real” and the averaged “reconstructed” position of the particle. Here, the consequence is a negative offset to the MSD data points. To correct this artifact, the offset is determined and added to the MSD data points. Details about the description of all the artifacts as well as the corresponding experimental results can be found in publication P1. After a special hierarchy of corrections was defined, the first successful experiment, that was measured with this setup could be analysed. Therefore a sample of 20 nm sized beads diffusing in pure glycerol was used. At a given time resolution of $\Delta t = 4$ ms a spatial accuracy of $\Delta r = 7.5$ nm could be achieved. The diffusion process was also compared with theoretical predictions according to the Stokes-Einstein relation, which showed a good agreement.

Additionally, an analysis of the setup drift ($v_{drift} = 0.05$ nm/s) and the effects of the sample flow ($v_{flow} = 10$ nm/s) were investigated. Both were negligible compared to a typical mean displacement of the used tracer bead within one second (≈ 250 nm). Moreover, estimations of the influences of optical forces, i.e. the radiation pressure and optical trapping, are discussed. The results are, that the estimated forces are 5 orders of magnitude weaker than the forces that are responsible for the diffusion process. Hence, optical forces can be neglected as well. For details see the appendix of publication P1.

With this chapter and in particular with the content of publication P1, the basics of the tracking principle and the characterisation of the whole setup is settled. It includes the first tracking experiment that was measured with this setup and that is analysed in terms of the mean squared displacements. The experimental results were compared with theory and were in good agreement.

6 Single-particle tracking: results & discussion

In this chapter I will present the results of the tracking experiments. Among these the findings described in the sections *Accuracy of diffusion coefficients* and *Crowded Fluids* were published. Hence, the content of these two sections is a summary of the published work, that can be found in part II of this thesis. The sections of this chapter are structured as follows.

- Analysis of the measured single-particle trajectories

Besides the commonly practiced mean squared displacement analysis, which takes the major part of this section, some alternative approaches are discussed.

- Accuracy of measuring a diffusion coefficient (publication P2)

The accuracy is discussed as a function of the length of a trajectory and as a function of the number of fitting points that were used for a linear fit to the MSD curve.

- Particle sizes

Using the Stokes-Einstein equation the size of the measured particles can be determined from the diffusion coefficients.

- Crowded fluids (publication P3)

The use of the new tracking setup and a new way of analysing and plotting the data made it possible to clarify the theoretical model of subdiffusion in a crowded fluid which was consistent with the model of fractional Brownian motion.

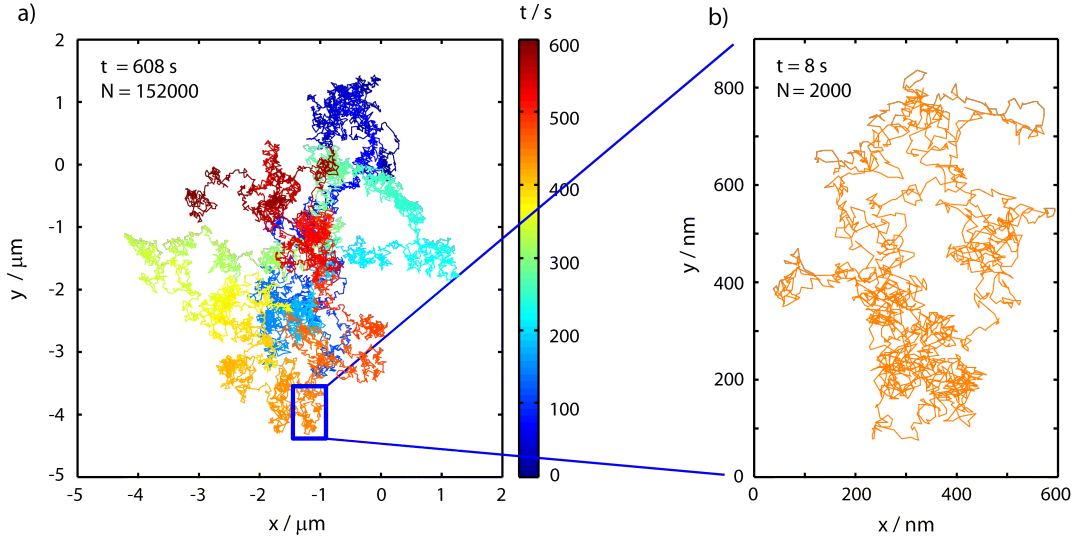


Figure 6.1: a) Example of a trajectory of a 20 nm sized bead in pure glycerol, recorded for $t = 608$ s ($N = 1.52 \times 10^5$ data points). b) Extended view of a sequence with $N_{seg} = 2000$ positions ($t = 8$ s).

6.1 Analysing diffusion based on single-particle trajectories

From seven different beads each with a nominal diameter of 20 nm diffusing in pure glycerol, trajectories of about 1.5×10^5 positions were recorded. For every run a particle was selected from the widefield image that was sufficiently separated from other particles and from the surface of the coverslips. An example for a typical trajectory is displayed in fig. 6.1a. It represents 1.52×10^5 data points recorded with a time resolution of $\Delta t = 4$ ms and corresponds to an elapsed time of 608 s which is indicated by the colour code where blue corresponds to the begin of the trajectory and red to its end. In the following the analysis of the mean squared displacements and three alternative approaches were discussed on one representative trajectory.

6.1.1 Mean squared displacement analysis

From the recorded trajectory $\mathbf{r}(t) = (x_p(t), y_p(t))$, consisting of N positions, the time-averaged MSD after a time lag $\tau = k\Delta t$ is calculated according to equation 2.21 [34]. For the trajectory displayed in fig. 6.1a the inset in fig. 6.2a shows the full MSD as a function of the lag time. For lag times $\tau < 50$ s the MSD features a linear increase followed by strong fluctuations at longer times that reflect the progressively decreasing averaging. Therefore the analysis of the MSD curves is usually limited to the first few data points. Having more than 10^5 data points at

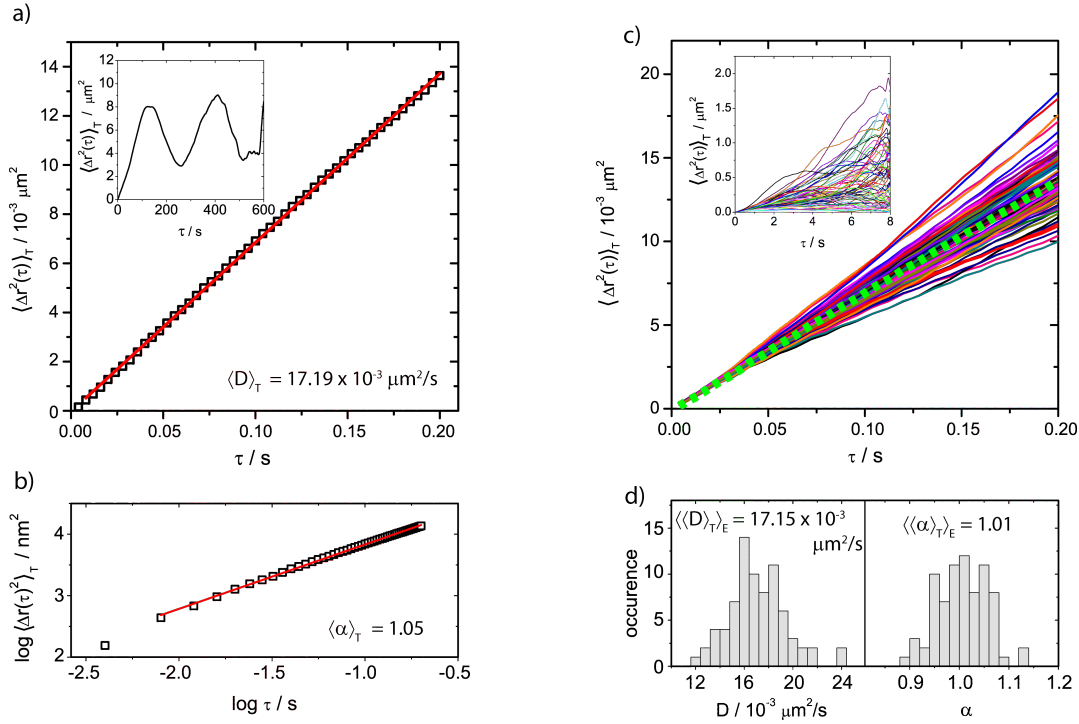


Figure 6.2: a) Time-averaged MSD of the full trajectory shown in fig. 6.1a. The inset displays the full MSD, while the main figure shows the first 50 data points. The red line corresponds to a linear fit to the data points. b) Double-logarithmic plot of the data shown in a). The red line corresponds to a linear fit with a slope of 1.05 c) MSDs of 76 subtrajectories that result from cutting the full trajectory into pieces of 2000 data points each. Similarly to part a) of the figure, the inset shows the full MSDs and the main figure displays the first 50 data points of each MSD. The dotted green line corresponds to the MSD curve shown in a). d) Distributions of the diffusion coefficient and the anomaly parameter as obtained from the MSDs shown in c).

hand, the MSD shown in fig. 6.2a was restricted to the first 50 data points corresponding to $\tau = 0.2 \text{ s}$. It is worth to note that even the 50th data point represents an average over more than 150000 entries. The full line in fig. 6.2a corresponds to a linear fit, which is in very good agreement with the data and from which a diffusion coefficient of $\langle D \rangle_T = 17.19 \times 10^{-3} \mu\text{m}^2/\text{s}$ is extracted. For this analysis, the first data point was neglected due to remaining experimental artifacts (oscillations of the piezo, details see publication P1). The notation $\langle D \rangle_T$ was used to indicate that this value stems from a time-averaged MSD according to equation 2.21. This number can be compared with the prediction from the Stokes-Einstein relation $D_{\text{SE}} = k_B T / 6\pi\eta a$ [5]. For $T = 294 \text{ K}$, $\eta = 1.2 \text{ Pa} \cdot \text{s}$ [39], and a mean bead radius of $a = 10 \text{ nm}$ as given by the manufacturer, $D_{\text{SE}} = 17.94 \times 10^{-3} \mu\text{m}^2/\text{s}$ was found. Although the agreement between $\langle D \rangle_T$ and D_{SE} is better than 5%, one can

argue that the discrepancy might reflect deviations of the radius of the bead from the value of 10 nm. Changing the point of view and taking the theoretical (Stokes-Einstein) diffusion coefficient as “real”, $a = 10.4$ nm for the actual size of the bead is found. Figure 6.2b shows the same data on a double logarithmic plot that can be fitted with a linear slope of $\langle\alpha\rangle_T = 1.05$, which is in line with the expected $\alpha = 1$ for Brownian motion and justifies the linear fit to the MSD data as explained in the theory part (section 2.1.3).

Often it is not possible to measure that long trajectories due to bleaching processes of the tracer particle, due to weak emission signals or simply, because the particle moves out of the detectable area. In order to mimic to have only shorter trajectories with less data points the long trajectory was chopped into 76 subtrajectories, also called segments, of 2000 data points each (corresponding to a time range of 8 s), see figure 6.1b. From these subtrajectories the time-averaged MSDs were calculated. The result for all 76 data sets is shown in the inset of figure 6.2c and reveals very large variations of the MSDs with respect to each other. For the same reasons as detailed above, figure 6.2c displays only the first 50 data points of the MSDs from all 76 subtrajectories. A bundle of linear MSDs that vary in slope was found. Since these data have been recorded from the same individual polymer bead it can be excluded that this spread reflects variations in the bead size. The different slopes rather result from the reduction of the statistical weight for the time-averaged MSDs of the subtrajectories. This is in line with the fact that the time-averaged MSD from the total trajectory of 1.52×10^5 data points runs nicely through the centre of the bundle of partial MSDs, as shown in figure 6.2c by the dotted green line for comparison. Analysing the slopes of the individual MSDs in terms of a diffusion coefficient and an anomaly parameter yields the distributions shown in figure 6.2d. The mean (empirical standard deviation) for the diffusion coefficient is $\langle\langle D \rangle_T\rangle_E = 17.15 \times 10^{-3} \mu\text{m}^2/\text{s}$ ($s_D = 2.39 \times 10^{-3} \mu\text{m}^2/\text{s}$) and for the anomaly parameter $\langle\langle \alpha \rangle_T\rangle_E = 1.01$ ($s_\alpha = 0.05$). The notation $\langle\langle \cdot \rangle_T\rangle_E$ symbolizes that the data have been evaluated from (short) time-averaged MSDs that have been averaged over an ensemble (here 76 subtraces).

The histograms presented in fig. 6.2d can be interpreted as the empirical probability density functions (PDFs) to measure a distinct range of values for these parameters. Mathematical statistics tells us, that the best estimator for the “real” value of the diffusion coefficient is provided from the first moment of this probability density which corresponds to $\langle\langle D \rangle_T\rangle_E$. The good agreement between the numerical values found for $\langle D \rangle_T$, i.e. the result from the full trajectory of 1.5×10^5 data points, and $\langle\langle D \rangle_T\rangle_E$ confirms that the statistical shortcomings of the trajectories with only 2000 data points are averaged out in the long trajectory. However, it shows as well that an accurate determination of the diffusion coefficient requires either a very long trajectory or knowledge about the (empirical) PDF for the outcome of an experiment on a shorter trajectory. A single experiment on a short trajectory is not sufficient and the result for the diffusion coefficient can differ by up to a factor

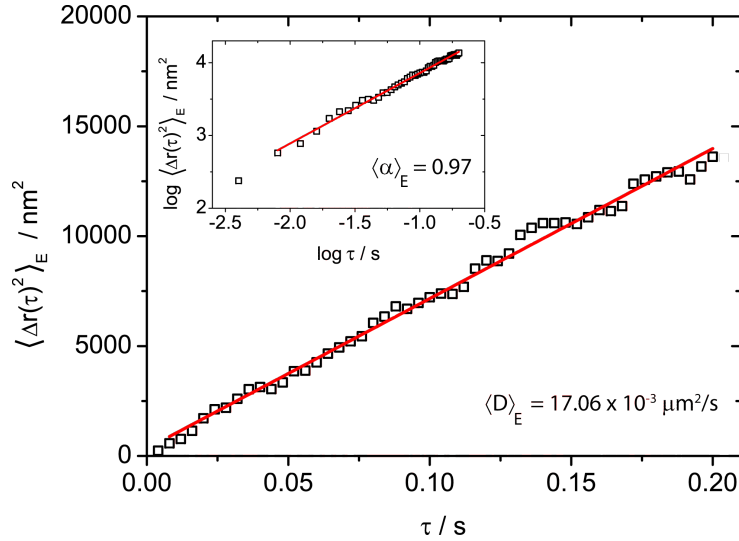


Figure 6.3: Ensemble-averaged mean squared displacement of the cut sequences of the single trajectory shown in fig. 6.1a. The inset displays the double-logarithmic plotted data, whereas the main figure shows the linear ones. The red solid lines are linear fits to the data points.

of 2.

Assuming that ergodicity is preserved, the cut sequences of the sub-ensemble can also be used to calculate the ensemble-averaged MSD according to the equation 2.22. This method is an alternative way to investigate a diffusion process, but is less suited for single trajectory experiments, because the number of traces for a statistical relevant ensemble, recorded under identical experimental conditions is mostly too small to yield proper results. However, for a comparison with the presented results also D and α were determined with this method. From line fits (red solid lines in fig. 6.3) to the linear as well as the double-logarithmic data $\langle D \rangle_E = 17.06 \times 10^{-3} \mu\text{m}^2/\text{s}$ and $\langle \alpha \rangle_E = 0.97$ was achieved (cf. fig. 6.3). Again both values fit quite well with the values determined by the above mentioned analysing methods. Slight differences stem from the rather weak ensemble. No violation of the ergodic principle is observed.

The presented MSD analysis was finally performed for all the seven measured trajectories. The results from the time-averaged MSDs ($\langle D \rangle_T$, $\langle \alpha \rangle_T$), the mean values of the ensemble of subtrajectories ($\langle \langle D \rangle_T \rangle_E$, $\langle \langle \alpha \rangle_T \rangle_E$) as well as the results from the ensemble-averaged MSDs ($\langle D \rangle_E$, $\langle \alpha \rangle_E$) are summarized in table 6.1. Beside the values obtained from the pure ensemble-average analysis, which are normally not used because of its weak statistics, all the values from the time-averaged analysis agree quite well with respect to each other. For all the following discussions regarding this sample (20 nm bead in glycerol), the measured normal Brownian motion with $\alpha = 1$ is used.

Exp. nr.	$\langle D \rangle_T /$ $10^{-3} \mu\text{m}^2/\text{s}$	$\langle \langle D \rangle_T \rangle_E /$ $10^{-3} \mu\text{m}^2/\text{s}$	$\langle D \rangle_E /$ $10^{-3} \mu\text{m}^2/\text{s}$	$\langle \alpha \rangle_T$	$\langle \langle \alpha \rangle_T \rangle_E$	$\langle \alpha \rangle_E$
1	17.19	17.15	17.06	1.04	1.01	0.97
2	21.58	21.64	21.03	1.02	1.02	0.99
3	16.70	16.60	17.71	1.03	1.01	0.96
4	17.49	17.47	18.18	1.04	1.01	1.15
5	15.01	14.98	14.95	1.05	0.94	0.91
6	24.14	24.10	24.57	1.04	1.01	1.02
7	12.32	12.34	13.30	1.01	1.04	9.94

Table 6.1: Summary of the diffusion coefficients and the anomaly parameters obtained from time-averaged as well as ensemble-averaged analysis. The entries are the time-averaged diffusion coefficient (anomaly parameter) $\langle D \rangle_T$ ($\langle \alpha \rangle_T$), the mean value determined from the ensemble of subtrajectories $\langle \langle D \rangle_T \rangle_E$ ($\langle \langle \alpha \rangle_T \rangle_E$) and the ensemble-averaged diffusion coefficient (anomaly parameter) $\langle D \rangle_E$ ($\langle \alpha \rangle_E$).

The analysis of single-particle trajectories with the use of the mean squared displacements (MSD) is the most common method. Among the here presented techniques of trajectory analysis, this is the only one, where the diffusion coefficient as well as the anomaly parameter can be determined. The most informations regarding a diffusion process can be extracted.

6.1.2 Alternative approaches

Cumulative distribution function

This method supplies an alternative approach to analyse a trajectory [37, 38]. According to the explanation in section 2.1.3 the empirical cumulative distribution function (CDF) for the square displacements at the lag times $\tau = 4 \text{ ms} - 0.2 \text{ s}$ ($\tau = (1 - 50)\Delta t$) was determined consecutively for a single trajectory. An example, calculated at a lag time of $\tau = 40 \text{ ms}$ is shown in fig. 6.4a (black squares). The data points can be modeled with a double-exponential function as given by

$$CDF(\Delta r^2, \tau) = 1 - \left(\beta \exp\left(-\frac{\Delta r^2}{\Delta r_1^2}\right) + (1 - \beta) \exp\left(-\frac{\Delta r^2}{\Delta r_2^2}\right) \right) \quad (6.1)$$

Here, the Δr_i^2 are related to a fast (1) and slow (2) component of the diffusion coefficient, i.e. $\Delta r_i^2 = 4D_i\tau$, weighted by a fraction β . For systems, where pure Brownian motion is present, β equals 1 and the CDF reduces to a single-exponential with a single diffusion coefficient $D_1 = D_{cdf}$. Yet, for systems showing subdiffusive behaviour β clearly differs from 1 and a double-exponential with a so called slow component of the diffusion coefficient (Δr_2^2) is better suited to describe the data. Hence, this method is powerful in distinguishing normal from anomalous diffusion, just by determining β . The afore mentioned fit function (eq. 6.1) was applied to

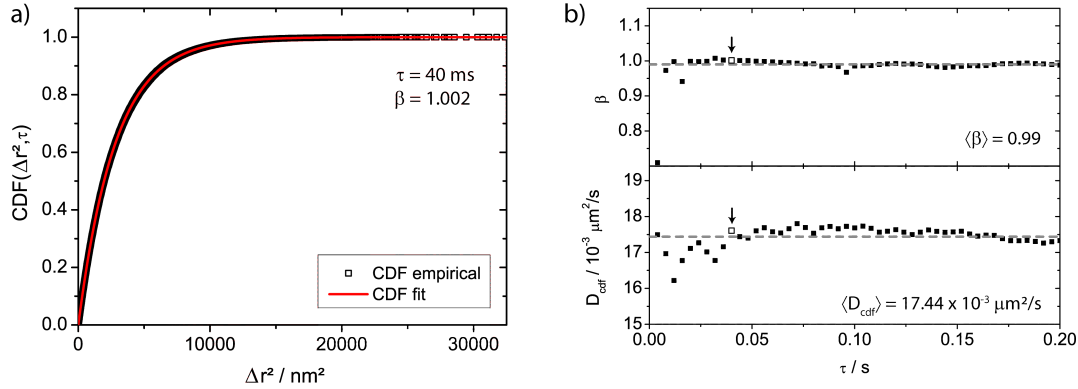


Figure 6.4: a) Example of a cumulative density function at a lag time of $\tau = 40$ ms. b) diffusion coefficient and fraction β taken from double-exponential fits to the empirical CDF. The arrow marks the values that correspond to the CDF shown in a). Due to remaining experimental shortcomings the first data point was neglected for the interpretation.

the data points (cf. fig. 6.4a, red solid line). The shown example ($\tau = 40$ ms) yields $\beta = 1.002$ which is in nearly perfect agreement with Brownian motion. The value of the fraction as a function of the lag time can be seen in fig. 6.4b, upper part. For this single trajectory on average a fraction of $\langle\beta\rangle = 0.99$ was found, which is close to unity and resembles Brownian motion with a single-exponential for the CDF. Further, the mean diffusion coefficient was calculated with this method to $\langle D_{cdf}\rangle = 17.44 \times 10^{-3} \mu\text{m}^2/\text{s}$, which is shown graphically in fig. 6.4b, lower part. The calculated value for the example CDF, shown in fig. 6.4a are marked with an arrow. Again, the first data points for $\tau = 4$ ms was neglected due to experimental shortcomings. Compared to the value obtained from the time-averaged MSD (cf. table 6.1, exp. nr. 1), a good agreement is achieved. This procedure was done for all the 7 recorded trajectories. The results can be found in table 6.2. From the overall average of the seven trajectories of the fraction $\langle\beta\rangle = 0.96$ one can conclude that the here used system reflects Brownian motion. Additionally, the diffusion coefficient fits quite well with the already determined ones from the mean squared displacement analysis. The slight discrepancy to theoretical/expected values can be addressed to the usage of partly uncorrected trajectory data (only the setup induced artifacts were corrected, i.e. the systematic error in the tracking algorithm and the (mis)alignment of the piezo stage) which was necessary for this evaluation. The advantage of this technique is the capability to study multi-component diffusion phenomena, e.g. a two-component diffusion can be interpreted as a slow and a fast mobility of the tracked particle. The fraction between these two mobilities can then be used to distinguish normal from anomalous diffusion. One has to be careful, that this fraction is not related to the anomaly parameter α . Another big advantage is, that this method can also be applied to relative short trajectories

Exp. nr.	$\langle\beta\rangle$	$\langle D\rangle_{cdf} /$ $10^{-3} \mu\text{m}^2/\text{s}$
1	0.99	17.44
2	0.90	22.15
3	0.98	16.81
4	0.92	18.19
5	0.97	16.46
6	1.01	24.05
7	0.97	11.98

Table 6.2: Summary of the results from the analysis according to the cumulative distribution function from 7 individual polymer beads. The entries denote the experiment nr., the fraction $\langle\beta\rangle_T$, and the diffusion coefficients $\langle D\rangle_{cdf}$.

with a few position determinations [37].

Spatial extend & shape

Another method to extract information from a tracking experiment is to determine the spatial extend by means of a gyration ellipse around a trajectory and its shape, i.e. the asphericity. The method, how to calculate this value is discussed in detail in section 2.1.3. In fig. 6.5a the gyration ellipse with its radii of gyration is overlaid to a representative trajectory with $N = 1.52 \times 10^5$ data points. The overall spatial extend of the trajectory is rather elongated than circular. The latter one would be expected for a perfect random walk and holds true for an ensemble of traces. But, for a single trajectory the elongated version is found [35]. This behaviour is better described by the shape of the trace instead of the spatial extend, which can vary (mainly) due to the mobility of the particle and the length of the trajectory. The shape is determined by the asphericity, which is a measure for the deviation from a spheric (3D) or a circular (2D) shape. According to eqn. 2.26 the asphericity A of an individual trajectory is calculated for a certain length (number of positions N_{seg}) of cut segments. (As a reminder, the calculation of A requires averaging over an ensemble of traces.) It is quite hard to decide, at which segment length the value of A is reliable. Therefore the asphericity of a trace was calculated as a function of the length N_{seg} , i.e. $A(N_{seg})$. The result of the 7 individual measured traces is shown in fig. 6.5b. For a segment length of $N_{seg} = 2$ the shape of the trajectory is perfect rod-like and leads a value of $A(2) = 1$. Within the first 15 data points the asphericity converges towards a value of $A = 4/7$ (grey line in fig. 6.5b), that is the analytical value for a 2-dimensional random walk [35, 36]. To verify this behaviour for the here presented measurements in a more quantitative way, a statistical relevant window (grey shaded area in fig. 6.5b) for the calculation of a mean asphericity $\langle A \rangle$ was chosen. This region was restricted to $20 \leq N_{seg} \leq 250$ where at the one end ($N_{seg} > 20$) $A(N_{seg})$ is regarded as fully converged and on the other

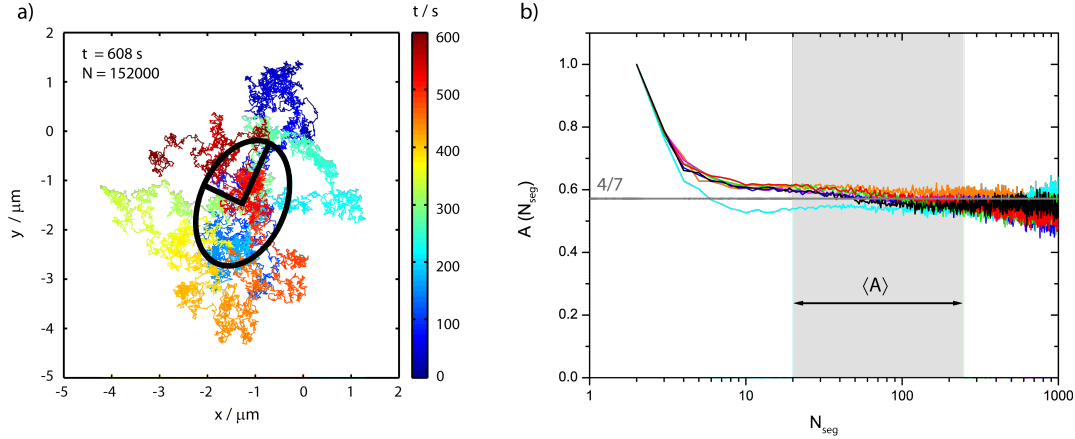


Figure 6.5: Asphericity of all trajectories plotted against the sequence length N_{seg} . The grey shaded region is the window, where the asphericity is averaged. The grey solid line represents the analytical value for a 2-dimensional random walk, i.e. $A=4/7$.

hand ($N_{seg} < 250$) the averaging in calculating the asphericity is high enough. The values for the 7 experiments are summarized in table 6.3. On average, the mean asphericity was determined to $\langle A \rangle_7 = 0.566$ which is in very good agreement with the analytical value of $A = 4/7 \approx 0.571$ for a Brownian motion. The index 7 indicates the average over all seven experiments. The nearly perfect coincidence reflects furthermore, that no significant signs of drift or flow is overlaid to the trajectories that would lead to a distortion and concomitantly influence the asphericity. For the investigation of systems showing anomalous diffusion, this method can be used to clarify the type of sub-diffusion, which is described in publication P3 (see part II).

With this method, neither the diffusion coefficient nor the anomaly parameter can be determined. Hence, it yields minimal informations about a diffusion process. But, in addition to the time-dependent parameters (D , α) a structural parameter

Exp. nr.	$\langle A \rangle$
1	0.555
2	0.575
3	0.564
4	0.563
5	0.540
6	0.569
7	0.595

Table 6.3: Summary of the determined mean asphericities $\langle A \rangle$ of the seven individual trajectories.

is obtained, that describes the deviations from a circular shape (in case of a 2D trajectory). In combination with the anomaly this technique is powerful in investigating subdiffusive behaviour, e.g. of crowded fluids like it is discussed in section 6.4 of this thesis.

Ergodicity breaking parameter

Recently a technical parameter for determining the degree of ergodicity breaking has been published [51, 52].

$$E(\tau) = \frac{\left\langle \left\langle \Delta \mathbf{r}(\tau)^2 \right\rangle_T^2 \right\rangle_E - \left\langle \left\langle \Delta \mathbf{r}(\tau)^2 \right\rangle_T \right\rangle_E^2}{\left\langle \left\langle \Delta \mathbf{r}(\tau)^2 \right\rangle_T \right\rangle_E^2} \quad (6.2)$$

The calculation of this ergodicity breaking parameter $E(\tau)$ requires again an ensemble of short trajectories, that can be obtained by splitting a long trace into short segments with equal length. From these short segments the time-averaged MSDs are calculated. According to equation 6.2 the time-averaged MSDs, i.e. $\langle \Delta \mathbf{r}(\tau)^2 \rangle_T$, are on the one hand squared and then ensemble-averaged, symbolized by $\langle \cdot \rangle_E$, and on the other hand first ensemble-averaged and then squared. For values of E close to 0 the system is regarded as non ergodicity breaking [51, 52].

In an analog way to the determination of the asphericity the ergodicity breaking parameter was calculated. For averaging $E(\tau)$ we used a time window that corresponds to the analysis of the diffusion coefficient and the anomaly parameter (2-50 data points). The results for the averaged ergodicity breaking parameter $\langle E \rangle$ of every single trajectory is listed in table 6.4. All values are smaller than 0.020 which is interpreted as non-ergodicity breaking, compared to values found in the literature for weak ergodicity breaking system. There, $E = 0.57$ [51] and hence a factor of more than 20 times larger than the here obtained values. This additional parameter reflects the expected Brownian motion, where ergodicity is preserved.

Exp. nr.	$\langle E \rangle$
1	0.017
2	0.019
3	0.020
4	0.020
5	0.018
6	0.017
7	0.020

Table 6.4: Summary of the determined mean ergodicity breaking parameter $\langle E \rangle$ of the seven individual trajectories.

6.2 Accuracy of diffusion coefficients

How well a diffusion coefficient can be determined by a mean squared displacement analysis of experimental single-particle trajectories is an important issue. In the previous chapter it was explained, that long trajectories results in accurate diffusion coefficients. However, one can imagine, that not only the length of the trajectory is important, also uncertainties in the position determination or the number of fitting points used in the MSD analysis have an effect on the accuracy of the measured diffusion coefficient. To what extend these parameters influence the accuracy is discussed in great detail in the literature on the basis of simulations and numerical calculations [53–55]. First it was studied by Qian and Saxton and was further developed and subtilized by Michalet who took also experimental localisation errors into account. Up to now a comparison with experimental data remained elusive. In this section the problem is treated from the experimental point of view and the results were compared with the predictions made in the afore mentioned literature. The findings were published in *Physical Chemistry Chemical Physics* (see publication P2). In the following I will give a summary of this work.

Many studies that use single-particle tracking to investigate diffusion processes, especially in the field of biophysics, often lack of sufficiently long trajectories, either because the particle diffuses out of the detectable area or due to photobleaching of the fluorescent tracer particles. Hence, the MSD points of a trajectory are less averaged which results in a less accurate diffusion coefficient. In order to investigate this accuracy, many trajectories are required to perform a statistical analysis. Usually, it is not possible to acquire a statistically relevant number of trajectories with identical experimental conditions. While it is rather simple to keep the viscosity and temperature between several independent tracking experiments constant, the bead size determined from each recorded trajectory can vary drastically. Therefore, in the literature simulations with a high number of fictitious trajectories with identical parameters (trajectory length N , temperature T , viscosity η , bead radius a) were used to clarify this issue [53–55]. In this work an experimental approach to measure the accuracy of a diffusion coefficient is presented.

Exploiting single-particle orbit tracking, very long trajectories comprising more than $N = 1.5 \times 10^5$ data points were recorded from individual 20 nm sized particles in glycerol that undergo Brownian motion. Each of these large data sets can be decomposed into an ensemble of segments with a various number of data points N_{seg} , providing the same ensemble of mean squared displacement curves from the same individual particle. By a linear fit to each MSD curve of an ensemble with a given value of N_{seg} , the slopes D^* as a function of the number of fitting points n were determined (n starts from the MSD point 2 and ends at $n + 1$, details see publication P2). Subsequently for each value of n , the relative error $s_{D^*}/\overline{D^*}$ was calculated from the histograms of the slopes and plotted against each other. Here, the (empirical) mean $\overline{D^*}$ and standard deviation s_{D^*} were determined. Figure 6.6

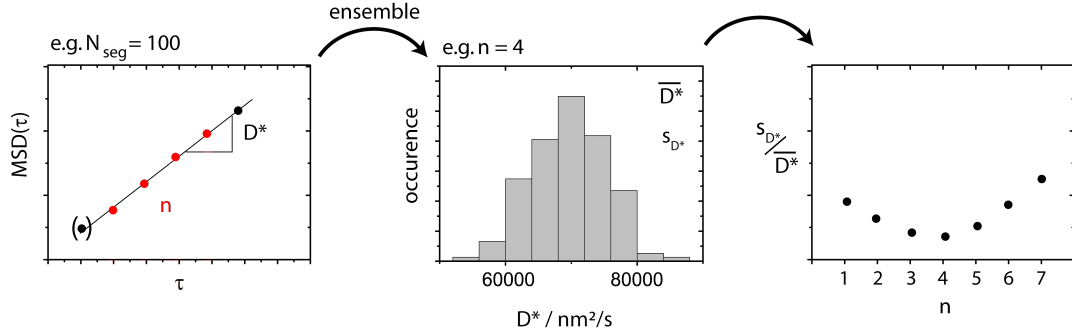


Figure 6.6: Schematic explanation to determine the accuracy of the slope of MSD curves. Left: A single MSD curve. The number of fitting points is highlighted in red. Middle: Histogram of slopes D^* . Right: Representation of the relative error of slopes as a function of the number of fitting points n . Adapted from publication P2.

displays this calculation procedure schematically. Instead of the diffusion coefficient, the slope was determined to be comparable with literature data ($D^* = 4D$). The calculation of the relative error of slopes was performed for a segment length of $N_{seg} = 100$ and $N_{seg} = 1000$. The existence of an optimum number of fitting points, i.e. $n = 4$, was found, where the relative error of the slopes features a minimum. Interestingly, this minimum is independent on the segment length. A relative error of about 25% for a segment length of $N_{seg} = 100$ data points was found, whereas an accuracy of about 8% requires trajectories with a length of $N_{seg} = 1000$ data points.

Moreover, the distributions of diffusion coefficients were studied as a function of the length of the segments. For a length of $N_{seg} = 10$ data points the distributions are very broad and an interpretation is useless. The diffusion coefficients determined from trajectories with $N_{seg} = 100$ can still vary by more than a factor of 2.

This analysis shows that the accuracy of measuring a diffusion coefficient depends on the length of a trajectory and on the number of fitting points that are used for a linear fit to the MSD data points. All the findings yield qualitatively and quantitatively a good agreement with theoretical and numerical predictions found in the literature.

6.3 Particle sizes

In the previous section, the influence of the trajectory length and the number of fitting points, that are used for a linear fit to the MSD curve, were discussed regarding the accuracy of measuring a diffusion coefficient. Having the optimal number of $n = 4$ fitting points for the here presented experiments, the MSD analysis was applied to all seven trajectories, each comprising about 1.5×10^5 positions. The

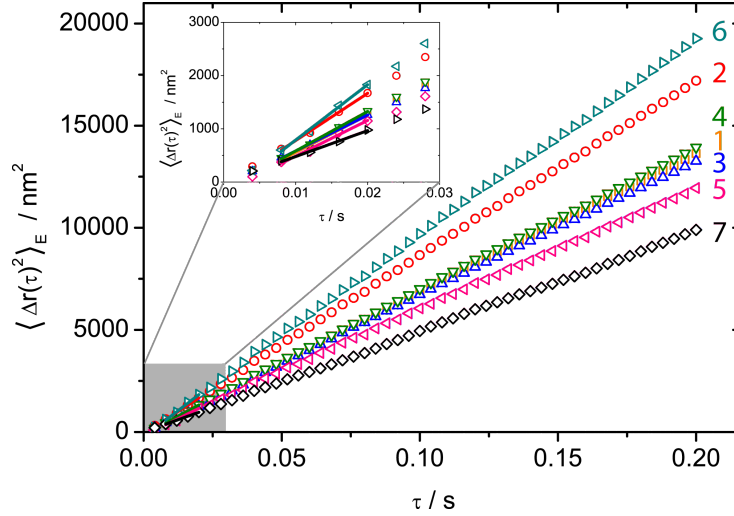


Figure 6.7: Time-averaged MSDs (first 50 data points) of the 7 individual trajectories from 20 nm sized beads diffusing in pure glycerol. For each bead, trajectories were recorded for 10 minutes with a time increment of $\Delta t = 4$ ms. The inset displays the first 7 MSD points and the linear fits (full lines) to the data with $n = 4$ fitting points, i.e. using the points 2-5.

first 50 data points of the MSDs from each trajectory are shown in fig. 6.7. The data are compatible with linear fits ($n = 4$), that vary in slope. The respective time-averaged diffusion coefficients, $\langle D \rangle_T$ extracted from these data are summarized in Table 6.5. The diffusion coefficients $\langle D \rangle_T$ show strong variations and cover the range from $12 \times 10^{-3} \mu\text{m}^2/\text{s}$ to $24 \times 10^{-3} \mu\text{m}^2/\text{s}$. Since all 7 MSDs represent highly averaged data it is very unlikely that these variations result from a lack of statistics (as for example the variations discussed in the context of fig. 6.2c). It is much more probable that the variations reflect the differences in the size of the individual beads that have been traced, hence the values for the diffusion coefficients are interpreted as the “correct” values.

Using the diffusion coefficient $\langle D \rangle_T$ as input for the Stokes-Einstein relation, the actual size of the polymer beads can be calculated according to

$$\langle a \rangle_T = \frac{k_B T}{6\pi\eta \langle D \rangle_T}. \quad (6.3)$$

The results for the particle radii $\langle a \rangle_T$ are listed also in table 6.5, featuring an arithmetic mean of 10.14 nm and a standard deviation of 2.47 nm as best estimators to characterize the distribution of bead sizes. These numbers are in reasonable agreement with the information provided by the manufacturer ($a = (10 \pm 2)$ nm). To illustrate the importance of the previously discussed influence of the number of fitting points used for the MSD curve to extract the diffusion coefficient, a comparison between $n = 50$, a putative good value which was chosen due to the highly

Exp. nr.	$\langle D \rangle_T /$ $10^{-3} \mu\text{m}^2/\text{s}$	$\langle a \rangle_T /$ nm	$\langle \langle a \rangle_T \rangle_E /$		$\langle \langle a \rangle_T \rangle_E /$	
			nm	$s_a /$ nm	nm	$s_a /$ nm
			$n = 50$		$n = 4$	
1	17.45	10.3	10.7	1.5	10.4	0.6
2	22.20	8.1	8.5	1.3	8.2	0.5
3	16.86	10.6	11.0	1.5	10.7	0.6
4	18.54	9.7	10.5	1.6	10.0	0.5
5	16.76	10.7	12.3	1.9	10.9	0.7
6	26.02	6.9	7.6	1.2	7.3	0.4
7	12.19	14.7	14.9	2.5	16.1	0.9

Table 6.5: Summary of the results from the MSDs from 7 individual polymer beads. The entries denote the diffusion coefficient $\langle D \rangle_T$ from the time-averaged MSDs from the long trajectories, the corresponding bead radius $\langle a \rangle_T$ as obtained from the Stokes-Einstein relation and the mean values $\langle \langle a \rangle_T \rangle_E$ and empirical standard deviations s_a of the distribution of particle radii, calculated from the diffusion coefficients of the set of time-averaged MSDs from the short trajectories. The latter two values are given for $n = 50$ and $n = 4$ fitting points of the MSD curves.

averaged data, and the optimal value of $n = 4$, is discussed for the particle sizes in the following. In order to do so, each of the 7 long trajectories were cut into segments of $N_{seg} = 2000$ data points. Subsequently, the time-averaged diffusion coefficient was determined from each subtrajectory which was used to calculate the particle radius with equation 6.3. The distributions of particle radii are shown in fig. 6.8 for the 7 tracking experiments, each carried out on a different particle. In fig. 6.8a and b the results for a number of fitting points of $n = 50$ and of $n = 4$ are displayed, respectively. These histograms can be interpreted as empirical probability density functions for measuring a particle radius within a distinct range in one of the experiments. The statistical parameters, i.e. the mean and the empirical standard deviation, of these histograms are given in the figure and in table 6.5. It can be seen directly, that the distributions for $n = 4$ fitting points are much narrower than the one for $n = 50$ fitting points. Comparing the mean values $\langle \langle a \rangle_T \rangle_E$ obtained with $n = 50$ and $n = 4$ fitting points with the radii $\langle a \rangle_T$ that have been determined from the long trajectories, the data set with $n = 4$ yields a much better agreement with the radii $\langle a \rangle_T$. Also the width of the histograms for $n = 4$ fitting points is a factor of 2 smaller than the width of the data set extracted with $n = 50$ fitting points. However, this means that in a single tracking experiment that covers about 2000 data points in 2/3 of the cases the radius of a particle can be determined with an accuracy of about $s_a / \langle \langle a \rangle_T \rangle_E \approx 15\%$ for $n = 50$ fitting points and of about $s_a / \langle \langle a \rangle_T \rangle_E \approx 6\%$ for $n = 4$ fitting points. The chance of measuring the “true” particle radius increases tremendously, just by choosing the optimum region for fitting the MSD curves.

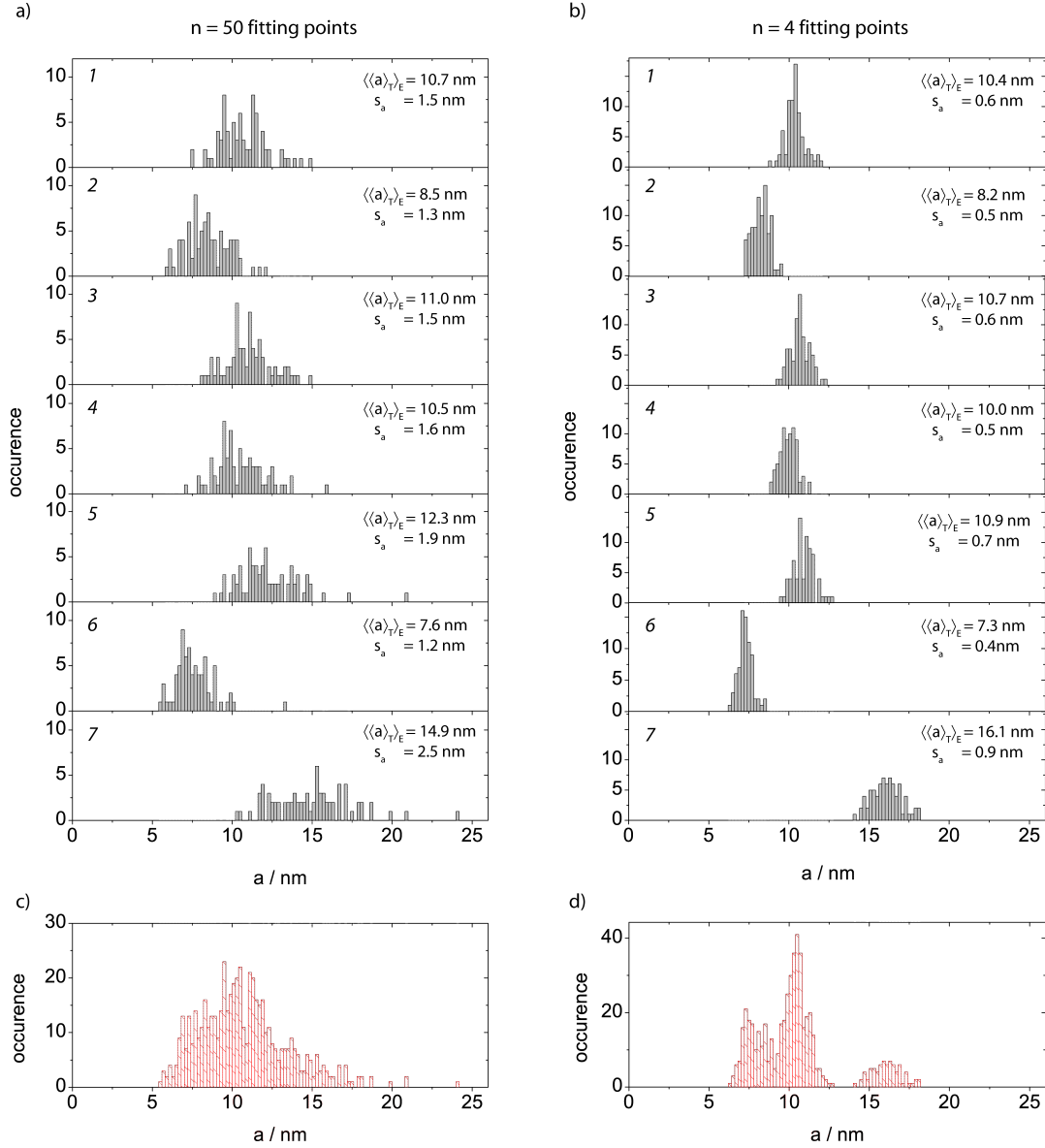


Figure 6.8: Empirical probability density functions to find a distinct bead size from one subtrajectory for $n = 50$ (a) and $n = 4$ (b) fitting points. Each histogram in a) and b) corresponds to one of the 7 different beads that have been measured individually. The means $\langle\langle a \rangle\rangle_E$ and (empirical) standard deviations s_a of these distributions are given in the figure. c) and d) are the added histograms of a) and b), respectively.

Naively, one can combine all the measured particle radii from all experiments to one single histogram. This is shown in figure 6.8 c) and d) for $n = 50$ and $n = 4$ fitting points, respectively. While a clear structure for the case of $n = 4$ is found, the distribution for $n = 50$ fitting points is broad and featureless. This reflects again

the importance of the choice of the number of fitting points. The different particle sizes can be distinguished if the optimal number of fitting points is considered.

Apparently, in particle tracking the experimentally determined sizes of the particles reflect the convolution of several distributions. The first contribution comes from the real distribution of the particle size around a mean with a distinct width. This distribution exists in the real world and would be ideally the result of an experimental study. However, for each particle that is studied this distribution is convoluted with the empirical probability density to measure a distinct size for this particular bead. The latter distribution reflects the statistics of the experiment and can be narrowed down by taking longer trajectories and a proper region for fitting the MSD data points. Only if the widths of these empirical distributions become sufficiently narrow their contributions to the experimental result can be neglected. This is what is assumed above where the parameters obtained from the long trajectories with an optimal number of fitting points ($\langle D \rangle_T$ and $\langle a \rangle_T$) were interpreted to characterize the real distribution function of the particle size. The broadening of the distribution due to the statistical analysis is negligible.

These findings touch upon an important issue because commercial applications have been developed that measure the size distributions of nanoparticles by particle tracking [56]. In those experiments typically a large number of short trajectories (each in the order of some hundreds of data points [57]) are measured. Then from each trace a diffusion coefficient and the corresponding size of the particle is determined. As demonstrated here, the problem with this approach is that the experimental outcome of a single experiment can already vary significantly, represented by the probability density functions as shown in fig. 6.8. Unfortunately, information about these PDFs are usually not accessible. Since each trajectory stems from a different particle, and since the particles can vary in size, ensemble averaging over many trajectories will not be helpful either. The importance, however, of having reliable information about size distributions of nanoparticles is an emerging field in the context of health protection, in particular if one considers that up to now a well characterised safety protocol regarding the toxicity for the use of nanoparticles is still not in sight [58].

6.4 Crowded Fluids

All the previously presented results were obtained from measurements on a fluid that exhibits normal Brownian motion. The intention was to characterize the setup and to learn more about the statistical data analysis. In the following the results on a more complex fluid are introduced, where non-Brownian motion is expected. The cell membrane as well as intracellular fluids inhibit a variety of macromolecules, that are responsible for the transport processes within a cell, among which (bio)-chemical reactions play an important role. The high density of these molecules

influences the diffusion of the reaction partners enormously. Hence, anomalous diffusion due to macromolecular crowding is a non-neglectable process in describing the reaction kinetics in cells. Due to the hindered motion of the diffusing particles, a subdiffusive process is expected. Several theoretical models have been proposed, that target this issue, where the three most prominent ones are i) obstructed diffusion (OD) [59], ii) continuous time random walk (CTRW) [51, 60] and iii) fractional Brownian motion (FBM) [61–63]. The model of obstructed diffusion is a very simple one and describes the motion of a particle on a grating with random positioned obstacles. It can be compared with a blind ant on a percolation grating. The CTRW model is the random walk of a tracer particle with power-law distributed residence times. In other words it is regarded as a Lévy flight in the time domain. And finally the theory of FBM considers viscoelastic forces that hinders the particle on free diffusion. The motion is anti-correlated, i.e. a memory is present.

Until now it was impossible to decipher, which one of these models is best to describe the process of crowding induced subdiffusion, because experimental verification was missing. In cooperation with the chair of experimental physics I of the University of Bayreuth (group of Prof. Dr. M. Weiss), the type of the diffusion in a crowded fluid was investigated experimentally. The results of this study were published in the journal *Soft Matter* with the title “Fractional Brownian motion in crowded fluids”, which can be found in part II of this thesis (publication P3). Here, I will give a summary of this work and provide additional information with respect to the used sample.

Measurements in a cell or a biological membrane needs high experimental requirements. Therefore, a simpler approach was chosen by mimicking the natural system of a cell plasma by a fluid called dextran, which shows similar behaviour. Dextran is forming a highly branched network structure and serves as a model system for crowded fluids (see section 3). To clarify, that the results obtained with dextran are not just an experimental artifact, a chemically similar sample (sucrose) that shows normal Brownian motion, was investigated as a reference.

For all previously introduced experiments a bead size of 20 nm was used. By using these beads also for the measurements in dextran, only a very weak subdiffusive behaviour was observed. Subsequently, the tracking experiments were performed on 20 nm and 50 nm beads to check if there exists a size dependence regarding the subdiffusive behaviour. The results are shown in figure 6.9, where the full symbols corresponds to the 20 nm sized beads and the open symbols to the 50 nm sized beads, measured in sucrose (blue) and in dextran (red). About 20 trajectories for each combination were measured. The anomaly parameter was determined via a mean squared displacement analysis from the long trajectories. To calculate the radii of the particles from the diffusion coefficient, the viscosity is required. Because no suitable values were found in the literature, the anomaly parameter was plotted against the inverse of the diffusion coefficient, which represents a proportionality to the particle size, if the measurements are performed in the same sample fluid,

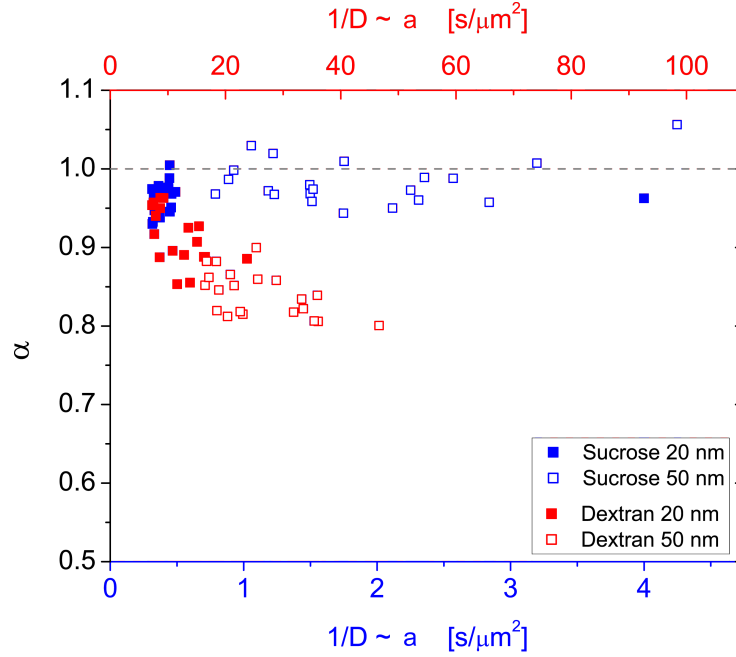


Figure 6.9: Results of the anomaly parameter α as a function of the determined bead radius a . The full blue (red) squares are the nominal 20 nm sized beads in the sample sucrose (dextran), while the open blue (red) squares are the nominal 50 nm beads in sucrose (dextran). The grey line serves as a guide for the eye.

i.e. the viscosity stays constant (see equation 6.4).

$$\frac{1}{D} = \frac{6\pi\eta}{k_b T} a = \gamma a \quad (6.4)$$

This presentation is suitable enough, because only the dependence in the particle sizes and not the absolute values for the radii are important. The experiments were performed in two fluids with different viscosities, i.e. for a proper visualization two x-axis were introduced, where the bottom (blue) axis in figure 6.9 corresponds to the measurements in sucrose and the top (red) axis to the measurements in dextran. To compare the two data sets, the axis were further scaled according to the smallest measured values of $1/D$ for the nominal 20 nm sized beads. Despite the nominal values of 20 nm and 50 nm for the bead sizes a distribution was determined, which was discussed in detail in section 6.3. For this measurement, a broad distribution was helpful, because the size effect on the diffusion behaviour was studied. The measurements in sucrose showed independent of the size of the beads an anomaly value close to 1, while the measurements in dextran showed a clear dependence on the size of the beads. However, all measurements for the 50 nm sized beads in dextran showed an unambiguous subdiffusive behaviour. The mean anomaly values for the 50 nm sized beads were determined to $\langle \alpha_{suc} \rangle = 0.98$ for sucrose and

to $\langle \alpha_{dex} \rangle = 0.82$ for the crowded dextran solution. The clear separation between these two values is evident, i.e. the subdiffusion is not just an artifact. A plausible explanation is the size ratio of the beads and the mesh size of the dextran network. Small beads can diffuse nearly freely through the network structure, while larger particles are hindered. Hence, in the following only the data obtained for the measurements with bead sizes of 50 nm are discussed.

The experimentally determined trajectories of the 50 nm sized beads in dextran were compared with simulated trajectories based on the three theoretical models mentioned afore. These models have in common, that they can describe subdiffusion. But, while the CTRW model shows slight ergodicity breaking according to the recently developed ergodicity breaking parameter [51, 52] (see eq. (6.2), the other two models do not. Also the analysis of the experimentally measured trajectories do not show any signs of ergodicity breaking. This rules out the CTRW model for a proper description of the crowding induced subdiffusion in dextran. The remaining two models (OD and FBM) show ergodic behaviour and therefore another criterium has to be found to decipher between those two theories.

The idea is to calculate the asphericity A and the anomaly α of experimentally determined trajectories and compare those results with the results obtained from simulated trajectories that repose on the theories of OD and FBM. For these simulations, trajectories with α values between 0.5 and 1.0 were generated and the asphericity was calculated subsequently, yielding the asphericity as a function of the anomaly, i.e. $A(\alpha)$. This analysis was performed in the group of the cooperation partner. The details are described in the publication P3. The mean values of the experimentally determined anomaly and asphericity are $\langle \alpha \rangle = 0.82$ (*vide supra*) and $\langle A \rangle = 0.46$, respectively. For the comparison, the α value from the experiment (0.82) was inserted in both functions $A(\alpha)$, obtained by the simulations with OD and FBM. This yields $A_{OD} = 0.56$ and $A_{FBM} = 0.47$. A nearly perfect agreement between the experimental data and the model of fractional Brownian motion was obtained.

With this work a clear statement regarding the theoretical description of a subdiffusive process in a complex fluid was made, which helps to better understand the reaction kinetics in living cells. It is worth to note, that it is of crucial importance for the analysis of the experimental data to measure very long trajectories with a high spatial and temporal accuracy. Having those data a comparison with simulations was possible.

The future belongs to those who believe in
the beauty of their dreams

Eleanor Roosevelt

7 Outlook

The described experimental setup for single-particle orbit tracking, the data analysis and the applications are on a level where fascinating experiments and investigations can be performed. The setup is well characterised and first results showed its capability. But some improvements in all of the mentioned fields are helpful to push this research forward and to get a highly developed setup. In the following a short outlook for possible applications and setup improvements are given.

Instead of concentrating on tracking experiments in the research sector of biophysics, where most of the groups are working, the field of material sciences can be investigated, where tracking of single nanoobjects can help to better understand processes on a nanometer length scale. For example the switching behaviour of a liquid crystal is challenging when working on a submicrometer scale. If traceable molecules or particles can be attached to the molecules of a liquid crystal, the time-dependent motion of these molecules can be recorded with a high precision. This would help to better understand the phase transition of liquid crystals. Further, if molecules with a defined transition dipole moment are used, also the rotational diffusion can be investigated.

Another possibility to use particle tracking in material sciences is the examination of diffusion processes through nanoporous membranes. Recently successful experiments were published, where the diffusion through switchable nanopores that vary in size were measured [64]. With the single-particle tracking experiments, the structure of the pores can be determined, with a resolution far beyond the diffraction limit of light. This helps to construct filter systems on a micro- and even nanometer scale.

With the here presented setup, at the moment only 2-dimensional tracking experiments can be performed with a high spatio-temporal resolution. But with a lower time resolution also 3-dimensional trajectories can be recorded. The 3rd dimension becomes accessible through the z-tracking algorithm. Here it was only used to keep the particle of interest in the focal plane, but the algorithm stores the z-position of the particle with a lower time resolution. In figure 7.1 the 3-dimensional trace with a number of $N = 15000$ positions of a 20 nm sized bead, diffusing in glycerol is shown for a time resolution of $\Delta t = 40$ ms, which is a factor of 10 slower than

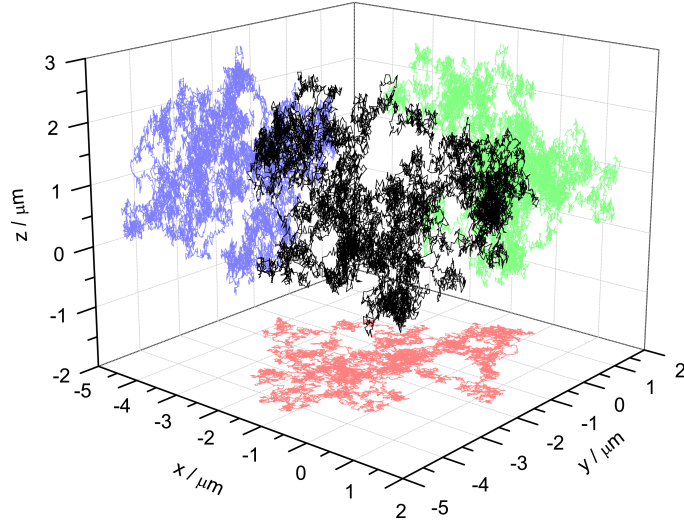


Figure 7.1: 3-dimensional trajectory of a single particle with a size of 20 nm, that diffuses in the fluid glycerol. The trace consists of $N = 15000$ data points with a time resolution of $\Delta t = 40$ ms. The green, blue and red trajectory corresponds to the projections to the xz , yz , and xy plane, respectively.

the rest of the results. Regarding the position accuracies of the z -position, this has to be investigated in a future work, the 2-dimensional accuracy (xy plane) is the same like in the presented work (≈ 10 nm). To improve also the temporal resolution for the z dimension, a fast scanning in this direction has to be implemented. One option is to install a third AOD, that is responsible for the generation of a second light orbit. The optics has to be aligned in a manner, that one of the light orbits is slightly above the particle and the other is slightly below. By switching the excitation intensities of these two orbits periodically on and off with a different frequency than the one used for the focus rotation, in an analog way the z -position of the particle can be calculated by demodulating the emission signal.

The temporal resolution of all of the axis can be improved by implementing a beam scanning technique, rather than sample scanning with the piezo. By moving the laser beam with the AODs a much higher temporal resolution should be obtained, because no mechanical elements restrict the scanning mechanism.

These were just some improvements that can be done to bring the setup to a new level. Especially with the higher time resolution, diffusion processes on a faster time scale becomes accessible.

Appendix

A Program code

In the following the Matlab source code for the generation of the “simulated real” and “simulated reconstructed” trajectories is displayed.

```
1
2 % Simulation of the "real" and the "reconstructed" trajectory
3 % *****
4
5 clc;
6 clear;
7 format long
8 nr_trace=1;
9
10 %**** tracking parameter *****
11 dt=2E-6;           %sampling time [s]
12 f=1000;           %orbit frequency [Hz]
13 ro_x=190E-9;      %orbit radius x [nm]
14 ro_y=190E-9;      %orbit radius y [nm]
15 w=270E-9;         %1/e^2 of focus [nm]
16 gb=500;           %background emission [cps]
17 g0=450000;        %emission in the focus
18 omega=2*pi*f*dt;  %orbit frequency
19 s=100;            %samples (length of trajectory)
20
21
22 for i2=0:nr_trace-1
23
24     %**** diffusion parameter *****
25     eta=1.2;        %viscosity [Pas]
26     r=10E-9;        %radius of sphere [m]
27     kb=1.3806504E-23; %Boltzmann constant [J/K]
28     T=294;          %Temperature [K]
29     g=6*pi*eta*r;   %friction coefficient (Stokes)
30     fc=sqrt(2*kb*T/g/dt); %prefactor stochastic force
31     D=kb*T/g;       %diffusion coefficient
32     P=4;            %orbit periods
33     a=P/(f*dt);     %sampling intervals
34     tr=P/f;         %time resolution [s]
35
36
37     %**** initial values *****
38     x=0E-9;         %x of "real" trace
39     y=0E-9;         %y of "real" trace
40     dx=0;           %x step of "real" trace
41     dy=0;           %y step of "real" trace
42     xc=0;           %x of "reconstructed" trace
43     yc=0;           %y of "reconstructed" trace
44     dxc=0;          %x step of "reconstructed" trace
45     dyc=0;          %y step of "reconstructed" trace
46     xs=0;           %x of piezostage
47     ys=0;           %y of piezostage
48     x_a=zeros(1,s); %array for "real" x values
49     y_a=zeros(1,s); %array for "real" y values
```

```

50 xc_a=zeros(1,s); %array for "reconstructed" x values
51 yc_a=zeros(1,s); %array for "reconstructed" y values
52 time=zeros(1,s); %array for time
53 int=zeros(1,s); %array for intensity
54 randn('state',sum(1000*clock));
55
56
57 ** generation of the "real" and "reconstructed" trace *
58 for i3=1:s
59
60     S=zeros(1,a); %theoretical nr. of photons
61     Sp=zeros(1,a); %poisson dist. nr. of photons
62     Scos=zeros(1,a);
63     Ssin=zeros(1,a);
64     cos_v=zeros(1,a);
65     sin_v=zeros(1,a);
66
67
68     for n=1:a
69         %***** "real" trajectory *****
70         fs_x=randn;
71         fs_y=randn;
72
73         dx=fs_x*fc*dt;
74         dy=fs_y*fc*dt;
75
76         x=x+dx;
77         y=y+dy;
78
79         %***** "reconstructed" trajectory *****
80
81         S(n)=dt*gb+dt*g0*exp(-2/w^2*((x-xs-ro_x*cos(omega*n))^2+
82         (y-ys-ro_y*sin(omega*n))^2));
83         cos_v(n)=cos(omega*n);
84         sin_v(n)=sin(omega*n);
85     end
86
87     x_a(i3)=x*1E9;
88     y_a(i3)=y*1E9;
89
90     Sp=poissrnd(S);
91     Scos=Sp.*cos_v;
92     Ssin=Sp.*sin_v;
93
94     %***** calculation of the position *****
95
96     if (sum(Sp)==0)
97         dxc=0;
98         dyc=0;
99     else
100         dxc=w^2/(2*ro_x)*sum(Scos)/sum(Sp);
101         dyc=w^2/(2*ro_x)*sum(Ssin)/sum(Sp);
102
103         xc=xc+dxc;
104         yc=yc+dyc;
105
106         xc_a(i3)=xc*1E9;
107         yc_a(i3)=yc*1E9;
108
109         %***** feedback mechanism *****
110         xs=xc;
111         ys=yc;
112

```

```

113 %***** time and intensity *****
114
115 time(i3)=i3*tr;
116 int(i3)=sum(Sp)/tr;
117
118 end
119 end

```

B Harmonic approximation

In this section the derivation of the harmonic modulation of the emission signal for particle positions close to the centre of the light orbit is shown. Therefore equation (2.28) from the section 2.2.2 is used.

$$I(t) = I_0 \exp\left(-\frac{2}{w^2}(x_p - R \cos(\omega t))^2\right) \exp\left(-\frac{2}{w^2}(y_p - R \sin(\omega t))^2\right) + I_b \quad (\text{B.1})$$

A 2-dimensional Taylor series of this equation in the neighborhood of the position $(x_0, y_0) = (0, 0)$ gives:

$$\begin{aligned}
I(t) &\approx I(t)|_{x_0, y_0} + \frac{\partial}{\partial x_p} I(t) \Big|_{x_0, y_0} x_p + \frac{\partial}{\partial y_p} I(t) \Big|_{x_0, y_0} y_p + \mathcal{O}(x^2, y^2) \\
&= I_b + I_0 e^{\frac{2}{w^2} R^2 \cos^2(\omega t)} e^{\frac{2}{w^2} R^2 \sin^2(\omega t)} \\
&\quad + \left[I_0 e^{-\frac{2}{w^2} (x_p - R \cos(\omega t))^2} e^{-\frac{2}{w^2} (y_p - R \sin(\omega t))^2} \cdot \left(-\frac{4}{w^2}\right) (x_p - R \cos(\omega t)) \right]_{x_0, y_0} x_p \\
&\quad + \left[I_0 e^{-\frac{2}{w^2} (x_p - R \cos(\omega t))^2} e^{-\frac{2}{w^2} (y_p - R \sin(\omega t))^2} \cdot \left(-\frac{4}{w^2}\right) (y_p - R \sin(\omega t)) \right]_{x_0, y_0} y_p \\
&\quad + \mathcal{O}(x^2, y^2) \\
&= I_b + I_0 e^{\frac{2R^2}{w^2}} + \left[I_0 e^{\frac{2R^2}{w^2}} \cdot \frac{4R}{w^2} \cos(\omega t) x_p \right] + \left[I_0 e^{\frac{2R^2}{w^2}} \cdot \frac{4R}{w^2} \sin(\omega t) y_p \right] \\
&\quad + \mathcal{O}(x^2, y^2) \\
&= I_b + I_0 e^{\frac{2R^2}{w^2}} \left[1 + \frac{4R}{w^2} (x_p \cos(\omega t) + y_p \sin(\omega t)) \right] + \mathcal{O}(x^2, y^2)
\end{aligned}$$

The emission signal is modulated with a cos- and a sin- function.

Bibliography

- [1] R. Brown, *The Miscellaneous Botanical Works of Robert Brown* (Hardwicke, Robert, 1866).
- [2] University of Strathclyde, *Diffusion processes: proceedings of the Thomas Graham Memorial Symposium* (Gordon and Breach, London, 1971).
- [3] A. Fick, “Über Diffusion,” *Annalen der Physik* (Berlin) **170**, 59 (1855).
- [4] A. Einstein, “Zur Theorie der Brownschen Bewegung,” *Annalen der Physik* (Berlin) **324**, 371–381 (1906).
- [5] A. Einstein, “Über die von der molekularkinetischen Theorie der Wärme geforderte Bewegung von in ruhenden Flüssigkeiten suspendierten Teilchen,” *Annalen der Physik* (Berlin) **322**, 549–560 (1905).
- [6] M. von Smoluchowski, “Zur kinetischen Theorie der Brownschen Molekularbewegung und der Suspensionen,” *Annalen der Physik* **326**, 756–780 (1906).
- [7] R. Bird, W. Stewart, and E. Lightfoot, *Transport Phenomena* (Wiley, 2002).
- [8] H. Schmalzried, *Chemical kinetics in solids* (VCH, Weinheim, 1995).
- [9] B. Alberts, A. Johnson, P. Walter, J. Lewis, M. Raff, and K. Roberts, *Molecular Biology of the Cell* (Taylor & Francis, 2007).
- [10] E. L. Elson, “Fluorescence correlation spectroscopy and photobleaching recovery,” *Annu. Rev. Phys. Chem.* **36**, 379–406 (1985).
- [11] E. L. Elson and D. Madge, “Fluorescence Correlation Spectroscopy. I. Conceptual Basis and Theory,” *Biopolymers* **13**, 1–27 (1974).
- [12] E. L. Elson, “Fluorescence correlation spectroscopy: Past, present, future,” *Biophys. J.* **101**, 2855–2870 (2011).
- [13] J. Gelles, B. J. Schnapp, and M. P. Sheetz, “Tracking kinesin-driven movements with nanometre-scale precision,” *Nature* **331**, 450–453 (1988).
- [14] Q. Wang and W. Moerner, “Optimal strategy for trapping single fluorescent molecules in solution using the optical trap,” *Appl. Phys. B* **99**, 23–30 (2010).
- [15] A. E. Cohen and W. E. Moerner, “Suppressing Brownian motion of individual biomolecules on solution,” *Proc. Natl. Acad. Sci. USA* **103**, 4362–4365 (2006).

- [16] B. J. Schnapp, J. Gelles, and M. P. Sheetz, “Nanometer-scale measurements using video light microscopy,” *Cell Motil. Cytoskel.* **10**, 47–53 (1988).
- [17] B. W. Hicks and K. J. Angelides, “Tracking movements of lipids and thy1 molecules in the plasmalemma of living fibroblasts by fluorescence video microscopy with nanometer scale precision,” *Membrane Biol.* **144**, 231–244 (1995).
- [18] T. Schmidt, G. J. Schütz, W. Baumgartner, H. J. Gruber, and H. Schindler, “Imaging of single molecule diffusion,” *Proc. Natl .Acad. Sci. USA* **93**, 2926–2929 (1996).
- [19] V. Levi, Q. Ruan, K. Kis-Petikova, and E. Gratton, “Scanning FCS, a novel method for three-dimensional particle tracking.” *Biochem. Soc. Trans.* **31**, 997–1000 (2003).
- [20] M. Speidel, A. Jonáš, and E.-L. Florin, “Three-dimensional tracking of fluorescent nanoparticles with subnanometer precision by use of off-focus imaging,” *Opt. Lett.* **28**, 69–71 (2003).
- [21] A. J. Berglund and H. Mabuchi, “Feedback controller design for tracking a single fluorescent molecule,” *Appl. Phys. B* **78**, 653–659 (2004).
- [22] H. Cang, C. S. Xu, D. Montiel, and H. Yang, “Guiding a confocal microscope by single fluorescent nanoparticles,” *Opt. Lett.* **32**, 2729–2731 (2007).
- [23] J. G. Ritter, R. Veith, J.-P. Siebrasse, and U. Kubitscheck, “High-contrast single-particle tracking by selective focal plane illumination microscopy,” *Opt. Express* **16** (2008).
- [24] S. R. P. Pavani, M. A. Thompson, J. S. Biteen, S. J. Lord, N. Liu, R. J. Twieg, R. Piestun, and W. E. Moerner, “Three-dimensional, single-molecule fluorescence imaging beyond the diffraction limit by using a double-helix point spread function,” *Proc. Natl .Acad. Sci. USA* **106**, 2995–2999 (2009).
- [25] M. J. Saxton and K. Jacobson, “Single-particle tracking: applications to membrane dynamics.” *Annu. Rev. Biophys. Biomol. Struct.* **26**, 373–399 (1997).
- [26] M. B. Forstner, J. Käs, and D. Martin, “Single lipid diffusion in langmuir monolayers,” *Langmuir* **17**, 567–570 (2001).
- [27] M. Goulian and S. M. Simon, “Tracking single proteins within cells,” *Biophys. J.* **79**, 2188–2198 (2000).

-
- [28] M. Dahan, T. Laurence, F. Pinaud, D. S. Chemla, A. P. Alivisatos, M. Sauer, and S. Weiss, “Time-gated biological imaging by use of colloidal quantum dots,” *Opt. Lett.* **26**, 825–827 (2001).
- [29] L. Holtzer, T. Meckel, and T. Schmidt, “Nanometric three-dimensional tracking of individual quantum dots in cells,” *Appl. Phys. Lett.* **90**, 53902 (2007).
- [30] E. J. G. Peterman, S. Brasselet, and W. E. Moerner, “The fluorescence dynamics of single molecules of green fluorescent protein,” *J. Phys. Chem. A* **103**, 10553–10560 (1999).
- [31] G. Seisenberger, M. U. Ried, Endre, H. Buning, M. Hallek, and C. Bräuchle, “Real-time single-molecule imaging of the infection pathway of an adeno-associated virus,” *Science* **294**, 1929–1932 (2001).
- [32] L. D. Landau and F. M. Lifschitz, *Lehrbuch der theoretischen Physik - Hydrodynamik* (Akademie-Verlag Berlin, 1981).
- [33] J. Dhont, *An Introduction to Dynamics of Colloids*, Studies in Interface Science (Elsevier, Amsterdam, The Netherlands, 1996).
- [34] H. Qian, M. P. Sheetz, and E. L. Elson, “Single particle tracking. analysis of diffusion and flow in two-dimensional systems,” *Biophys. J.* **60**, 910–921 (1991).
- [35] J. Rudnick and G. Gaspari, “The shapes of random walks,” *Science* **237**, 384–389 (1987).
- [36] J. Rudnick and G. Gaspari, “The aspherity of random walks,” *J. Phys. A: Gen. Phys.* **19** (1986).
- [37] G. J. Schütz, H. Schindler, and T. Schmidt, “Single-molecule microscopy on model membranes reveals anomalous diffusion,” *Biophys. J.* **73**, 1073–1080 (1997).
- [38] A. V. Weigel, B. Simon, M. M. Tamkun, and D. Krapf, “Ergodic and nonergodic processes coexist in the plasma membrane as observed by single-molecule tracking,” *Proc. Natl .Acad. Sci. USA* **108**, 6438–6443 (2011).
- [39] M. L. Sheely, “Glycerol viscosity tables,” *Ind. Eng. Chem.* **24**, 1060–1064 (1932).
- [40] K. Kis-Petikova and E. Gratton, “Distance measurement by circular scanning of the excitation beam in the two-photon microscope,” *Microsc. Res. Tech.* **63**, 34–49 (2004).

- [41] J. Enderlein, “Positional and temporal accuracy of single molecule tracking,” *Sing. Mol.* **1**, 225–230 (2000).
- [42] J. Enderlein, “Tracking of fluorescent molecules diffusing within membranes,” *Appl. Phys. B* **71**, 773–777 (2000).
- [43] Y. Katayama, O. Burkacky, M. Meyer, C. Bräuchle, E. Gratton, and D. C. Lamb, “Real-time nanomicroscopy via three-dimensional single-particle tracking,” *Chem. Phys. Chem.* **10**, 2458–2464 (2009).
- [44] A. E. Cohen and W. E. Moerner, “Method for trapping and manipulating nanoscale objects in solution,” *Appl. Phys. Lett.* **86**, 093109 (2005).
- [45] A. E. Cohen, “Control of nanoparticles with arbitrary two-dimensional force fields,” *Phys. Rev. Lett.* **94**, 118102 (2005).
- [46] A. E. Cohen and W. E. Moerner, “Controlling brownian motion of single protein molecules and single fluorophores in aqueous buffer,” *Opt. Express* **16**, 6941–6956 (2008).
- [47] M. A. Thompson, M. D. Lew, M. Badieirostami, and W. E. Moerner, “Localizing and tracking single nanoscale emitters in three dimensions with high spatiotemporal resolution using a double-helix point spread function,” *Nano Lett.* **10**, 211–218 (2010).
- [48] D. S. Banks and C. Fradin, “Anomalous diffusion of proteins due to molecular crowding,” *Biophys. J.* **89**, 2960–2971 (2005).
- [49] M. Weiss, M. Elsner, F. Kartberg, and T. Nilsson, “Anomalous subdiffusion is a measure for cytoplasmic crowding in living cells,” *Biophys. J.* **87**, 3518–3524 (2004).
- [50] A. J. Berglund and H. Mabuchi, “Performance bounds on single-particle tracking by fluorescence modulation,” *Appl. Phys. B* **83**, 127–133 (2006).
- [51] Y. He, S. Burov, R. Metzler, and E. Barkai, “Random time-scale invariant diffusion and transport coefficients,” *Phys. Rev. Lett.* **101**, 058101 (2008).
- [52] W. Deng and E. Barkai, “Ergodic properties of fractional brownian-langevin motion,” *Phys. Rev. E* **79**, 011112 (2009).
- [53] X. Michalet, “Mean square displacement analysis of single-particle trajectories with localization error: Brownian motion in an isotropic medium,” *Phys. Rev. E* **82**, 041914 (2010).

- [54] M. J. Saxton, “Single-particle tracking: the distribution of diffusion coefficients,” *Biophys. J.* **72**, 1744–1753 (1997).
- [55] X. Michalet and A. J. Berglund, “Optimal diffusion coefficient estimation in single-particle tracking,” *Phys. Rev. E* **85**, 061916 (2012).
- [56] V. Filipe, A. Hawe, and W. Jiskoot, “Critical evaluation of nanoparticle tracking analysis (nta) by nanosight for the measurement of nanoparticles and protein aggregates,” *Pharmaceut. Res.* **27**, 796–810 (2010).
- [57] C. Finder, M. Wohlgemuth, and C. Mayer, “Analysis of particle size distribution by particle tracking,” *Part. Part. Sys. Charact.* **21**, 372–378 (2004).
- [58] R. Landsiedel, L. Ma-Hock, A. Kroll, D. Hahn, J. Schnekenburger, K. Wiench, and W. Wohlleben, “Testing metal-oxide nanomaterials for human safety,” *Adv. Mater.* **22**, 2601–2627 (2010).
- [59] M. J. Saxton, “Anomalous diffusion due to obstacles: A monte carlo study,” *Biophys. J.* **66**, 394–401 (1994).
- [60] A. Lubelski, I. M. Sokolov, and J. Klafter, “Nonergodicity mimics inhomogeneity in single particle tracking,” *Phys. Rev. Lett.* **100**, 250602 (2008).
- [61] K. L. Sebastian, “Path integral representation for fractional brownian motion,” *J. Phys. A: Gen. Phys.* **28**, 4305–4311 (1995).
- [62] S. B. Yuste, “First-passage time, survival probability and propagator on deterministic fractals,” *J. Phys. A: Gen. Phys.* **28**, 7027–7038 (1995).
- [63] S. Havlin and D. Ben-Avraham, “Diffusion in disordered media,” *Adv. Phys.* **36**, 695–789 (1987).
- [64] C. R. Haramagatti, F. H. Schacher, A. H. E. Müller, and J. Köhler, “Diblock copolymer membranes investigated by single-particle tracking,” *Phys. Chem. Chem. Phys.* **13**, 2278–2284 (2011).

List of publications

Author

- D. Ernst, S. Hain, and J. Köhler, Setup for single-particle orbit tracking: artifacts and corrections, *J. Opt. Soc. Am. A* **29**, 1277-1287, (2012)
- D. Ernst and J. Köhler, Measuring a diffusion coefficient by single-particle tracking: Statistical analysis of experimental mean squared displacement curves, *Phys. Chem. Chem. Phys.* **15**, 845-849, (2013)
- D. Ernst, M. Hellmann, J. Köhler, and M. Weiss, Fractional Brownian motion in crowded fluids, *Soft Matter* **8**, 4886-4889, (2012)
- D. Ernst, R. Hildner, C. Hippus, F. Würthner, and J. Köhler, Photoblinking dynamics in single calix[4]arene-linked perylene bisimide dimers, *Chem. Phys. Lett.* **482**, 93-98, (2009)

Co-Author

- A. Issac, R. Hildner, D. Ernst, C. Hippus, F. Würthner, and J. Köhler, Single molecule studies of calix[4]arene-linked perylene bisimide dimers: relationship between blinking, lifetime and/or spectral fluctuations, *Phys. Chem. Chem. Phys.* **14**, 10789-10798, (2012)
- A.S. Goldmann, A. Walther, L. Nebhani, R. Joso, D. Ernst, K. Loos, C. Barner-Kowollik, L. Barner, and A.H.E. Müller, Surface Modification of Poly (divinylbenzene) Microspheres via Thiol - Ene Chemistry and Alkyne - Azide Click Reactions, *Macromolecules* **42**, 3707-3714, (2009)

Danksagung

Zum Schluss möchte ich mich noch bei einigen Leuten bedanken, die auf vielfältige Weise zum Gelingen dieser Arbeit beigetragen haben.

Als Erstes möchte meinem Doktorvater Prof. Dr. Jürgen Köhler einen Dank aussprechen. Durch sein Vertrauen in meine Arbeit hat er es mir ermöglicht, einen neuen Aufbau zu entwickeln, der nach einigen Hochs und Tiefs letztendlich ausgereift war und neue Perspektiven für die weitere Forschung eröffnet. Er hat mir stets die nötige Freiheit gegeben meine Ideen umzusetzen und hat mir immer durch zahlreiche Diskussionen über meine Messergebnisse weitergeholfen, wenn ich seine Unterstützung brauchte.

Ein weiterer großer Dank geht an unseren Kooperationspartner Prof. Dr. Matthias Weiss. Von Matthias konnte ich viel über anomale Diffusionsprozesse und neue Auswertemethoden lernen. Er war immer diskussionsbereit und hat sich für meine Probleme viel Zeit genommen. Weiterhin möchte ich Dr. Marcel Hellmann danken, der mich in programmtechnischen Fragen zur Auswertung der Messdaten unterstützt hat.

Der Serviceabteilung der Firma Jäger Messtechnik GmbH möchte ich für den hervorragenden Support danken. Insbesondere ist hier Stefan Plappert zu erwähnen, der mir des öfteren die nötigen Tipps zur Softwareansteuerung des Aufbaus gab und auch fortwährend ein reges Interesse am Fortschritt meiner Arbeit zeigte.

Danke auch an Prof. Dr. Werner Köhler, der mir bei grundlegenden Fragen zu Diffusionsprozessen weiterhalf. Unsere technischen Angestellten, ohne die ein Lehrstuhl meiner Meinung nach nie richtig funktionieren kann, waren immer hilfsbereit und sorgten an vielen Stellen für eine Erleichterung der Arbeit. Stefan Schlicht war bei elektrotechnischen Fragen stets ein guter Ansprechpartner. Waltraud Joy ist mir bei chemischen Fragen bezüglich der Probenpräparation mit Rat und Tat zur Seite gestanden. Werner „Wörni“ Reichstein ist immer für einen zur Stelle und hat mir vor Allem in der Anfangsphase durch einige, teils größere, Umbauten im Labor geholfen. Weiterhin möchte ich der Mechanikwerkstatt und insbesondere Frank Neumann und Olli ein Lob aussprechen. Ohne sie wären einige Konstruktionen wohl nicht zustande gekommen. Ein großer Dank geht an die „Verwaltungszentrale“ des Lehrstuhls, das Sekretariat. Besonders erwähnen möchte ich hier Evelyn Hülsmann, die sich um sämtliche Verwaltungsangelegenheiten gekümmert hat und immer ein offenes Ohr für die „Problemchen“ der Mitarbeiter hat.

Vielen Dank auch an unsere PostDocs Richard Hildner und Abey Issac für viele interessante Diskussionen und das Korrekturlesen meiner Arbeit. Ich möchte an dieser Stelle auch „meinem“ ersten Bachelor Daniel Zalami für neue Ideen zur Weiterentwicklung des Aufbaus und für die gute Zusammenarbeit danken. Ein Dankeschön

geht auch an die Mitstreiter der Doktoranden während meiner Zeit am Lehrstuhl, Tobias Pflock und Florian Spreitler, die den Sprung in die „echte“ Welt bereits hinter sich gebracht haben. Vor allem Florian möchte ich für die große Unterstützung durch viele Diskussionen über PC-Programme, angewandte Optik und Interpretation von Messungen danken. Nicht zu vergessen sind natürlich Ralf Kunz und Paul Böhm, die mit mir die Zeit am Lehrstuhl begonnen haben und langsam auch dem Ende der Promotion entgegensehen. Auf geht's Jungs! Marc Jendry danke ich für eine coole Banz-Tagung. Besonders hervorheben möchte ich Steffen Hartmann, Matthias Gebhart, Axel Herrmann, Vanessa Weith, Laura Winterling, Lisa Krapf und Florian Schwaiger. Ein Teil davon ist zwar schon lange nicht mehr am Lehrstuhl, sie haben aber entscheidend dazu beigetragen, dass ich heute der bin, der ich bin. Ich danke euch für eine Menge schöner Erlebnisse in Bayreuth, diverse Wanderungen, exzessive Parties, lustige Kochabende, den Kaffeekentratsch und vieles mehr. Was wären die Miamiam-Besuche ohne euch gewesen. Vor allem Florian möchte ich großen Dank aussprechen. Die unzähligen Diskussionen mit ihm waren für mich nicht nur physikalisch sehr wertvoll, auch das Humorniveau wurde auf ungeahnte Ebenen gelenkt. Mann, mann, mann. Highlights waren London (Baby!) und das Pokalfinale in Dortmund (Heja BVB!). Es war eine geniale Zeit. Alle weiteren Kollegen, die hier nicht namentlich aufgeführt sind (bitte nicht böse sein), möchte ich natürlich auch für das angenehme Arbeitsklima danken. Der Lehrstuhl ist ein bunter „Haufen“ aus chaotischen und organisierten, ruhigen und aufbrausenden, engagierten und weniger engagierten, aber immer gut aufgelegten Kollegen. Ich möchte mich bei Allen für die interessantesten fachlichen und (zum Teil sehr abstrusen) nicht fachlichen Gespräche in der Kaffecke, bei diversen Grillfeiern und abendlichen Kneipen- und Biergartenbesuchen herzlichst bedanken. Das Arbeitsumfeld war durchwegs positiv und es hat sehr viel Spaß gemacht in dieser Gruppe zu arbeiten.

Auch meinen Freunden außerhalb der Universität gebührt ein Dank für die Ablenkung vom teilweise stressigen Alltag. Außerdem möchte ich auch der Familie meiner Freundin für viele schöne Stunden und Ausflüge danken.

Schließlich möchte ich mich bei meiner Familie und insbesondere bei meinen Eltern für die jahrelange und uneingeschränkte Unterstützung bedanken. Ihr habt mir immer den nötigen Rückhalt gegeben, was mir ein sorgenfreies Studium und eine anschließende Promotion ermöglichte. Ihr wart immer für da und dafür möchte einfach nur DANKE sagen. Ohne euch wäre vieles nicht möglich gewesen. Zu guter Letzt möchte ich mich bei meiner Freundin Nadine bedanken. Die letzten Jahre mit Dir waren wunderschön und hoffentlich folgen noch viele weitere. Du warst immer für mich da, hast mich bei meiner Arbeit immer unterstützt und mein Leben auf vielfältige Weise bereichert. Danke, für all die schönen Momente und dass du immer für mich da bist. ILD

Erklärung

Hiermit versichere ich an Eides statt, dass ich die vorliegende Arbeit selbstständig verfasst und keine anderen als die von mir angegebenen Quellen und Hilfsmittel benutzt habe.

Ich erkläre, dass ich keine früheren Promotionsversuche unternommen habe. Die vorgelegte Abhandlung wurde weder in gleicher noch in ähnlicher Form einer anderen Prüfungsbehörde zur Erlangung eines akademischen Grades vorgelegt.

Desweiteren erkläre ich, dass ich Hilfe von gewerblichen Promotionsberatern bzw. -vermittlern oder ähnlichen Dienstleistern weder bisher in Anspruch genommen habe noch künftig in Anspruch nehmen werde.

Bayreuth, den 27.09.2012

Dominique Ernst

Part II
Publications

PUBLICATION P1

**Setup for single-particle orbit tracking:
artifacts and corrections**

Dominique Ernst, Stefan Hain, and Jürgen Köhler

published in:

J. Opt. Soc. Am. A **29**, 1277-1287, (2012)

©2012 Optical Society of America

<http://dx.doi.org/10.1364/JOSAA.29.001277>

Setup for single-particle orbit tracking: artifacts and corrections

Dominique Ernst, Stefan Hain, and Jürgen Köhler*

Experimental Physics IV and Bayreuth Institute of Macromolecular Research (BIMF),

University of Bayreuth, 95440 Bayreuth, Germany

**Corresponding author: juergen.koehler@uni-bayreuth.de*

Received March 16, 2012; accepted March 30, 2012;
posted April 3, 2012 (Doc. ID 164958); published June 7, 2012

We report on an experimental setup for single-particle orbit tracking, which allows following fluorescent nanoparticles for more than 10 min with a temporal resolution of 4 ms and a dynamic position accuracy of better than 10 nm. On a model sample—20 nm sized fluorescent polymer beads in glycerol—we will illustrate how artifacts caused by unavoidable experimental shortcomings (might) obscure the experimental result and how misinterpretations can be prevented. © 2012 Optical Society of America

OCIS codes: 180.2520, 180.5810, 300.6280.

1. INTRODUCTION

The study of transport processes on molecular length scales is of great importance in many fields of research [1–9]. In the life sciences, reaction kinetics may depend crucially on the diffusion of the reactants [10–12], or in material engineering the flow of material through an interface is of great importance for filtering and catalysis [6,13]. Many methods for studying such processes rely on fluorescence microscopy. Initially, this was largely restricted to fluorescence recovery after photobleaching [14], which is an ensemble technique that prohibits probing of transport processes beyond the classical diffraction limit of light microscopy. Moreover, due to ensemble averaging, complex diffusion behavior might get masked in photobleaching experiments.

The situation changed drastically with the advent of single-molecule techniques. Confocal microscopy lies at the heart of fluorescence-correlation spectroscopy (FCS) and its variants [9,15]. The disadvantage of this method is that the average transition time of a particle through the detection volume of about $1 \mu\text{m}^3$ is very short. Hence, one is either limited to short observation times or one averages sequentially over many particles, making it difficult to extract information about temporal or spatial inhomogeneities. Alternatively, wide-field fluorescence microscopy has been employed to follow the diffusion of individual nano-objects. The general idea of single-particle tracking (SPT) is to determine the position of an individual particle by fitting its diffraction-limited image on a CCD camera to the known point-spread function of the microscope or, more pragmatically, by fitting it to a two-dimensional Gaussian. Associating the center of the fit with the position of the particle allows determination of the spatial position with an accuracy far beyond the classical diffraction limit of light microscopy and to follow the diffusion of this particle with high precision [1,3,16–21]. Fascinating experiments have been reported using SPT in combination with fluorescently labeled particles. Examples are the diffusion of individual lipids in membranes [4,22], the movement of proteins or quantum dots in cells [5,21,23], or the study of

biomolecular motors [24]. It even has become possible to trace the infection pathways of individual viruses [25].

While SPT allows for determining the spatial position of the tracer particle with exceptional accuracy, it provides only limited temporal resolution, mainly given by the readout time of the CCD camera. Instead of following the spatial position of a particle by recording a sequence of images in epifluorescence microscopy, Enderlein proposed a method nowadays termed single-particle orbit tracking in [26,27]. There, the excitation light is focused into the plane of the sample and rotates on a circle that encloses the particle of interest; see Fig. 1. As long as the particle is located precisely at the center of the orbit, it experiences a constant excitation intensity, despite the variation of the position of the focus. Upon any movement of the particle away from the center, this situation changes drastically and the excitation intensity, and concomitantly the intensity of the emitted fluorescence $I(t)$ from the particle, becomes modulated with the rotation frequency of the light orbit, according to

$$I(t) = I_0 \exp\left(-\frac{2}{w^2}(x_p - R \cos(\omega t))^2\right) \cdot \exp\left(-\frac{2}{w^2}(y_p - R \sin(\omega t))^2\right) + I_B. \quad (1)$$

Here I_0 corresponds to the maximum emission intensity, R to the radius of the light orbit, w to the waist of the focused excitation beam, x_p and y_p to the coordinates of the particle in the plane of the light orbit, ω to the cycle frequency of the light orbit, and I_B to the background intensity. Demodulation of the emission signal yields the coordinates of the particle

$$x_p = \frac{w^2 \int_0^T I(t) \cos(\omega t) dt}{\int_0^T I(t) dt}, \quad y_p = \frac{w^2 \int_0^T I(t) \sin(\omega t) dt}{\int_0^T I(t) dt}, \quad (2)$$

and a feedback loop can be implemented that follows the trajectory of the particle $\mathbf{r}(t) = (x_p(t), y_p(t))$ as a function of time.

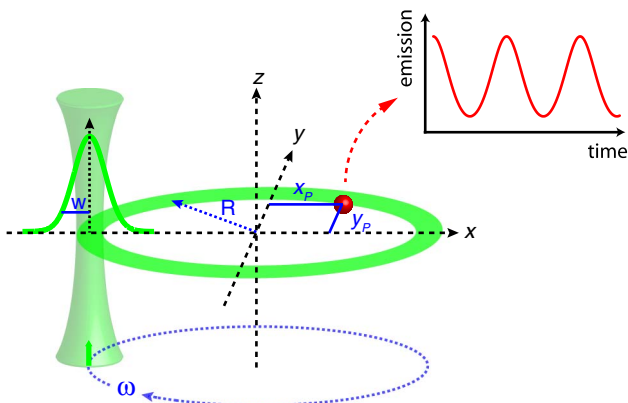


Fig. 1. (Color online) Schematic geometry (not drawn to scale) of a focused laser beam with waist w ($1/e^2$ -width) rotating at a frequency $\nu = \omega/2\pi$ in the sample plane. The red dot indicates a fluorescent particle at the position (x_p, y_p) within the orbit. The radius of the orbit is R . Inset top right, shows schematically the emission intensity of the particle as a function of time.

Meanwhile, this technique has been applied successfully by several groups to follow the position of proteins, quantum dots, or dye-labeled polymer beads in various environments [28–31]. Further progress in the field has made it possible to combine this technique with FCS [32,33], and to optically measure relative distances with nanometer precision [34]. A very ingenious experiment was developed in the Moerner group by combining this technique with a trapping setup called the anti-Brownian electrokinetic trap [35,36]. There, electrokinetic forces are used to level out the Brownian motion of a particle and keep it in the trap. The detection of the position, which is the feedback signal fed into the trap, is done with the orbit tracking technique.

However, the experimental realization of the here-presented approach bears the potential for several artifacts that might give rise to misinterpretations of the underlying diffusion process. Typically, a measured trajectory is analyzed in terms of the time-averaged mean square displacement (MSD) [37]. For two-dimensional diffusion, the MSD is commonly expressed as $\text{MSD}(\tau) = 4D\tau^\alpha$, where D is the diffusion coefficient, τ the lag time, and α the anomaly parameter [38,39]. One distinguishes between subdiffusive processes ($\alpha < 1$), normal (Brownian) diffusion ($\alpha = 1$), and superdiffusive processes ($\alpha > 1$). Yet, experimental shortcomings, rather than an underlying anomalous diffusion process, may give rise to the observation of an anomaly parameter $\alpha \neq 1$ [40].

Here we will demonstrate the performance of our orbit tracking setup for a reference sample (20 nm sized dye-labeled polymer bead in glycerol) that is known to feature normal diffusion. We will illustrate the influence of several experimental shortcomings on the resulting MSD, provide correction mechanisms, and show that we can follow the Brownian motion of the particle for more than 600 s with a temporal resolution of 4 ms and a dynamic position accuracy of 7.5 nm. Applying all corrections to remove the contributions from experimental artifacts, we find $\alpha = 1.03$ for the anomaly parameter, which is in close agreement with the expected value of $\alpha = 1$.

2. EXPERIMENTAL SECTION

A. Sample Preparation

For the characterization of the SPT setup, we purchased dye-labeled polystyrene microspheres of 20 nm in diameter

(Molecular probes, 20 mg/ml in H_2O , dye: Nile Red). These beads were further diluted in water by a factor of 10, corresponding to a bead concentration of 0.1 nM. For the preparation of static samples, this solution is mixed (1:1 vol./vol.) with a 5% polyvinyl alcohol (PVA)/water mixture, resulting in a final bead concentration of 50 pM. Subsequently, a drop of this solution (about 25 μl) was spin coated onto a quartz coverslip that was cleaned with acetone. For the preparation of mobile beads, the solution with the microspheres is dissolved in glycerol (1:50 vol./vol.), which yields a bead concentration of 2 pM. About 25 μl of this solution was sandwiched between two microscope coverslips that were cleaned with acetone. The edges of this construct were sealed with high viscosity grease (high-vacuum grease, Wacker) to prevent a flow field due to evaporation or adhesion. The samples were fixed on a piezostage that served as the sample holder in the microscope. All experiments were carried out at room temperature [$(21 \pm 0.5)^\circ\text{C}$].

B. Experimental Setup

The experimental setup consists of a laser source, a laser beam deflection unit, a home-built fluorescence microscope that can be operated either in wide-field or confocal mode, a detection part, and a calculation unit. The setup is sketched in Fig. 2(a), and in the following some of these components will be explained in more detail.

Deflection unit. The output of an Ar/Kr-Ion laser (Innova 70C Spectrum, Coherent) at 514 nm, which is linearly polarized in a direction that is vertical with respect to the optical table, is directed into two acousto-optical deflectors (AODs, DTSX-400-532; driver, DRFA10Y-B-0; amplifier, AMPA-B-30, Pegasus). The first AOD deflects the beam horizontally, and the second one deflects the beam vertically with respect to the optical table. Together with the four lenses L_1 – L_4 , which feature all the same focal length of $f_{1,2,3,4} = f = 250$ mm [see Fig. 2(b)], they constitute the deflection unit. All lenses are separated with respect to each other by twice their focal distance. The AODs are placed at one quarter of this distance, i.e., $f/2$, from L_1 and from L_3 , respectively; see Fig. 2(b). First we produce a vertically deflected beam that has a focus in the focal plane of L_1 and that propagates without divergence between L_2 and L_3 . Then the light is deflected by the second AOD in a direction perpendicular to the initial direction, and focused in the focal plane of L_3 , which is a conjugated plane of the focal plane of L_1 ; see dashed lines in Fig. 2(b). This generates a light orbit that propagates without divergence beyond L_4 . Yet the light is not propagating parallel with respect to the optical axis, but, due to L_4 , it is merged at a pivot point creating a collimated orbit of light; see Fig. 2(c). Finally, a set of telecentric lenses, L_5 and L_6 , serves for (1) projecting the pivot point into the back focal plane of an infinity-corrected objective and (2) expanding the beam to ensure full illumination of the back aperture of the objective. This results in a focused laser beam with a waist of $w = 270$ nm that rotates in the focal plane of the objective; see Figs. 2(b) and 1. The whole optical system was designed using ray transfer matrix analysis (see Appendix A.1).

In order to achieve a circular orbit, the harmonic signals that drive the AODs must have the same amplitude A , frequency ν , and a relative phase difference of $\pi/2$. In our setup, the voltage for the amplitude can be varied between 0 and 5 V,

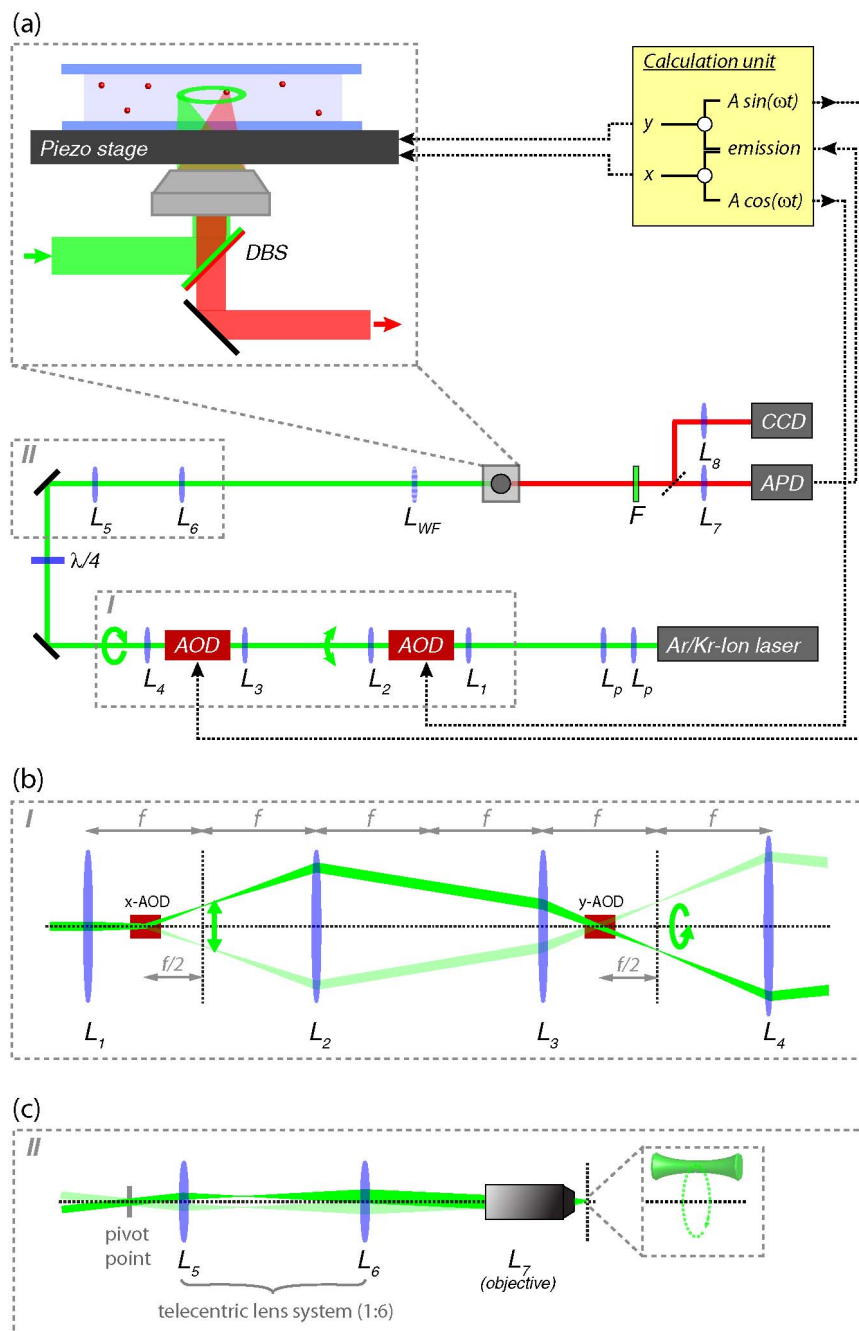


Fig. 2. (Color online) (a) Schematic representation of the optical setup. In the lower part, the light path including all optical elements is shown (L, lenses; F, filter; DBS, dichroic beam splitter; AOD, acousto-optical deflector; APD, avalanche photodiode; CCD, charge-coupled device). Inset top left, sample (blue shaded area), the microscope objective, and the piezo on an expanded scale. The excitation light is indicated in green and is reflected toward the sample by a dichroic beam splitter. Once the light orbit that is created in the sample plane hits a polymer bead (red dots), red-shifted fluorescence is emitted that passes the dichroic and travels toward the detectors. (b) Detailed view of box I of part (a), which corresponds to the deflection unit. The propagation of the laser under the most extreme deflection angles is indicated by the dark green and light green colors, respectively. The AODs are depicted as the two red boxes. The four lenses have the same focal lengths of $f = 250$ mm. The two dashed lines perpendicular to the optical axis indicate a set of conjugated planes. (c) Detailed view of box II in part (a), which represents a set of telecentric lenses. Beyond L_4 , a collimated, rotating light beam propagates under an angle with respect to the optical axis. The pivot point is defined as the point on the optical axis where the collimated beam crosses the optical axis. The set of telecentric lenses, L_5 ($f_5 = 50$ mm) and L_6 ($f_6 = 300$ mm), maps the pivot point into the back focal plane of the objective, L_7 , creating a rotating focus for the excitation light, see inset.

which corresponds to a maximum deflection angle of 20 mrad or likewise to a maximum radius R of $5 \mu\text{m}$ for the light orbit in the focal plane of the objective. The deflection frequency can be as high as 20 kHz. The parameters used for this work were as follows: $R = 190$ nm ($A = 190$ mV) and $\nu = 1$ kHz. The transmitted laser power is varied by changing the radio frequency amplitude.

Microscope. The suitably shaped laser light passes a $\lambda/4$ wave plate (Berek Polarization Compensator, New Focus) to ensure circularly polarized light and is reflected via a dichroic beam splitter (z532RDC, AHF) toward an infinity-corrected water-immersion objective (UPLSAPO, 60 \times , NA = 1.2, Olympus); see Fig. 2(a). The sample is mounted on a piezostage (Tritor 102, piezosystem Jena) that covers

a scan volume of $100 \mu\text{m} \times 100 \mu\text{m} \times 100 \mu\text{m}$. The minimum step size along each of the three axis is 3.05 nm, which is determined by the digitization accuracy of the voltages applied. The emission from the dye-loaded beads is collected by the same objective, passes the dichroic beam splitter, a dielectric filter (HQ545LP, OD = 6 @ 514 nm, AHF), and it is then focused either onto the chip of a CCD (sencam qe, PCO) or an avalanche photodiode (SPCM-AQR-14, PerkinElmer) with a sensitive area of $180 \mu\text{m}$ in diameter.

The microscope can be operated in two different modes, a wide-field mode for imaging and a confocal mode for tracking. In wide-field mode, the deflection unit is set to a neutral state where the laser beam is not deflected, and an optional lens L_{WF} with a focal length of $f_{\text{WF}} = 180 \text{ mm}$ is flipped into the optical path in front of the microscope objective. This defocuses the excitation light to an area of about $80 \mu\text{m} \times 80 \mu\text{m}$ in the sample plane, and an image of the sample can be registered with the CCD. In this mode, a particle is selected and moved with the piezostage close to the center of the orbit. Subsequently, the setup is switched to the confocal mode, i.e., the lens L_{WF} is removed, the deflection unit is switched on, generating a light orbit as described above, and the emission is collected by the APD.

C. Tracking of a Particle, Data Acquisition, Trajectory Analysis

The home-written tracking software consists of a feedback algorithm that calculates the x and y positions of the particle with respect to the center of the orbit at every time step Δt . The time resolution of the experiment is determined by the frequency ν of the rotating laser focus and the number of periods (cycles) P ; i.e., $\Delta t = P/\nu$ for one time step. During that interval, the fluorescence signal from the APD is acquired at a sampling rate of $\delta t^{-1} = 500 \text{ kHz}$, which is the highest rate possible to run our tracking software without runtime errors. The ratio between $\Delta t/\delta t = N_s$ defines the number of data points sampled for one position calculation. The position of the particle (x_p, y_p) is calculated according to

$$x_p = \frac{w^2 \sum_{n=1}^{N_s} S_n \cos(\omega n \delta t)}{2R \sum_{n=1}^{N_s} S_n}, y_p = \frac{w^2 \sum_{n=1}^{N_s} S_n \sin(\omega n \delta t)}{2R \sum_{n=1}^{N_s} S_n}. \quad (3)$$

Here S_n denotes the number of photons collected during the n th sampling interval, and $\omega = 2\pi\nu$. Next, the coordinates of the particles are converted into suitable voltages and fed to the piezostage with the reversed sign moving the particle back to the center of the light orbit. This feedback loop is repeated many times, and from the movement of the piezo, the corresponding movement of the particle can be reconstructed providing its trajectory in the x, y plane, i.e., perpendicular to the optical axis. With this method, the determination of one pair of coordinates $x_p(\Delta t), y_p(\Delta t)$ requires at least one full period of rotation of the light orbit.

In order to follow the diffusion of the particle also along the direction of the optical axis (z axis), we moved the piezo periodically up and down along this direction. This movement corresponds to N_z steps of size s (s is a multiple of the minimum step width of the piezo) in either direction. The temporal resolution of one z cycle is $\Delta t_z = N_z \Delta t$, and hence a factor of N_z slower than the temporal resolution of the x, y feedback loop. Therefore, the fluorescence signal of the bead

as a function of the z position is used only to keep the particle in the plane of the light orbit rather than to register the three-dimensional diffusion. All calculations are performed by a programmable I/O box (AdWin Gold II, Jäger Messtechnik). This box is a versatile piece of equipment that acquires the APD signal, controls the voltages for the three piezoaxes, and provides the voltages $U_x(n\delta t) = A \cos(\omega n \delta t)$ and $U_y(n\delta t) = A \sin(\omega n \delta t)$ that are applied to the AODs for the x and y deflection of the light beam. Moreover, it can be programmed to act as a lock-in amplifier to determine the position of the particle; see Eq. (3). Employing this device avoids hardware conflicts with computer interfaces, and it ensures a perfect temporal synchronization between the generation of the discrete positions within the orbit and the acquisition of the signal.

In order to analyze individual trajectories $\mathbf{r}(t) = (x_p(t), y_p(t))$ consisting of N positions, we determine the time-averaged mean squared displacement (MSD) [3,37] after a lag time $\tau = k\Delta t$ according to

$$\text{MSD}(\tau) = \langle \Delta \mathbf{r}(k\Delta t)^2 \rangle_T = \frac{1}{N-k} \sum_{i=1}^{N-k} [r(i\Delta t) - r((i+k)\Delta t)]^2. \quad (4)$$

Here, the brackets $\langle \cdot \rangle_T$ symbolize time averaging.

3. CHARACTERIZATION OF THE SETUP

Generally, the more photons that can be collected, the better the achievable position accuracy. One way to achieve this is by increasing the excitation intensity, which, however, has to be limited to a range such that forces exerted on the particle by the optical field can still be neglected; see Appendices A.2 and A.3. Alternatively, this can be accomplished by increasing the time interval during which the photons are collected. As a consequence of this, there is always an unavoidable conflict between temporal and spatial resolution. This becomes even more evident when diffusion processes are studied, because the movement of the particle during the acquisition time tends to smear out the spatial position. Accordingly, the experimentalist has the choice between poor localization accuracy due to poor photon statistics or due to averaging the position of the particle. This illustrates that the outcome of a tracking experiment depends critically on the number of emitted photons per unit time and the mobility of the emitter.

A. Choice of Experimental Parameters

Yet, besides these general restrictions the tracking performance, i.e., the achievable temporal and spatial resolution, is also determined by several experimental parameters such as the frequency at which the light orbit rotates, the radius of the orbit, and the parameters for the z axis tracking. The temporal resolution is determined by the rotation frequency ν and the number of rotation periods P that are accumulated for one calculation step of the spatial position. In our setup, this limits the temporal resolution principally to 0.05 ms ($\nu = 20 \text{ kHz}$, $P = 1$). However, the time-limiting process in our current setup is the oscillation of the piezo when it approaches a preset position and which takes about 2 ms. Therefore, we have chosen an orbit frequency of 1 kHz and define the first two periods as waiting time without any data acquisition. Hence, the best time resolution that can be achieved with our components corresponds to 3 ms. For the experiments shown here, we used $P = 4$; i.e., the spatial position of the

emitter is determined every 4 ms. Another parameter that has to be chosen carefully is the radius of the orbit. According to [41], the optimum radius depends only on the beam waist w and is given by $R = w/2^{1/2}$. For these conditions, a particle at the center of the orbit experiences the steepest gradient of the excitation intensity, translating movements of the particle into the largest possible changes of the emission intensity. Given the diffraction-limited beam waist of $w = 270$ nm, we have set $R = 190$ nm.

B. Experimental Artifacts

Nevertheless, even when carefully setting the experimental parameters, it cannot be avoided that the calculation of the spatial position of the particles is influenced by experimental imperfections, leading to misinterpretations of the data. In combination with simulation, we identified several perturbations that affect the measured spatial position of the particle: systematic errors of the tracking algorithm [41], mechanical misalignments, the limited signal-to-noise ratio [40], and averaging effects during data acquisition [5,7]. In the following we will address these issues one by one and discuss how to avoid or minimize their influence on the position accuracy and concomitantly on the MSD.

Systematic error in the tracking algorithm. A major problem in calculating the absolute position of a particle from the demodulation of the emission intensity is the neglect of higher harmonics in the signal [41]. This approximation is justified as long as the particle is close to the center of the light orbit and movements are small with respect to R . The more the particle moves out of the center of the light orbit, the more the signal is affected also by higher harmonics; see Fig. 3(a). This leads to a putative shift of the spatial coordinates toward smaller values.

In order to address this issue, we simulated the signal [see Eq. (1)] for an immobile particle as a function of the distance from the center of the light orbit and determined its position with the algorithm [Fig. 3(b) red line]. Indeed, the calculated positions level off at larger distance from the center. Though in the simulations the “real” position of these particles is known as well [Fig. 3(b) blue line], and the error introduced by this effect corresponds to the difference between the two full lines shown in Fig. 3(b). From this difference, we determined a correction function that is implemented as a fourth-order polynomial into the algorithm, providing a real-time correction for the calculation of the particle position during data acquisition. Subsequently, we did an experiment without the feedback algorithm on immobile particles that could be placed at will with respect to the center of the light orbit. The measured positions of the particle without correction are shown in Fig. 3(b) by the red squares and are in good agreement with the simulated curve. Repeating the experiment with the real-time correction yields the blue circles in Fig. 3(b), which are, as well, in very good agreement with the reference line. It is worth noting that the correction function was calculated from simulated data, i.e., further experimental shortcomings as will be discussed below, and which affect the calculated positions of the particle as well, do not play a role for this correction step.

(Mis)alignment of the piezostage. In order not to lose the particle in the z direction, the piezo is wobbled along the z axis, as detailed above. Ideally the direction of this movement

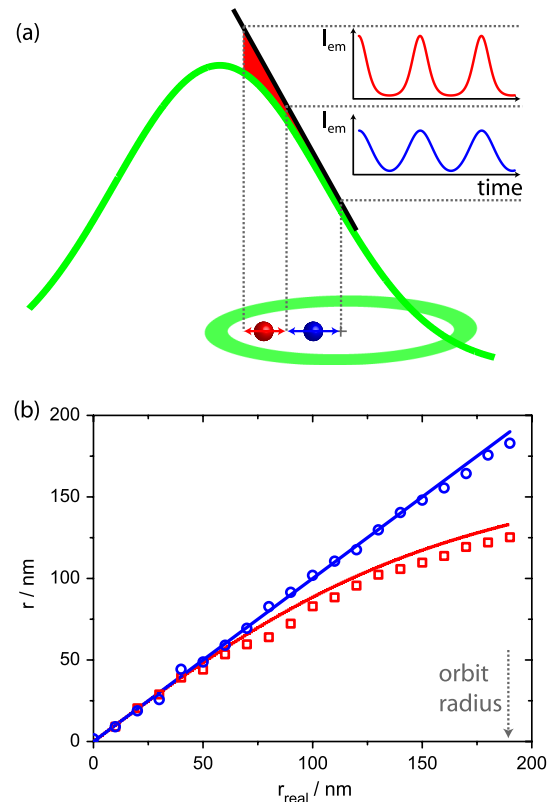


Fig. 3. (Color online) (a) Excitation intensity experienced by fluorescent particles (blue, red dots) as a function of their position with respect to the light orbit. The laser intensity is represented by a Gaussian profile (thin green curve) the light orbit by the ellipse (thick green line). A particle that resides close to the center of the light orbit (blue dot) experiences linear changes of the excitation intensity (black line) upon small movements. This yields a harmonic modulation of the emission intensity of the particle (blue profile, top right). Particles that reside close to the rim of the light orbit (red dot) experience strong deviations from a linear variation of the excitation intensity upon small movements, as is indicated by the red-shaded area. This introduces higher harmonics into the temporal modulation of the emission intensity (red profile, top right). (b) Simulation (red line) of the position of the particle determined by the tracking algorithm, r , as a function of its real position r_{real} with respect to the center of the light orbit. The radius of the light orbit is $R = 190$ nm and is indicated by the arrow. The difference between the red line and the blue line, which corresponds to the angle bisector, provides the correction function for the position of the particle. In two consecutive experiments, an immobilized particle was moved with the piezo in steps of 10 nm from the center to the rim of the light orbit. In the first experiment, its position was determined without the correction (red squares), whereas for the second experiment, the correction was applied (blue circles).

coincides perfectly with the optical axis. In a real situation, there is always a slight mismatch between these two axes, which leads to a periodic movement of the particle in the plane perpendicular to the optical axis; see Fig. 4(a). This oscillation can be misinterpreted as a lateral movement of the particle. In order to visualize this artifact more clearly, we performed an experiment where we tilted the piezo on purpose by more than 2° from the direction of the optical axis. The parameters for the z tracking were set to a step size of $s = 20$ (≈ 60 nm), and the number of steps (in one direction) was $N_z = 4$. The resulting MSD from this experiment is shown in Fig. 4(b) by the black squares. As expected, it features a modulation with a frequency proportional to $2N_z$. Because the frequency of this modulation is known, phase sensitive

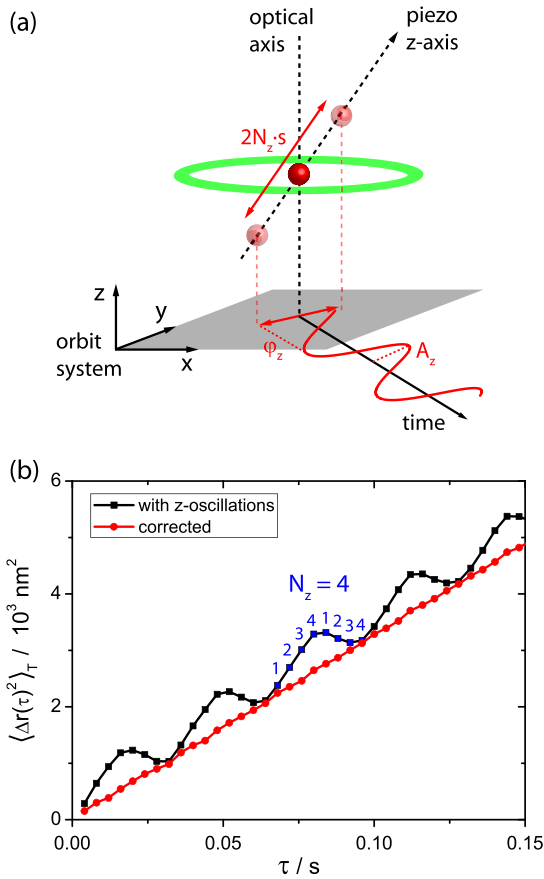


Fig. 4. (Color online) (a) Illustration of the mismatch between the optical axis and the z axis movement of the piezo. The green ellipse represents the light orbit. The piezo is wobbling over a distance $2N_z s$ along the piezo z axis. For a fluorescent bead (red dot) in the light orbit, this appears as if the particle oscillates in the plane perpendicular to the optical axis (red harmonic signal). (b) MSD of a trajectory of a 20 nm sized bead in glycerol. For this experiment, the piezostage was tilted on purpose by more than 2° with respect to the optical axis. The raw data (black squares) stem from a trajectory that has been followed for 5 min with a time resolution of $\Delta t = 4$ ms. The number of steps for the movement of the piezo along the z axis was $N_z = 4$, with a step size of $s = 20$ (≈ 60 nm). The modulation of the MSD with a period of $2N_z$ is clearly revealed and highlighted by the blue data points. The MSD calculated from the corrected coordinates (see text) is given by the red dots. For both MSDs, the solid lines serve as a guide for the eye.

lock-in analysis of the measured time traces along the x and y directions allow extraction of the amplitude and the relative phase of this superimposed oscillation. Once these data are known, the oscillation is subtracted from the experimental data, as shown for the example in Fig. 4(b), where the effect was purposely exaggerated. In a real experimental situation, the tilting angle of the piezo with respect to the optical axis was minimized to less than 1° and residual oscillations of the lateral position of the particle were corrected as described above.

Finite signal-to-noise ratio. There is no experiment without noise. In SPT experiments, the limited signal-to-noise ratio of the emission affects the accuracy of the calculated position of the particle, which leads to an additive constant in the MSD:

$$\langle \Delta r(\tau)^2 \rangle_T = 4D\tau + 2\sigma^2. \quad (5)$$

Displaying the MSD on a double logarithmic scale yields deviations from a linear relationship at short times that might be misinterpreted as subdiffusive processes. This issue is discussed in detail in [40].

In Fig. 5 we show the MSD from a tracking experiment on a single polymer bead of 20 nm size in glycerol as a function of the number of detected photons from the emitter. The signal from the bead was varied by 1 order of magnitude by changing the excitation rate. The experiment was performed on exactly one single bead for all excitation intensities to exclude variations of its diffusion behavior that depend on its actual size or shape. Displaying the MSD on a linear scale yields a linear time dependence for a Brownian motion. As expected, the lines are offset with respect to each other, reflecting the different noise levels of the experiments [Fig. 5(a)]. However, displaying the MSD on a double logarithmic scale [Fig. 5(b)] yields at short times deviations from the normal diffusion behavior mimicking a deviation from Brownian motion. Correction of this artifact is trivial. From the linear relation, the offset $2\sigma^2$ can be determined and subtracted. More interesting is the fact that the determination of the offset gives access to the dynamical position accuracy σ , which varied between 11 nm for the experiment with the highest count rate and 32 nm for the experiment with the lowest signal.

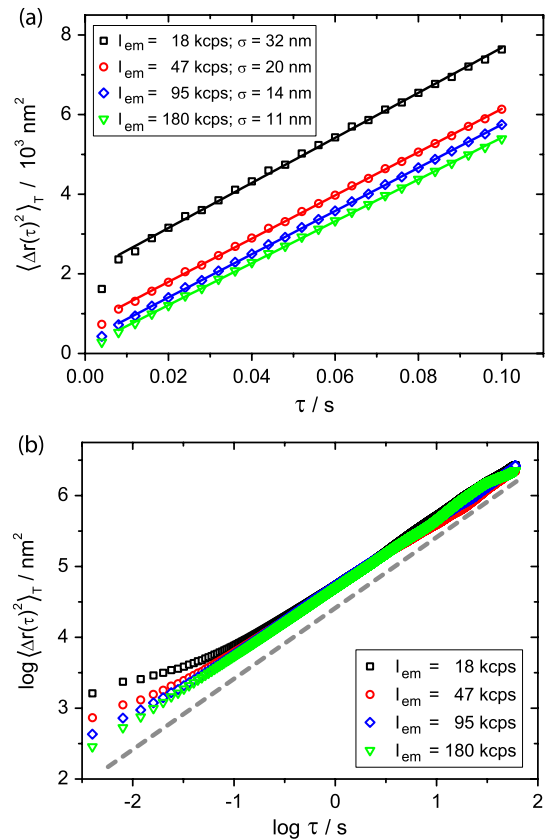


Fig. 5. (Color online) MSD of 20 nm sized tracers in glycerol as a function of the emission intensity of the particle, which increases from top to bottom by about 1 order of magnitude. The variation in emission intensity was controlled by the excitation intensity. (a) Plot of the data (symbols) on linear scales and linear fits (lines). (b) Plot of the same data on double logarithmic scales. For comparison, the dashed gray line represents the MSD that would have been obtained for $\sigma = 0$. In both plots, the first data point has been skipped due to residual influence of the oscillation of the piezo.

Position averaging. A more serious problem is that the particle is moving during the acquisition time Δt . Hence, rather than an actual position of the particle one determines the average position of the particle during the data acquisition interval; see Fig. 6(a). This effect leads to an underestimation of the MSD and shams a (nonexisting) superdiffusive motion of the particle at short time scales; see Fig. 6(b). This problem has been treated in detail in [5,7] and leads to a subtractive term in the MSD, i.e., $\langle \Delta r(\tau)^2 \rangle_T = 4D(\tau - \Delta t/3)$, which can be experimentally verified; see the full symbols in Fig. 6(b). This artifact can be corrected by (1) determination of the diffusion coefficient from the data points of the linear plot (data not shown) and then (2) adding $4/3D\Delta t$ to the data points.

C. Stability: Drift and Flow

Next to artifacts that are introduced by experimental shortcomings, the long-term stability of the setup plays an important role for tracking experiments. Drifts of the components with respect to each other will be superimposed on the movements of the particles and provide another source for misinterpretation. In order to investigate the mechanical stability of the setup, we immobilized a fluorescent bead in PVA and monitored its position without the feedback algorithm for 600 s, corresponding to 150,000 position determinations. From that we determined the initial (end) position by averaging the first

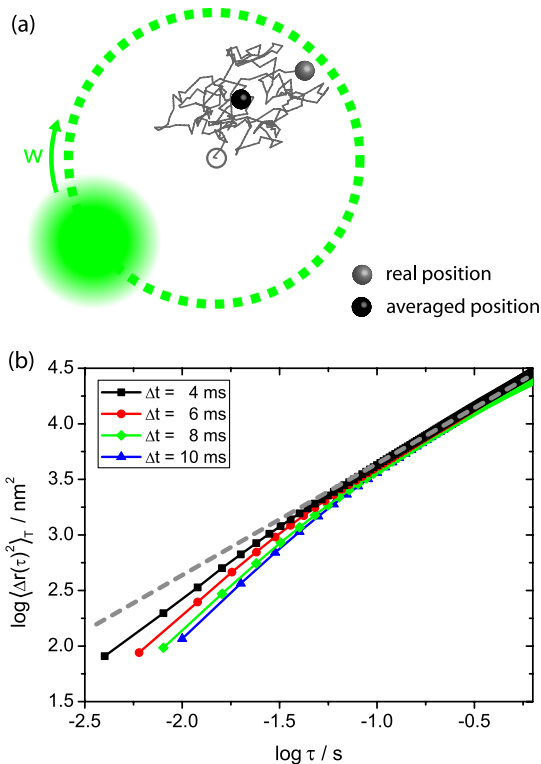


Fig. 6. (Color online) (a) Schematic representation of position averaging during the acquisition time Δt . The green area corresponds to the focal spot that rotates in the plane of the sample (green dotted line). The gray line depicts the movement of the particle during the acquisition time Δt . It starts at the center of the orbit indicated by the open circle and ends at the position indicated by the gray dot. The full black dot is the position that is measured and corresponds to the averaged position of the particle during Δt . (b) Double logarithmic plot of the MSD (symbols) of a 20 nm sized particle in glycerol as a function of the duration of the acquisition time. For comparison, the MSD that corresponds to the extrapolation toward $\Delta t = 0$ is shown by the dashed gray line. All other lines serve as a guide for the eye.

(last) 4000 data points. This experiment was repeated on three different beads, and we found an average drift of the setup of $\delta v_x = 0.06$ nm/s and $\delta v_y = 0.04$ nm/s for the x and y directions, respectively.

Another important issue concerns the flow of the medium in the sample chamber. For polymer beads in glycerol, we expect a Brownian motion with the characteristic of a zero mean displacement; i.e., $\langle \Delta x \rangle = \langle \Delta y \rangle = 0$. Any deviation from zero can be identified as flow. In order to quantify this effect, we interpreted a long trajectory of about 150,000 data points as a sequence of 150 short trajectories of 1000 data points each. For each of the short sequences, we determined the displacement of the particle along the x and y directions between the start and the end positions. A typical example with the resulting displacement vector is shown in Fig. 7(a). An ensemble of 1050 displacement vectors taken consecutively from trajectories of seven different particles within the same sample is shown in Fig. 7(b). The starting position of the displacement vectors is normalized to the origin. The spherical shape of the envelope of these vectors is already an indication that flow is very weak. A quantitative measure is obtained from the histograms [Figs. 7(c), 7(d)] which show the distributions of the displacements along the x and y directions, respectively. Gaussian fits of the histograms yield slight offsets from zero, -47 nm (x offset) and -38 nm (y offset), which correspond to a flow of $v_x = 12$ nm/s and $v_y = 10$ nm/s. However, typically the 20 nm beads move, on average, about 250 nm during 1 s, exceeding the movement that can be associated with flow by a factor of 20. Therefore, we neglect influences of drift and flow in the following.

D. Hierarchy of Corrections

In an experimental situation, the above-mentioned corrections are applied according to the following hierarchy. (1) The experimentally determined coordinates of the particle are corrected for the systematic error in the tracking algorithm due to neglect of higher harmonics; see Fig. 3. (2) The supposed oscillation in x , y coordinates due to the misalignment of the piezostage with respect to the optical axis is removed from the data; see Fig. 4. The resulting corrected coordinates are used to calculate the MSD. As discussed above, the MSD is still affected by two systematic errors and can be expressed as

$$\langle \Delta r(\tau)^2 \rangle_T = 4D(\tau - \Delta t/3) + 2\sigma^2. \quad (6)$$

(3) The linear slope of the MSD provides the diffusion coefficient D , and in order to compensate for the error in position averaging [see Fig. 6], the term $4/3D\Delta t$ is added to the MSD. However, for underlying anomalous diffusion processes, the MSD follows a power law, i.e., $\text{MSD}(\tau) \sim \tau^\alpha$ with $\alpha \neq 1$, and the correction is slightly more tedious. Then the diffusion coefficient is obtained either from a fit to the power law or from an MSD that is approximated as a linear function within distinct time intervals. (4) Finally, the offset $2\sigma^2$ that results from the finite signal-to-noise ratio is determined and subtracted, providing the dynamic position accuracy. Step (1) is done in real time during data acquisition, whereas all other steps are performed later in computer memory. We discarded doing the corrections concerning step (2) in real time, because this would be a time-limiting factor that impacts on the temporal resolution of the experiment. It is worth to note

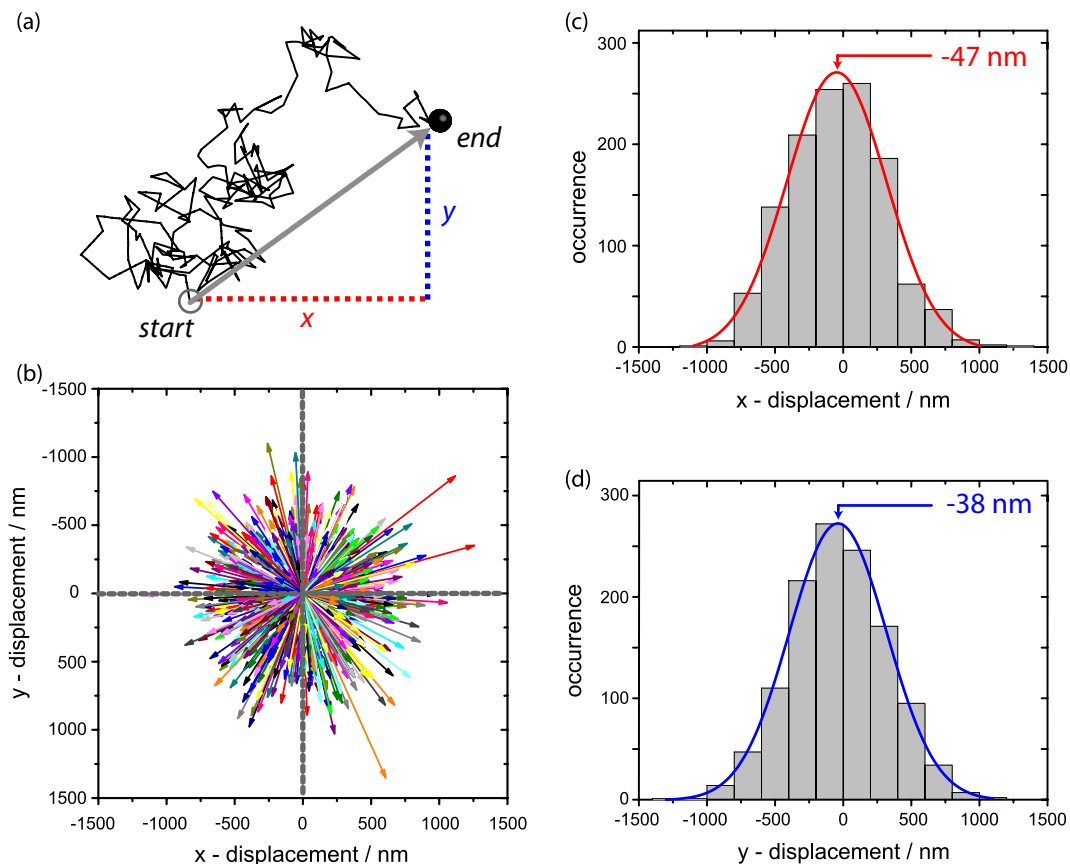


Fig. 7. (Color online) Measuring the flow in the sample chamber. (a) Sequence of 1000 data points (4 s) taken from a long trajectory of 150,000 data points. The gray arrow corresponds to the displacement vector of the particle during the 4 s. (b) Scatterplot of 1050 displacement vectors from seven independent trajectories. The vectors have been shifted with their starting point to a common origin. (c) Histogram of the x component of the displacement vectors. The full line corresponds to a Gaussian fit centered at a mean of -47 nm. (d) Histogram of the y component of the displacement vectors. The full line corresponds to a Gaussian fit centered at a mean of -38 nm.

that the corrections (3) and (4) are significant only at short time scales or small movements, respectively. As soon as $\tau \gg \Delta t$ or $\text{MSD} \gg \sigma^2$ is fulfilled, the influence of these corrections on the results is negligible.

4. EXAMPLE

As an example, we present an experiment where we studied the diffusion of a 20 nm sized tracer particle in pure glycerol. This sample was chosen, because glycerol does not form network structures and normal, Brownian diffusion can be expected [42], i.e., a linear dependence of the MSD of the traces as a function of the lag time. Or more formally $\text{MSD}(\tau) \sim \tau^\alpha$, with $\alpha = 1$.

We recorded trajectories with 150,000 positions, corresponding to an experimental time of 10 min. In order to compensate for the decrease of the emission signal in the course of time, for example due to bleaching effects, the excitation power was varied between 130 nW–1.5 μ W, which ensured a rather constant emission of about 1.5×10^5 cps (counts per second) during the experiment. In most of the experiments, the mean excitation power was about $P_{\text{ex}} = 560$ nW, which corresponds to an excitation intensity of $I_{\text{ex}} = 250$ W/cm² in the focus of the microscope objective. The rotation frequency of the light orbit was set to $\nu = 1$ kHz with $P = 4$ periods of rotation, resulting in a bin time of $\Delta t = 4$ ms. The parameters for the z tracking were $N_z = 10$ and $s = 5$

(≈ 15 nm). We recorded trajectories from seven different particles in order to compensate for the (slight) dispersion in the diameters of the beads and for possible variations of their shapes.

In Fig. 8 the first 50 data points of the “ensemble” average of time-averaged MSDs are shown for different stages of the corrections. The MSD that has been calculated after carrying out corrections (1) and (2) of the coordinates is shown by the black color code (squares), the one that results after step (3) is given by the blue color code (circles), and finally the fully corrected MSD [after step (4)], is indicated by the red color code (triangles). In order to show the differences between the three MSDs more clearly, some data points are shown on an expanded scale in the top right inset of Fig. 8(a). The solid lines in Fig. 8(a) refer to linear fits, which differ only by their offset; see inset, top left. From the slope we obtain the diffusion coefficient $D_{\text{exp}} = 0.0178$ $\mu\text{m}^2/\text{s}$ that can be compared with the prediction according to the Stokes–Einstein relation $D_{\text{theo}} = k_B T / 6\pi\eta a$. Here a refers to the radius of the particle, η to the viscosity of the medium, T to the temperature, and k_B to the Boltzmann constant. Using $T = 294$ K, $\eta = 1.2$ Pa \cdot s [42], and $a = 10$ nm, we obtain $D_{\text{theo}} = 0.0179$ $\mu\text{m}^2/\text{s}$ in nearly perfect agreement with the experimental value. The differences in the offsets of the three MSD curves become clear in the top left inset of Fig. 8(a), which shows the extrapolation of the three fitted curves

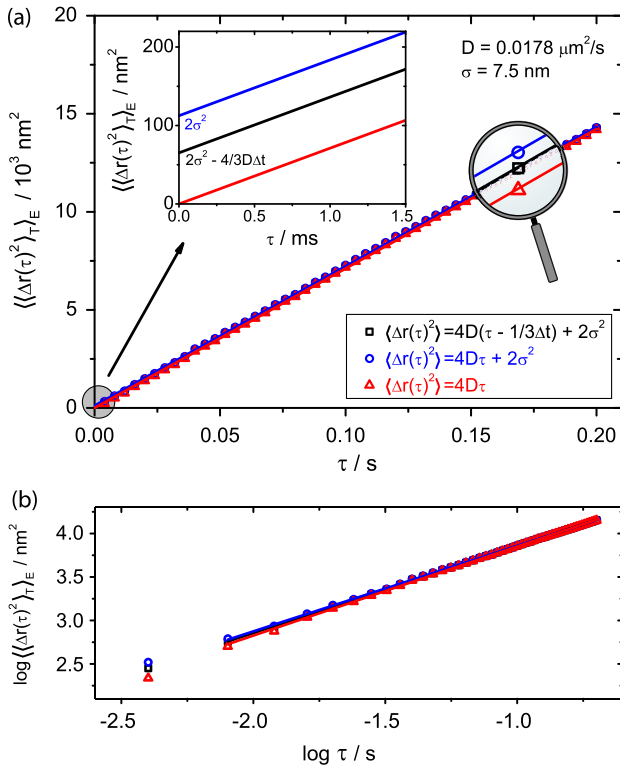


Fig. 8. (Color online) Ensemble average of time-averaged MSDs from seven trajectories taken from different 20 nm sized beads in glycerol at different stages of the correction. (a) Linear plot: raw data (black squares), data corrected for position averaging (blue circles), and fully corrected data (red triangles). All lines correspond to linear fits. The top right inset shows the same data at a scale that has been expanded by a factor of 100. The top left inset shows the extrapolation of the fits toward $\tau = 0$ and the respective intercepts with the MSD axis. For this example, we obtain D and σ as given in the figure. (b) Same data on double logarithmic axis. The lines are linear fits to the data with slopes of 1.00 (black squares), 0.98 (blue circles), and 1.03 (red triangles). For more details, see the text.

toward $\tau = 0$. Once the diffusion coefficient is obtained, the other two corrections, i.e., adding $4/3D\Delta t$ and subtracting the remaining offset are trivial. From the last correction, we obtain $2\sigma^2$, which provides the dynamic position accuracy of $\sigma = 7.5 \text{ nm}$ for the example shown here.

In order to enhance the visibility of any deviation from $\alpha = 1$, Fig. 8(b) displays the same data on a double logarithmic scale. The lines are linear fits with slopes $\alpha_{12} = 1.00$ (black squares), $\alpha_3 = 0.98$ (blue circles), and $\alpha_4 = 1.03$ (red triangles), which all agree very well with both the data and the expectation. Here the indices refer to the level of corrections. However, it should be noted that only the fully corrected MSD obeys $\log \text{MSD}(\tau) = \alpha \log \tau + \log 4D$, which allows extracting the scaling exponent α by linear fitting. The other two exponents (α_{12} and α_3) should be regarded only as apparent scaling parameters α^* following the notation in [40]. Nevertheless, for any level of correction, the deviations of these parameters from $\alpha = 1$ are within the experimental accuracy, testifying that the expected Brownian motion is revealed, and that the experiments were performed in a regime where corrections (3) and (4) were of minor importance.

An alternative method to analyze single-particle trajectories with respect to the diffusion behavior, relies on the cumulative distribution function [CDF($r^2 \tau$)] of the squared displace-

ments r^2 for a certain lag time τ [43,44]. The analysis of our data according to this protocol is given in detail in Appendix A.4 and reproduces Brownian motion.

5. CONCLUSION

We have described the details of an experimental setup that exploits orbit tracking to follow the movement of an individual fluorescent particle with a position accuracy far beyond the classical diffraction limit. The figures of merit depend on the dynamics of the system and on the number of detected photons per unit time. Typical values for diffusion in viscous media that we achieved are a position accuracy better than 10 nm, a temporal resolution of 4 ms, and a total observation time of more than 600 s. This allowed recording of trajectories of the particle movement consisting of more than 10^5 data points providing excellent statistics for data evaluation. However, the experimental realization of orbit tracking was hindered by several shortcomings leading to artifacts in the data that might misleadingly be interpreted as an underlying anomalous diffusion process. We have presented a detailed characterization of these problems, elucidated the origin of several artifacts, and showed how to correct the data accordingly. The operation of the setup and the influence of the artifacts on the data were illustrated for a model system from which it is known that it features normal diffusion. We have demonstrated that the normal diffusion can be revealed on all experimentally accessible time scales, if the corrections of the artifacts are properly taken into account. The agreement between the measured and calculated diffusion coefficient is better than 1%.

APPENDIX A

1. Beam Path Calculation

The optical system for the excitation light was designed using ray transfer matrix analysis [45], which has been proven to be a powerful tool to trace a Gaussian beam through a complex optical setup. The beam is represented by a two-component vector $\mathbf{b} = (b, \varphi)$ where b corresponds to the distance of the beam from the optical axis and φ to the angle between the propagation direction of the beam and the optical axis. Each optical element can be represented by a transfer matrix that relates a given input vector \mathbf{b}_{in} to a distinct output vector \mathbf{b}_{out} . The optical path of a series of optical elements is then simply calculated by multiplying the respective transfer matrices. For the setup described in the text, we find for the transfer matrix of the full system

$$\begin{pmatrix} b_{\text{out}} \\ \varphi_{\text{out}} \end{pmatrix} = \begin{pmatrix} -\frac{f_7 f_5}{f_6 f} & -\frac{1}{2} \frac{f_7 f_5}{f_6} \\ 2 \frac{f_6}{f_7 f_5} & 0 \end{pmatrix} \cdot \begin{pmatrix} b_{\text{in}} \\ \varphi_{\text{in}} \end{pmatrix}, \quad (\text{A1})$$

where the microscope objective has been approximated as a single lens with $f_7 = 3 \text{ mm}$. All other focal distances are given in the text. This simple set of linear equations allows to calculate the radius of the light orbit ($R_{\text{out}} = b_{\text{out}}$) and its orientation with respect to the optical axis (φ_{out}) as a function of the incoming beam radius b_{in} and deflection angle φ_{in} . Here we used $\mathbf{b}_{\text{in}} = (0, 0.76 \text{ mrad})$ starting at the center of the first AOD and obtain $\mathbf{b}_{\text{in}} = (190 \text{ nm}, 0)$, i.e., a focused laser beam that rotates on a cylinder having the optical axis as symmetry axis; see Fig. 9.

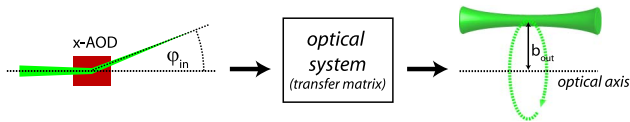


Fig. 9. (Color online) Schematic representation of the beam path calculation starting at the first AOD (x AOD).

2. Radiation Pressure

The force exerted on a fluorescent particle due to the incident photons is given by $F_p = P_{\text{ex}}/c$, where P_{ex} denotes the excitation power and c the speed of light. For $P_{\text{ex}} \approx 1 \mu\text{W}$, which is typical for our experiments, and the extreme assumption that all photons would be absorbed, this yields a force of about 10^{-15} N. This figure has to be compared with the force exerted on the particle (radius a) due to friction in a medium (viscosity η), which is given by $F_{\text{Stokes}} = 6\pi\eta a$. Even for a low-viscosity medium like water ($\eta = 10^{-3} \text{ Pa} \cdot \text{s}$), this yields for a particle with a radius of 10 nm a force of $F_{\text{Stokes}} \approx 10^{-10}$ N, exceeding the force induced by the radiation pressure by several orders of magnitude.

3. Optical Trapping

The potential of an optical trap is given by

$$U_{\text{trap}} = \frac{4P_{\text{ex}}n_m^4 a^3}{w^2 c} \left(\frac{m^2 - 1}{m^2 + 2} \right), \quad (\text{A2})$$

where P_{ex} refers to the excitation power, n_m to the index of refraction of the medium, a to the radius of the particle, w to the beam waist, and $m = n_p/n_m$ to the ratio of the indices of refraction of the particle and the medium, respectively [46, 47]. Using the numerical values from our experiments, i.e., $P_{\text{ex}} = 1 \mu\text{W}$, $n_m = 1.33$, $n_p = 1.65$, $a = 10$ nm, and $w = 270$ nm, we obtain a trapping potential of about $U_{\text{trap}} \approx 10^{-26}$ J, which is orders of magnitude smaller than the thermal energy at room temperature, which amounts to $U_{\text{therm}} = k_B T \approx 10^{-21}$ J.

4. Cumulative Distribution Function

The empirical CDF (r^2, τ) for a certain lag time τ (data not shown) is determined by counting the number of squared displacements smaller or equal to r^2 . For normal diffusion a single-exponential curve is expected, while in systems with anomalous diffusion deviations from this function are taken into account by a double-exponential curve given as

$$\text{CDF}(r^2, \tau) = 1 - \left(\beta \exp\left(-\frac{r^2}{r_1^2}\right) + (1 - \beta) \exp\left(-\frac{r^2}{r_2^2}\right) \right). \quad (\text{A3})$$

Here, the r_i^2 are fit parameters that are related to the diffusion coefficients, commonly interpreted as a fast and a slow component, weighted with a parameter β . For Brownian motion, this reduces to the single-exponential; i.e., $\beta = 1$ [43, 44].

From our data we calculated the CDFs for lag times $\tau = (2-50)\Delta t$, and we determined β accordingly. Figure 10 displays the CDF for $\tau = 40$ ms as a typical example, which shows a nearly perfect agreement between the data and the fit. Averaging over all lag times $\tau = (2-50)\Delta t$ and seven trajectories yields $\beta = 0.96$. It should be noted that the CDF analysis does not include the corrections of the position averaging and the finite signal-to-noise ratio [correction steps

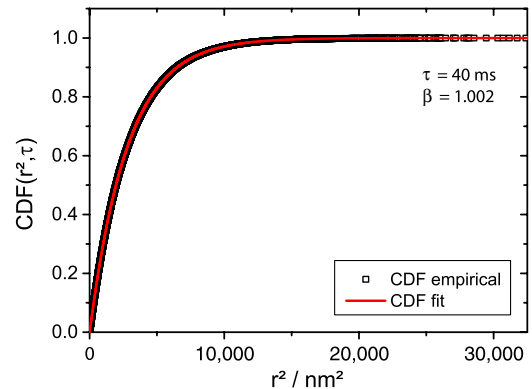


Fig. 10. (Color online) Example of empirical CDF as a function of the squared displacements at a lag time of $\tau = 40$ ms is shown by the black squares. The fit (red line) was performed according to Eq. (A3).

(3) and (4)]. This analyzing method gives only limited information about the degree of subdiffusion, but is suited to distinguish normal from anomalous diffusion.

ACKNOWLEDGMENTS

We thank Werner Köhler, Florian Schwaiger, and Florian Spreitler for fruitful discussions and gratefully acknowledge financial support from the German Science Foundation (DFG) within the framework of the Research Unit “Nichtlineare Dynamik komplexer Kontinua” (FOR 608).

REFERENCES

1. J. Gelles, B. J. Schnapp, and M. P. Sheetz, “Tracking kinesin-driven movements with nanometre-scale precision,” *Nature* **331**, 450–453 (1988).
2. E. R. Weeks, J. C. Crocker, A. C. Levitt, A. Schofield, and D. A. Weitz, “Three-dimensional direct imaging of structural relaxation near the colloidal glass transition,” *Science* **287**, 627–631 (2000).
3. B. W. Hicks and K. J. Angelides, “Tracking movements of lipids and Thy1 molecules in the plasmalemma of living fibroblasts by fluorescence video microscopy with nanometer scale precision,” *J. Membrane Biol.* **144**, 231–244 (1995).
4. M. J. Saxton and K. Jacobson, “Single-particle tracking: applications to membrane dynamics,” *Annu. Rev. Biophys. Biomol. Struct.* **26**, 373–399 (1997).
5. M. Goulian and S. M. Simon, “Tracking single proteins within cells,” *Biophys. J.* **79**, 2188–2198 (2000).
6. J. Kirstein, B. Platschek, Ch. Jung, R. Bein, Th. Brown, and Ch. Bräuchle, “Exploration of nanostructured channel systems with single-molecule probes,” *Nat. Mater.* **6**, 303–310 (2007).
7. S. Wieser and G. J. Schütz, “Tracking single molecules in the live cell plasma membrane—do’s and don’t’s,” *Methods* **46**, 131–140 (2008).
8. B. Schulz, D. Tauber, F. Friedriszik, H. Graaf, J. Schuster, and C. von Borczyskowski, “Optical detection of heterogeneous single molecule diffusion in thin liquid crystal films,” *Phys. Chem. Chem. Phys.* **12**, 11555–11564 (2010).
9. E. L. Elson, “Fluorescence correlation spectroscopy: past, present, future,” *Biophys. J.* **101**, 2855–2870 (2011).
10. M. von Smoluchowski, “Versuch einer mathematischen Theorie der Koagulationskinetik kolloider Lösungen,” *Z. Phys. Chem.* **92**, 129–168 (1917).
11. O. Bénichou, C. Chevalier, J. Klafter, B. Meyer, and R. Voituriez, “Geometry-controlled kinetics,” *Nat. Chem.* **2**, 472–477 (2010).
12. M. Hellmann, D. W. Heermann, and M. Weiss, “Anomalous reaction kinetics and domain formation on crowded membranes,” *Eruophys. Lett.* **94**, 18002 (2011).
13. C. R. Haramagatti, F. H. Schacher, A. H. E. Müller, and J. Köhler, “Diblock copolymer membranes investigated by single-particle tracking,” *Phys. Chem. Chem. Phys.* **13**, 2278–2284 (2011).

14. E. L. Elson, "Fluorescence correlation spectroscopy and photobleaching recovery," *Annu. Rev. Phys. Chem.* **36**, 379–406 (1985).
15. E. L. Elson and D. Madsen, "Fluorescence correlation spectroscopy. I. Conceptual basis and theory," *Biopolymers* **13**, 1–27 (1974).
16. J. G. Ritter, R. Veith, J.-P. Siebrasse, and U. Kubitschek, "High-contrast single-particle tracking by selective focal plane illumination microscopy," *Opt. Express* **16**, 7142–7152 (2008).
17. M. Speidel, A. Jonáš, and E.-L. Florin, "Three-dimensional tracking of fluorescent nanoparticles with subnanometer precision by use of off-focus imaging," *Opt. Lett.* **28**, 69–71 (2003).
18. M. A. Thompson, M. D. Lew, M. Badieirostami, and W. E. Moerner, "Localizing and tracking single nanoscale emitters in three dimensions with high spatiotemporal resolution using a double-helix point spread function," *Nano Lett.* **10**, 211–218 (2009).
19. B. J. Schnapp, J. Gelles, and M. P. Sheetz, "Nanometer-scale measurements using video light microscopy," *Cell Motil. Cytoskel.* **10**, 47–53 (1988).
20. Th. Schmidt, G. J. Schütz, W. Baumgartner, H. J. Gruber, and H. Schindler, "Imaging of single molecule diffusion," *Proc. Natl. Acad. Sci. USA* **93**, 2926–2929 (1996).
21. M. Dahan, T. Laurence, F. Pinaud, D. S. Chemla, A. P. Alivisatos, M. Sauer, and S. Weiss, "Time-gated biological imaging by use of colloidal quantum dots," *Opt. Lett.* **26**, 825–827 (2001).
22. M. B. Forstner, J. Käs, and D. Martin, "Single lipid diffusion in Langmuir monolayers," *Langmuir* **17**, 567–570 (2001).
23. L. Holtzer, T. Meckel, and Th. Schmidt, "Nanometric three-dimensional tracking of individual quantum dots in cells," *Appl. Phys. Lett.* **90**, 053902 (2007).
24. E. J. G. Peterman, H. Sosa, and W. E. Moerner, "Single-molecule fluorescence spectroscopy and microscopy of biomolecular motors," *Annu. Rev. Phys. Chem.* **55**, 79–96 (2004).
25. G. Seisenberger, M. U. Ried, Th. Endress, H. Buning, M. Hallek, and Ch. Bräuchle, "Real-time single-molecule imaging of the infection pathway of an adeno-associated virus," *Science* **294**, 1929–1932 (2001).
26. J. Enderlein, "Positional and temporal accuracy of single molecule tracking," *Sing. Mol.* **1**, 225–230 (2000).
27. J. Enderlein, "Tracking of fluorescent molecules diffusing within membranes," *Appl. Phys. B* **71**, 773–777 (2000).
28. Y. Katayama, O. Burkacky, M. Meyer, Ch. Bräuchle, E. Gratton, and D. C. Lamb, "Real-time nanomicroscopy via three-dimensional single-particle tracking," *Chem. Phys. Chem.* **10**, 2458–2464 (2009).
29. K. McHale, A. J. Berglund, and H. Mabuchi, "Quantum dot photon statistics measured by three-dimensional particle tracking," *Nano Lett.* **7**, 3535–3539 (2007).
30. A. J. Berglund and H. Mabuchi, "Feedback controller design for tracking a single fluorescent molecule," *Appl. Phys. B* **78**, 653–659 (2004).
31. V. Levi, Q. Ruan, and E. Gratton, "3-D particle tracking in a two-photon microscope: application to the study of molecular dynamics in cells," *Biophys. J.* **88**, 2919–2928 (2005).
32. V. Levi, Q. Ruan, K. Kis-Petikova, and E. Gratton, "Scanning FCS, a novel method for three-dimensional particle tracking," *Biochem. Soc. Trans.* **31**, 997–1000. (2003).
33. A. J. Berglund and H. Mabuchi, "Tracking-FCS: fluorescence correlation spectroscopy of individual particles," *Opt. Express* **13**, 8069–8082 (2005).
34. K. Kis-Petikova and E. Gratton, "Distance measurement by circular scanning of the excitation beam in the two-photon microscope," *Microsc. Res. Tech.* **63**, 34–49 (2004).
35. Q. Wang and W. E. Moerner, "Optimal strategy for trapping single fluorescent molecules in solution using the ABEL trap," *Appl. Phys. B* **99**, 23–30 (2010).
36. Q. Wang and W. E. Moerner, "An adaptive anti-Brownian electrokinetic trap with real-time information on single-molecule diffusivity and mobility," *ACS Nano* **5**, 5792–5799 (2011).
37. H. Qian, M. P. Sheetz, and E. L. Elson, "Single particle tracking. Analysis of diffusion and flow in two-dimensional systems," *Biophys. J.* **60**, 910–921 (1991).
38. R. Metzler and J. Klafter, "The restaurant at the end of the random walk: recent developments in the description of anomalous transport by fractional dynamics," *J. Phys. A* **37**, R161–R208 (2004).
39. J.-P. Bouchaud and A. Georges, "Anomalous diffusion in disordered media: statistical mechanisms, models and physical applications," *Phys. Rep.* **195**, 127–293 (1990).
40. D. S. Martin, M. B. Forstner, and J. A. Käs, "Apparent subdiffusion inherent to single particle tracking," *Biophys. J.* **83**, 2109–2117 (2002).
41. A. J. Berglund and H. Mabuchi, "Performance bounds on single-particle tracking by fluorescence modulation," *Appl. Phys. B* **83**, 127–133 (2006).
42. M. L. Sheely, "Glycerol viscosity tables," *Ind. Eng. Chem.* **24**, 1060–1064 (1932).
43. G. J. Schütz, H. Schindler, and T. Schmidt, "Single-molecule microscopy on model membranes reveals anomalous diffusion," *Biophys. J.* **73**, 1073–1080 (1997).
44. A. V. Weigel, B. Simon, M. M. Tamkun, and D. Krapf, "Ergodic and nonergodic processes coexist in the plasma membrane as observed by single-molecule tracking," *Proc. Natl. Acad. Sci. USA* **108**, 6438–6443 (2011).
45. K. Halbach, "Matrix representation of Gaussian optics," *Am. J. Phys.* **32**, 90–108 (1964).
46. A. Ashkin, J. M. Dziedzic, J. E. Bjorkholm, and S. Chu, "Observation of a single-beam gradient force optical trap for dielectric particles," *Opt. Lett.* **11**, 288–290 (1986).
47. K. C. Neumann and S. M. Block, "Optical trapping," *Rev. Sci. Instrum.* **75**, 2787–2809 (2004).

PUBLICATION P2

Measuring a diffusion coefficient by single-particle tracking: Statistical analysis of experimental mean-squared-displacement curves

Dominique Ernst and Jürgen Köhler

published in:

Phys. Chem. Chem. Phys. **15**, 845-849, (2013)
Electronic supplementary information (ESI) available

©Royal Society of Chemistry 2013
<http://dx.doi.org/10.1039/c2cp43433d>

Measuring a diffusion coefficient by single-particle tracking: statistical analysis of experimental mean squared displacement curves†

Cite this: *Phys. Chem. Chem. Phys.*, 2013, **15**, 845

Dominique Ernst and Jürgen Köhler*

We provide experimental results on the accuracy of diffusion coefficients obtained by a mean squared displacement (MSD) analysis of single-particle trajectories. We have recorded very long trajectories comprising more than 1.5×10^5 data points and decomposed these long trajectories into shorter segments providing us with ensembles of trajectories of variable lengths. This enabled a statistical analysis of the resulting MSD curves as a function of the lengths of the segments. We find that the relative error of the diffusion coefficient can be minimized by taking an optimum number of points into account for fitting the MSD curves, and that this optimum does not depend on the segment length. Yet, the magnitude of the relative error for the diffusion coefficient does, and achieving an accuracy in the order of 10% requires the recording of trajectories with about 1000 data points. Finally, we compare our results with theoretical predictions and find very good qualitative and quantitative agreement between experiment and theory.

Received 28th September 2012,
Accepted 13th November 2012

DOI: 10.1039/c2cp43433d

www.rsc.org/pccp

1 Introduction

Diffusion is often exploited to examine interactions and movements of individual nanoscopic objects in soft matter and/or biological environments on a molecular length scale.^{1–10} Early experimental work was carried out using fluorescence recovery after photobleaching (FRAP)¹¹ which yields the ensemble average of the diffusing particles and which is, dictated by the diffraction of light, restricted in spatial resolution to length scales of about 200–300 nm. Alternatively, researchers employed fluorescence correlation spectroscopy (FCS),^{12,13} which provides the average over a number of individual objects that are registered sequentially and from which it is assumed that they behave uniformly. Since about two decades single-particle tracking (SPT) became a valuable tool to map out the movement of an individual particle with high spatial and temporal resolution.^{1–4,14–21} The developed methodology covers techniques where the movement of an individual particle can be followed by recording its diffraction-limited image on a sequence of CCD frames,¹ sophisticated approaches that compensate the Brownian motion using

electrokinetic forces,¹⁴ techniques that use structured illumination by actively designing the point-spread function of the microscope,^{21,22} as well as methods that rely on a spatial modulation of the light that travels to or comes from the particle.¹⁹ Fascinating results have been obtained, for example in biophysics the movement of molecules, viruses, or motor proteins could be made visible,^{4–6} and in the materials science transport processes through nanoporous structures^{7,8} or the manifestation of diffusion anomalies in liquid crystals and mesoporous structures could be followed.^{9,23,24}

Typically the fluorescence of a particle is monitored as a function of time and the position of the particle is extracted from the data with sub-diffraction limited accuracy. This provides the trajectory $r(t)$ of the particle that is commonly analysed in terms of the mean squared displacement (MSD). For a 2-dimensional diffusion process the MSD generally scales with a power law according to $\text{MSD}(\tau) = 4\tilde{D}\tau^\alpha$, where \tilde{D} is the generalized diffusion coefficient, and α the anomaly parameter. For $\alpha = 1$ the underlying process corresponds to normal diffusion (Brownian motion)²⁵ and \tilde{D} reduces to the diffusion coefficient D known from Einstein.²⁶ Otherwise the process is called subdiffusive ($\alpha < 1$) or superdiffusive ($\alpha > 1$).

For obvious reasons an experimental trajectory can only be recorded with a distinct temporal resolution, it suffers from localisation errors due to the movement of the particle during data acquisition,²⁷ it is affected by unavoidable signal-to-noise

Experimental Physics IV and Bayreuth Institute of Macromolecular Research (BIME), University of Bayreuth, 95440 Bayreuth, Germany. E-mail: juergen.koehler@uni-bayreuth.de; Fax: +49 921 55 4002; Tel: +49 921 55 4000

† Electronic supplementary information (ESI) available: Analysis of all measured trajectories. See DOI: 10.1039/c2cp43433d

limitations²⁸ and last but not least it is inherently of finite length. Hence, it is of crucial importance to understand how accurate the diffusion coefficient can be extracted from a real experimental MSD curve.^{25,29,30} Although the mathematical framework for the MSD analysis is known for many years, the implications of the experimental limitations on the accuracy of the measured parameters have been considered in detail only recently.^{29,31} These studies address the achievable precision for the diffusion coefficient that can be obtained from a given MSD curve as a function of the experimental parameters mentioned above. In order to test their theoretical results the authors had to rely on fictitious tracking experiments based on simulations rather than on experimental data. The reason is that a sophisticated statistical analysis of the tracking data requires a very large data set which is difficult to obtain, because the particle might get lost for tracking due to diffusion out of the focal volume or due to photobleaching. Often it is already a great challenge to register trajectories consisting of some hundred data points. Naively speaking, a trajectory of arbitrary length could be acquired by repeating a tracking experiment under exactly the same experimental conditions on several nanoparticles. However, since even nominally identical nanoparticles are slightly different in shape and size, the statistics of the (unknown) size distribution of the nanoparticles will be superimposed on the statistics of the diffusion coefficient. Moreover, the precision with which the diffusion coefficient can be determined from a MSD curve depends on the accuracy of the MSD data points and on the number of fitting points that are taken into account.^{29,30} Therefore, the numerous theoretical and numerical developments that allow assessment of the experimental shortcomings still await experimental verification.

In this work we use single-particle orbit tracking, which allows us to obtain single-particle trajectories that consist of more than 1.5×10^5 data points with a temporal resolution of 4 ms and a spatial accuracy of better than 10 nm.³² Such a long trajectory can be divided into a sequence of segments, where each segment can be considered as an individual trajectory that, by definition, has been recorded on exactly the same particle under identical experimental conditions. This enables us to evaluate the statistics of the diffusion coefficient extracted from the segments as a function of the length of the segments and to compare the results with the theoretical predictions made in the literature.^{25,29}

2 Experimental section

2.1 Sample preparation

For the single-particle tracking experiments we use fluorescent beads with a diameter of 20 nm that are loaded with Nile red (Molecular Probes, 20 mg mL⁻¹ dissolved in water). This solution is further diluted in water to a concentration of 0.1 nM and subsequently mixed with pure glycerol (Sigma) resulting in a concentration of 2 pM for the tracers. From that solution a drop of about 25 μ L is sandwiched between two microscope coverslips that are cleaned with acetone. In order to prevent evaporation of the solvent (and the resulting flow field in the sample) the edges of the coverslips are sealed with grease (High-Vacuum Grease, Wacker).

This construct is mounted on top of a 3-axis piezo stage (Tritor 102, piezosystem Jena) providing a scan range of 100 μ m for each axis. All experiments are performed at room temperature, *i.e.* (21 ± 0.5) °C.

2.2 Experimental setup

The home-built setup for single-particle orbit tracking has been described in great detail in a separate paper.³² Briefly, the output from an Ar/Kr-ion laser (Innova 70C Spectrum, Coherent) operated at 514 nm is guided through a deflection unit consisting of two mutually perpendicular arranged acousto optical deflectors (AOD, DTSX-400-532, Pegasus) that generate a rotating light orbit. This orbit is projected via a dichroic beam splitter (z532RDC, AHF) towards an infinity-corrected water-immersion objective (UPLSAPO, 60 \times , NA = 1.2, Olympus). This results in a focussed laser beam with a waist of $w = 270$ nm that rotates on an orbit with a radius of $R = 190$ nm in the focal plane of the objective. The frequency of the rotation can be adjusted by the AODs and is set to 1 kHz.

The emission of the fluorescent nanoparticles is collected with the same objective, passes the dichroic and is focussed either onto the chip of a CCD (sencam qe, PCO) or an avalanche photo diode (SPCM-AQR-14, Perkin Elmer). Residual laser light that passes the dichroic is suppressed by a dielectric optical filter (HQ545LP, OD = 6 at 514 nm, AHF). To spot the location of the tracers we operate the setup in widefield mode. Therefore the deflection unit is switched off and an additional lens in the excitation path defocusses the laser light to an area of $80 \times 80 \mu\text{m}^2$. With the aid of the piezo stage an appropriate particle is moved close to the position where the light orbit will appear (centre of the field of view). Subsequently, the optics are switched to confocal mode, the light orbit is generated and the algorithm for automated tracking is started.

We record the emission intensity of the fluorescent particle which is modulated by the frequency of the rotating laser focus. By demodulating this emission signal we are able to calculate the x -, y -position of the particle with respect to the centre of the orbit. The position provides a feedback signal for the piezo and the particle is moved (together with the sample) back to the centre of the orbit. These steps (collect emission – calculate position – move piezo) are repeated continuously, which allows us to reconstruct the movement of a fluorescent tracer particle for more than 10 minutes with a spatial resolution of better than 10 nm. The temporal resolution of the experiments is $\Delta t = 4$ ms which results in trajectories of $N = 1.5 \times 10^5$ x -, y -position pairs.

3 Results and discussion

An example for a typical trajectory measured with our setup is displayed in Fig. 1. It represents 1.52×10^5 data points and corresponds to an elapsed time of 608 s which is indicated by the colour code, where blue corresponds to the start of the trajectory and red to its end. In order to mimic to have only shorter trajectories with less data points we cut the long trajectory into segments that were treated as independent

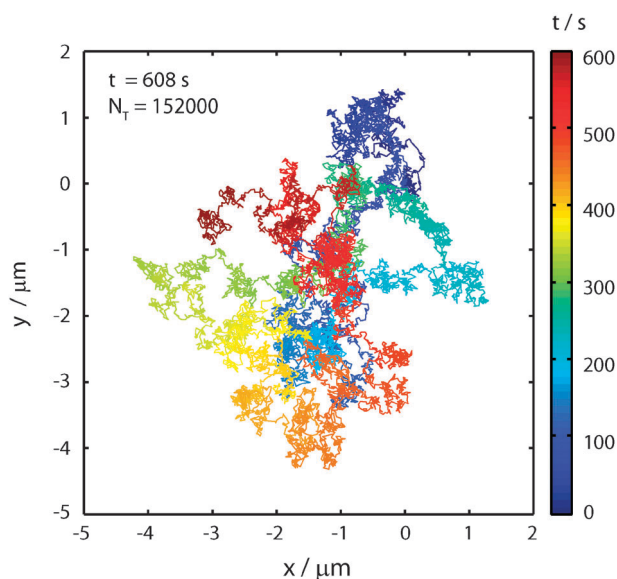


Fig. 1 Example of a trajectory of a 20 nm sized bead in pure glycerol. The colour code refers to the elapsed time of 608 s ($N = 1.52 \times 10^5$ data points; blue corresponds to the start and red corresponds to the end).

trajectories of shorter length. In the following we denote the length of the full trajectory as N_T (here $N_T = 1.52 \times 10^5$) and the length of a segment as N_{seg} . For our study we choose $N_{\text{seg}} = 10, 20, 40, 60, 80, 100, 200, 400, 600, 800$, and 1000, which yields ensembles of N_T/N_{seg} short trajectories of equal length. The idea is now to determine the diffusion coefficient D from the slope of the time-averaged MSDs of each segment and to examine the statistical variation of D within each ensemble of trajectories. Yet, according to ref. 29 there exists an optimum number of data points of the MSD that should be considered to obtain the best result for the diffusion coefficient. This can be understood as follows. For increasing lag times the accuracy of the data points in the MSD decreases due to the progressively decreasing averaging of the available data. For example, the first data point of the MSD represents an average over $(N_{\text{seg}} - 1)$ positions of the particle whereas the last data point has not been averaged at all. Hence, fitting the slope of the MSD curve by taking too many data points into account leads to a deterioration rather than an improvement of the result. On the other hand, the very first points of the MSD are stronger subjected to localisation errors, either due to noise (static error) or due to blurring of the position of the particle during data acquisition (dynamic error). Both effects average out for MSD points at longer lag times.

As a consequence of this, we first have to find out the optimum number of data points that should be considered for fitting the slope of the MSD. In the following, the protocol for doing so will be explained on the example of $N_{\text{seg}} = 1000$ which yields an ensemble of 152 trajectories of equal length and the same number of MSD curves. For this ensemble we fitted the slope, D^* , of each MSD curve by an unweighted linear fit to the first n data points. More precisely, we have skipped the very first data point of the MSDs, because it turned out that it is strongly affected by residual oscillations of the piezo. These

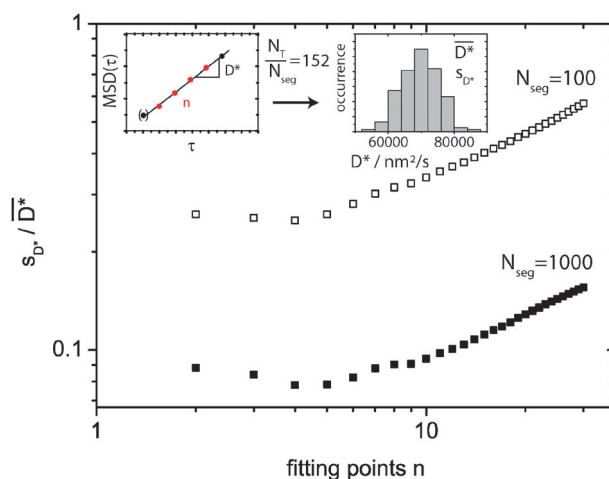


Fig. 2 Relative error of the slope D^* obtained from unweighted linear fits to the MSD curve as a function of the number of fitting points n for the segment length $N_{\text{seg}} = 100$ (open symbols) and $N_{\text{seg}} = 1000$ (full symbols). The inset top left displays schematically a MSD curve as a function of the lag time τ and the data points that are considered for the linear fit (red) to obtain D^* . For all fits the first data point of the MSD (brackets) is ignored (for details see text). The inset top right shows as an example for the distribution of the slopes within the ensemble of N_T/N_{seg} trajectories for $n = 4$ and $N_{\text{seg}} = 100$, from which $\overline{D^*}$ (first moment; empirical mean value) and s_{D^*} (second moment; empirical standard deviation) can be calculated.

oscillations affect the position determination and reduce the accuracy of the first point of the MSD curve, whereas the influence of these oscillations on the accuracy of the succeeding MSD points level off (for details see Experimental section and ref. 32). Therefore the fit was applied to the data points from 2 to $(n + 1)$ and the slope D^* of the MSD curves was determined as a function of n . In order to be compatible with the existing literature we prefer the slope D^* of the MSD curves rather than the diffusion coefficient $D = D^*/4$.²⁹ An example for the distribution of D^* is shown in the top right inset of Fig. 2 for $n = 4$, *i.e.* taking only the data points 2–5 for fitting the MSDs into account as indicated schematically in the top left inset of Fig. 2. Subsequently, we determined from each histogram the first and the second moment providing the empirical mean $\overline{D^*}$ and the empirical standard deviation s_{D^*} for this parameter, and plotted the ratio $s_{D^*}/\overline{D^*}$ as a function of the number of fitting points n . The result of this procedure is shown in Fig. 2 for the examples of $N_{\text{seg}} = 100$ and $N_{\text{seg}} = 1000$. For both samples, the relative error $s_{D^*}/\overline{D^*}$ first decreases for growing n and then rapidly increases if more fitting points are taken into account. Here we find an optimum for the accuracy of the slope of the MSDs for $n = 4$. While the relative accuracy that can be achieved for D^* (about 8% for $N_{\text{seg}} = 1000$, and about 25% for $N_{\text{seg}} = 100$) clearly depends on the lengths of the segments, it is interesting to note that the number of fitting points n that yield the optimum result does not.

In order to facilitate a quantitative comparison of the data shown in Fig. 2 with the theoretical predictions in the literature²⁹ we have to resort to the reduced localisation error $x = \sigma^2/D\Delta t$, where σ is the localisation error, D the diffusion

coefficient, and Δt the temporal resolution. A good estimate for the diffusion coefficient is obtained from a linear fit to the data points 2–5 of the time-averaged MSD from the total trajectory of 1.52×10^5 data points, which yields $D_T = 17.45 \times 10^{-3} \mu\text{m}^2 \text{s}^{-1}$. Using $\sigma = 7.5 \text{ nm}^{32}$ and $\Delta t = 4 \text{ ms}$ we obtain $x \approx 0.8$ and find a good agreement between experiment and theory (see Fig. 6 for $x = 1$ in ref. 29).

Next we investigated the influence of the length of the segments on the outcome of the experimentally determined diffusion coefficient. Therefore we analysed the MSDs from 15 200 segments with a length of $N_{\text{seg}} = 10$, from 7600 segments with a length of $N_{\text{seg}} = 20$ and so on until 152 segments with a length of $N_{\text{seg}} = 1000$, by applying a linear fit to the data points 2–5 of the respective MSD curves. The resulting distributions for the diffusion coefficients $D = D^*/4$ are shown in Fig. 3 as a function of N_{seg} . For better comparison the histograms were scaled with the number of sub-trajectories in each ensemble, N_T/N_{seg} . For the short segments the distributions were asymmetric and extremely broad with a long tail toward larger values of the diffusion coefficient testifying that diffusion coefficients obtained from trajectories consisting only of a few data points are not very meaningful. As N_{seg} increases the distributions narrow down and become more symmetric. The shape and profile of the experimental distributions presented here are consistent with theory.³⁰

The distributions presented in Fig. 3 can be interpreted as the empirical probability density functions (PDFs) to measure a distinct range of values for the diffusion coefficient for a given length N_{seg} of the trajectory. This tells us that for trajectories with a length in the order of 100 data points (black bold line in Fig. 3), which would be very reasonable for experiments in biological environments, the actual outcome of an experiment for the diffusion coefficient can vary by more than a factor of 2. For each of these empirical probability densities, the best

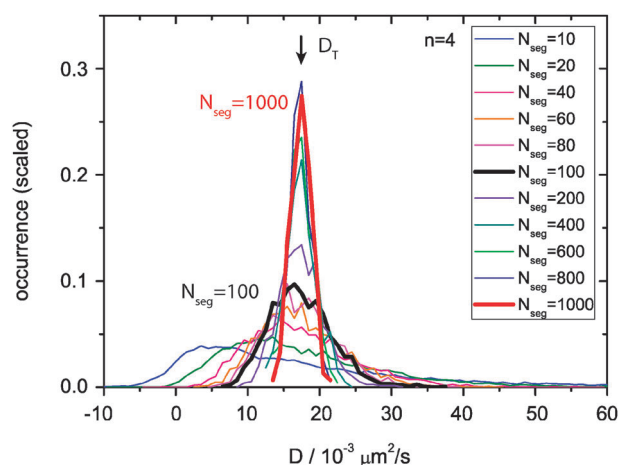


Fig. 3 Distributions of diffusion coefficients as a function of the segment length N_{seg} . For comparison, the distributions were scaled with the number of trajectories N_T/N_{seg} within the corresponding ensemble. The diffusion coefficients were obtained from linear fits to the MSD curves using $n = 4$ fitting points. The arrow on top of the distributions indicates the diffusion coefficient D_T determined from the time-averaged MSD of the full trajectory with a length of $N_T = 1.52 \times 10^5$ data points. The distributions for $N_{\text{seg}} = 100, 1000$ are highlighted by the bold lines.

estimate for the actual diffusion coefficient corresponds to the mean value \bar{D} (first moment) which is displayed in Fig. 4 (open squares) together with the corresponding empirical standard deviations (second moment, black error bars) as a function of N_{seg} . Interestingly the mean values show only little variation as a function of N_{seg} which is shown in the inset of Fig. 4 on an expanded scale.

In addition to the distribution of the diffusion coefficients as a function of the length of segments Qian *et al.*²⁵ derived an analytical expression for the standard deviation of these distributions which is given by $\sigma = \pm \bar{D}[2n/3(N_{\text{seg}} - n)]^{1/2}$ and which allows for comparison with the empirical standard deviation obtained experimentally. The calculated standard deviation is displayed in Fig. 4 by the red error bars. For better visualization both the experimental (black) and calculated (red) error bars are connected by the dashed and dotted lines, respectively. The systematically larger widths of the experimental error bars can be explained to result from errors in the position determination that were not considered in the theoretical calculation by Qian *et al.* Besides this minor discrepancy both characteristics are in good agreement. For $N_{\text{seg}} > 200$ the mean values of the distributions, \bar{D} , show only very little variation and are close to the value D_T obtained from the time-averaged MSD of the full trajectory (inset in Fig. 4, grey line).

However, it should be kept in mind that \bar{D} can only be determined if the distribution of D for the respective length of the trajectory is known. A single tracking experiment, for example with $N_{\text{seg}} = 100$, provides the diffusion coefficient only with an accuracy of about $\pm 25\%$. Achieving an accuracy of better than $\pm 10\%$ requires trajectories of $N_{\text{seg}} = 1000$ as testified in Fig. 2 and 3.

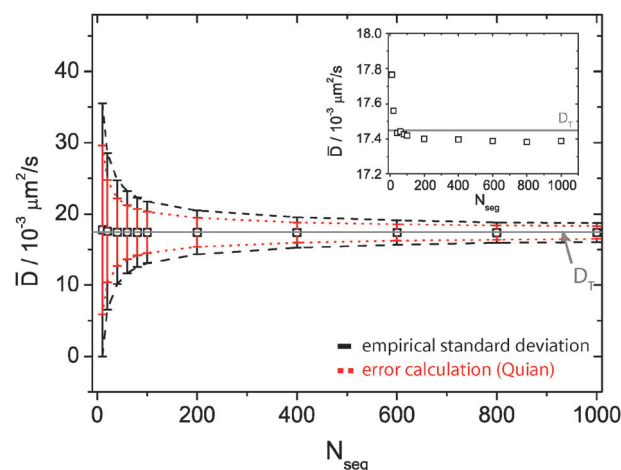


Fig. 4 Means of the diffusion coefficient, \bar{D} (open squares), and empirical standard deviations, s_D (black error bars), taken from the distributions shown in Fig. 3 as a function of the segment length N_{seg} . Theoretical values for the standard deviations (red error bars) have been calculated according to Qian *et al.*²⁵ using $\sigma = \pm \bar{D}[2n/3(N_{\text{seg}} - n)]^{1/2}$ and $n = 4$. As a guide for the eye the error bars are connected by the dashed (experimental data) and dotted (calculated data) lines. The inset displays the means of the diffusion coefficients on an enlarged scale. The grey line corresponds to the diffusion coefficient that is determined from the full time-averaged MSD curve of the full trajectory of 1.52×10^5 data points.

4 Conclusions

We analysed how the accuracy of the diffusion coefficient that is determined by fitting MSD curves depends on experimental parameters such as the length of the underlying trajectory and the number of fitting points of the MSD. This became possible by recording extremely long trajectories that could be cut into a large number of segments of variable lengths, thereby providing sufficiently large ensembles of (sub)trajectories that served for a statistical analysis. Our results were compared with theoretical predictions and we found good quantitative and qualitative agreement between experiment and theory.

The analysis presented was based on data from a single very long trajectory. In total we measured 7 very long trajectories from different tracers and found similar results. These are summarized in the ESI.†

Acknowledgements

We thank Florian Schwaiger for fruitful discussions and gratefully acknowledge financial support from the German Science Foundation (DFG) within the framework of the Research Unit “Nichtlineare Dynamik komplexer Kontinua” (FOR 608).

References

- 1 J. Gelles, B. J. Schnapp and M. P. Sheetz, *Nature*, 1988, **331**, 450.
- 2 B. J. Schnapp, J. Gelles and M. P. Sheetz, *Cell Motil. Cytoskeleton*, 1988, **10**, 47.
- 3 B. W. Hicks and K. J. Angelides, *J. Membr. Biol.*, 1995, **144**, 231.
- 4 T. Schmidt, G. J. Schütz, W. Baumgartner, H. J. Gruber and H. Schindler, *Proc. Natl. Acad. Sci. U. S. A.*, 1996, **93**, 2926.
- 5 G. Seisenberger, M. U. Ried, T. Endreß, H. Buning, M. Hallek and C. Bräuchle, *Science*, 2001, **294**, 1929.
- 6 E. J. G. Peterman, H. Sosa and W. E. Moerner, *Annu. Rev. Phys. Chem.*, 2004, **55**, 79.
- 7 C. R. Haramagatti, F. H. Schacher, A. H. E. Müller and J. Köhler, *Phys. Chem. Chem. Phys.*, 2011, **13**, 2278.
- 8 J. Kirstein, B. Platschek, C. Jung, R. Brown, T. Bein and C. Bräuchle, *Nat. Mater.*, 2007, **6**, 303.
- 9 B. Schulz, D. Täuber, F. Friedriszik, H. Graaf, J. Schuster and C. v. Borzyskowski, *Phys. Chem. Chem. Phys.*, 2010, **12**, 11555.
- 10 D. Ernst, M. Hellmann, J. Köhler and M. Weiss, *Soft Matter*, 2012, **8**, 4886.
- 11 E. L. Elson, *Annu. Rev. Phys. Chem.*, 1985, **36**, 379.
- 12 E. L. Elson and D. Madge, *Biopolymers*, 1974, **13**, 1.
- 13 E. L. Elson, *Biophys. J.*, 2011, **101**, 2855.
- 14 Q. Wang and W. E. Moerner, *ACS Nano*, 2011, **5**, 5792.
- 15 Q. Wang and W. Moerner, *Appl. Phys. B: Lasers Opt.*, 2010, **99**, 23.
- 16 V. Levi, Q. Ruan, K. Kis-Petikova and E. Gratton, *Biochem. Soc. Trans.*, 2003, **31**, 997.
- 17 M. Speidel, A. Jonáš and E.-L. Florin, *Opt. Lett.*, 2003, **28**, 69.
- 18 A. J. Berglund and H. Mabuchi, *Appl. Phys. B: Lasers Opt.*, 2004, **78**, 653.
- 19 H. Cang, C. S. Xu, D. Montiel and H. Yang, *Opt. Lett.*, 2007, **32**, 2729–2731.
- 20 J. G. Ritter, R. Veith, J.-P. Siebrasse and U. Kubitschek, *Opt. Express*, 2008, **16**, 7142.
- 21 S. R. P. Pavani, M. A. Thompson, J. S. Biteen, S. J. Lord, N. Liu, R. J. Twieg, R. Piestun and W. E. Moerner, *Proc. Natl. Acad. Sci. U. S. A.*, 2009, **106**, 2995.
- 22 M. A. Thompson, M. D. Lew, M. Badieirostami and W. E. Moerner, *Nano Lett.*, 2010, **10**, 211.
- 23 B. Schulz, D. Täubner, J. Schuster, T. Baumgärtel and C. v. Borzyskowski, *Soft Matter*, 2011, **7**, 7431.
- 24 J. Schuster, F. Cichos and C. v. Borzyskowski, *Eur. Phys. J. E: Soft Matter Biol. Phys.*, 2003, **12**, 019.
- 25 H. Qian, M. P. Sheetz and E. L. Elson, *Biophys. J.*, 1991, **60**, 910.
- 26 A. Einstein, *Ann. Phys. (Berlin, Ger.)*, 1905, **322**, 549.
- 27 M. Goulian and S. M. Simon, *Biophys. J.*, 2000, **79**, 2188.
- 28 D. S. Martin, M. B. Forstner and J. A. Käs, *Biophys. J.*, 2002, **83**, 2109.
- 29 X. Michalet, *Phys. Rev. E: Stat., Nonlinear, Soft Matter Phys.*, 2010, **82**, 041914.
- 30 M. J. Saxton, *Biophys. J.*, 1997, **72**, 1744.
- 31 X. Michalet and A. J. Berglund, *Phys. Rev. E: Stat., Nonlinear, Soft Matter Phys.*, 2012, **85**, 061916.
- 32 D. Ernst, S. Hain and J. Köhler, *J. Opt. Soc. Am. A*, 2012, **29**, 1277.

Electronic Supplementary Information

Measuring a diffusion coefficient by single-particle tracking: Statistical analysis of experimental mean squared displacement curves

Dominique Ernst, and Jürgen Köhler*

1 Analysis of all trajectories

In the following, the results for all seven measured trajectories are summarized. Trajectory 1 corresponds to the one used to illustrate the analysis in the main paper.

1.1 Relative error of the slope of the MSD curves

Fig. 1 shows the relative errors of the slopes of the MSD curves as a function of the number of fitting points for the segment lengths $N_{seg} = 100$ and $N_{seg} = 1000$, respectively.

The data sets from the different trajectories feature qualitatively the same behaviour, and the best relative accuracy for the slope is obtained for 3 or 4 fitting points. The slight discrepancies between the data sets might reflect variations in the localisation errors. For the following evaluation of the data the number of fitting points that was taken into account was set to $n = 4$.

1.2 Distribution of diffusion coefficients

The distributions of the determined diffusion coefficients from all seven data sets have been determined as a function of the lengths of the segments N_{seg} , and are shown in fig. 2. The results for trajectory 1 are discussed in length in the body of the paper and are not reproduced here. The setup of fig. 2 is similar to that of fig. 3 (left) and fig. 4 (right) in the main text. For all trajectories the distributions and accuracies are qualitatively similar. Discrepancies with respect to the absolute value of the diffusion coefficient are ascribed to size variations of the tracked particles.

References

- 1 H. Qian, M. P. Sheetz and E. L. Elson, *Biophys. J.*, 1991, **60**, 910.

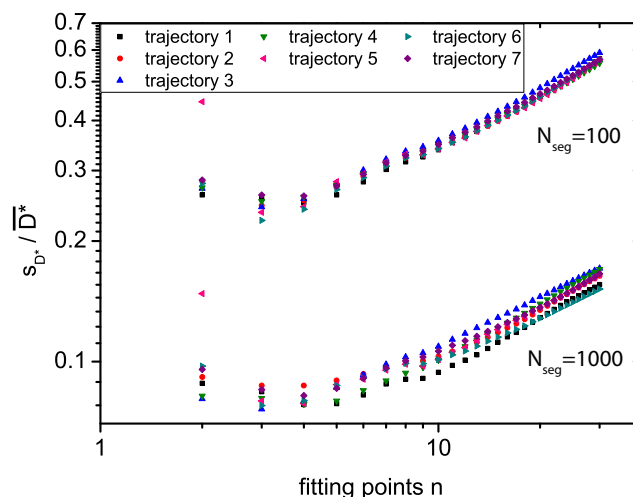
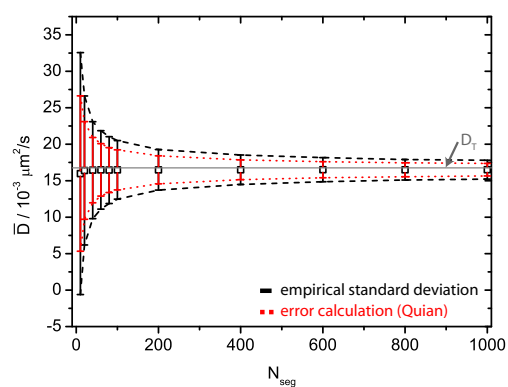
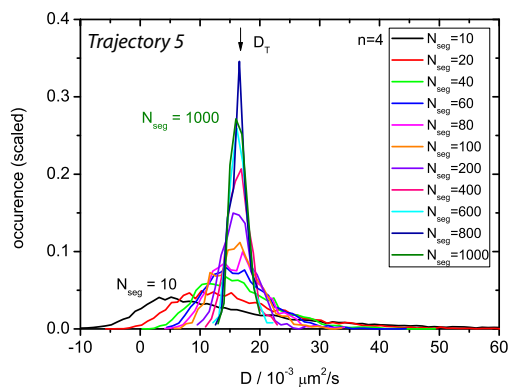
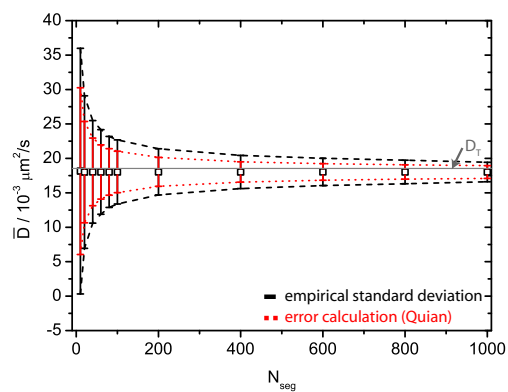
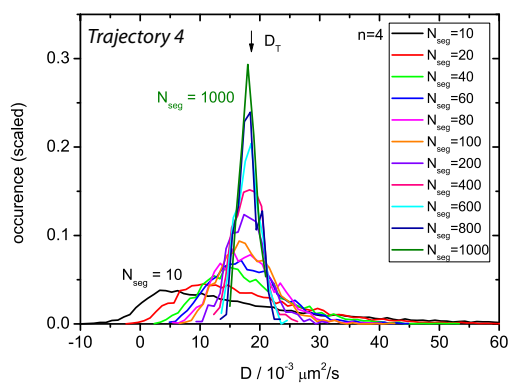
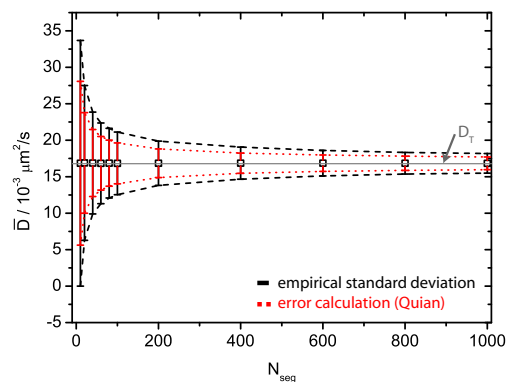
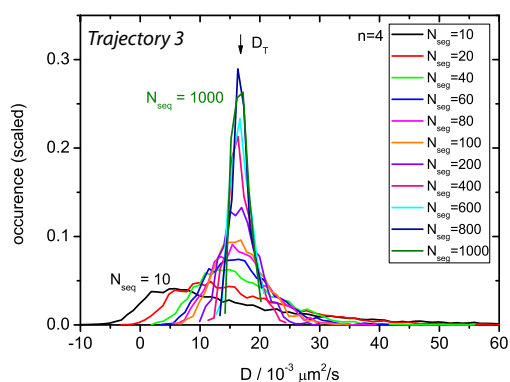
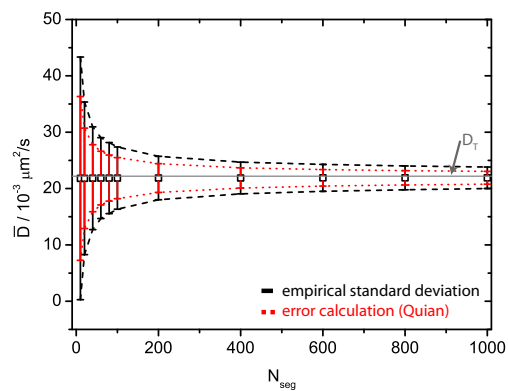
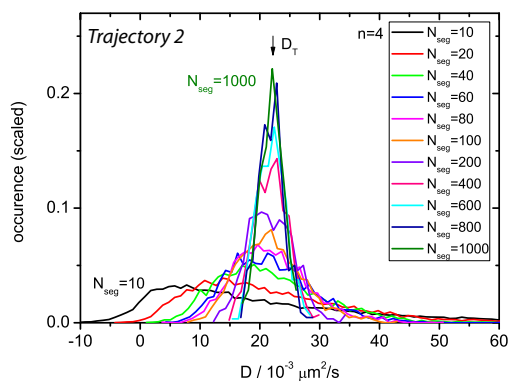


Fig. 1 (Color online) Relative error of the slopes D^* , obtained from unweighted linear fits to the MSD curve as a function of the number of fitting points n for the segment length $N_{seg} = 100$ and $N_{seg} = 1000$ for all measured trajectories. More details are given in the text and the main paper.



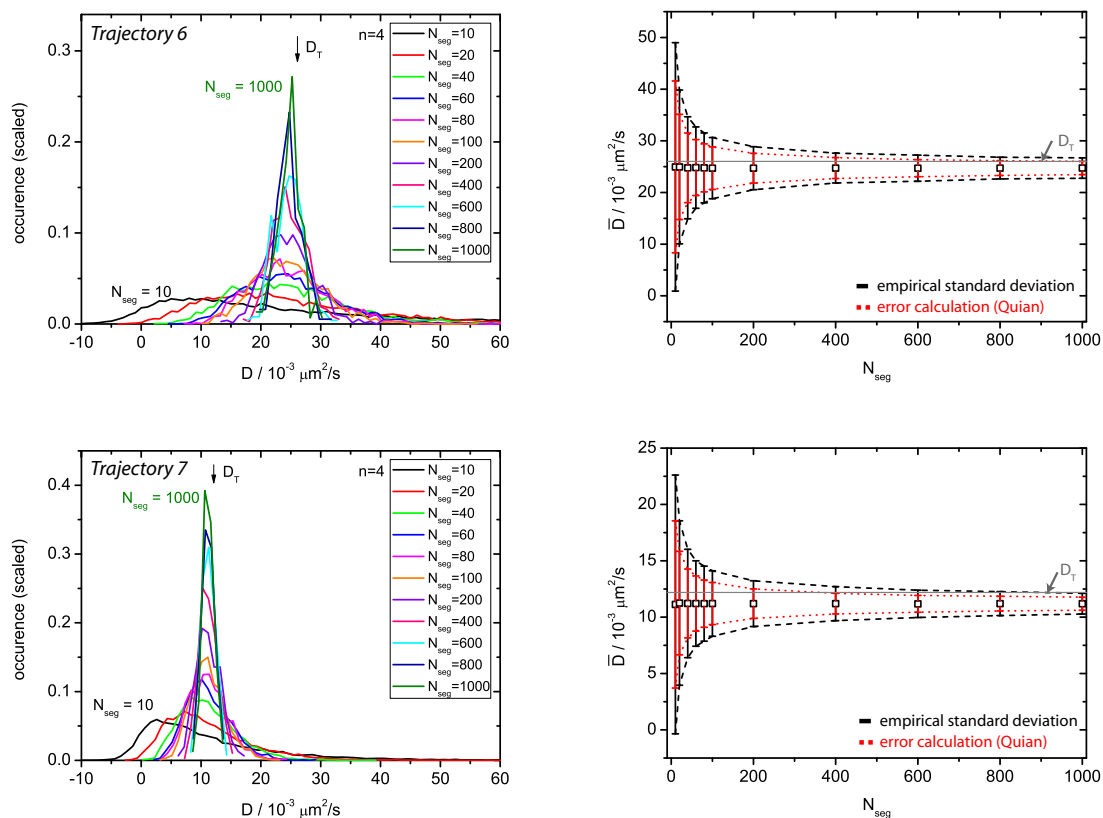


Fig. 2 (Color online) Summary of the distributions of the diffusion coefficients for all measured trajectories. Left: Distributions of the diffusion coefficients as a function of the segment lengths N_{seg} . All the diffusion coefficients were obtained from linear fits to the MSD curve using the optimal number of fitting points of $n = 4$. The arrow on top of the distributions indicates the diffusion coefficient of the corresponding full trajectory. Right: Mean values of the distributions of the diffusion coefficients \bar{D} (open squares) and empirical standard deviations (black error bars) as a function of the segment length N_{seg} . Theoretical values for the standard deviations (red error bars) have been calculated according to¹ using $\sigma = \pm \bar{D} [2n/3(N_{seg} - n)]^{1/2}$ and $n = 4$. As a guide for the eye the error bars are connected by the dashed (experimental data) and dotted (calculated data) lines. The grey line corresponds to the diffusion coefficient that is determined from a linear fit to the MSD curve of the corresponding full trajectory.

PUBLICATION P3

Fractional Brownian Motion in Crowded Fluids

Dominique Ernst, Marcell Hellmann, Jürgen Köhler and Matthias Weiss

published in:

Soft Matter **8**, 4886-4889, (2012)

Electronic supplementary information (ESI) available

©Royal Society of Chemistry 2012
<http://dx.doi.org/10.1039/C2SM25220A>

Cite this: *Soft Matter*, 2012, **8**, 4886

www.rsc.org/softmatter

Fractional Brownian motion in crowded fluids†

Dominique Ernst,^{‡a} Marcel Hellmann,^{‡b} Jürgen Köhler^{*a} and Matthias Weiss^{*b}

Received 30th January 2012, Accepted 22nd March 2012

DOI: 10.1039/c2sm25220a

Diffusion in crowded fluids, e.g. in the cytoplasm of living cells, has frequently been reported to show anomalous characteristics (so-called ‘subdiffusion’). Several random walk models have been proposed to explain these observations, yet so far an experimentally supported decision in favor of one of these models has been lacking. Here, we show that experimentally obtained trajectories in a prototypical crowded fluid show an asphericity that is most consistent with the predictions of fractional Brownian motion, i.e. an anti-correlated, anti-persistent generalization of normal Brownian motion that is related to the fluid’s viscoelasticity.

Macromolecular crowding, i.e. a total concentration of a variety of macromolecules up to 400 mg ml⁻¹, is a common phenomenon in intracellular fluids.¹ Crowding can have a considerable impact on (bio)chemical reactions,² hence challenging insights derived from biochemical assays in dilute aqueous solutions. The phosphorylation pattern of the mitogen-activated protein kinase (MAPK), for example, has been shown to vary greatly with the degree of cytoplasmic crowding.³ In dilute solutions, MAPK was twice phosphorylated by its kinase in a distributive manner, whereas adding artificial crowding agents resulted in a processive phosphorylation and hence a more efficient activation of MAPK. Recently, a theoretical explanation of these results has been given in terms of crowding-induced anomalous diffusion.⁴ Indeed, crowding is known to strongly alter the diffusional mobility of macromolecules.⁵ Apart from a mere reduction of the diffusion coefficient, i.e. an increased viscosity of the fluid, anomalous diffusion has also been frequently observed in crowded fluids *in vivo*^{6–10} and *in vitro*.^{11–15} Here, the mean square displacement (MSD) of a diffusing particle was shown to scale over several decades as $\langle r(t)^2 \rangle \sim t^\alpha$ with $\alpha < 1$ (‘subdiffusion’).

In spite of the frequent observation of subdiffusion, even in fairly unstructured fluids *in vitro*, an experimentally supported and unambiguous explanation of the effect in terms of a random walk model has remained elusive. So far, three types of random walks have been considered as an explanation of crowding-induced subdiffusion: (1) Obstructed diffusion (OD), i.e. the motion of a tracer particle in

a maze of immobile obstacles,¹⁶ (2) fractional Brownian motion (FBM) due to the viscoelasticity of the crowded fluid,¹⁵ and (3) a continuous time random walk (CTRW) in which the diffusing tracer takes power-law distributed rests between periods of free diffusion. The CTRW model is special since it shows weak ergodicity breaking^{17,18} whereas OD and FBM are ergodic random processes with stationary increments. Recent experimental data have indicated that CTRW may be less well suited to explain crowding-induced subdiffusion^{15,19} at least on short and intermediate time scales.²⁰

The main problem in relating experimental data to the above models is a lack of detailed information on the diffusion process: several techniques, e.g. fluorescence correlation spectroscopy, only report the MSD and leave all higher moments of the diffusion propagator undetermined. Single-particle tracking (SPT) techniques allow one to record individual trajectories and hence can overcome this limitation.^{21,22} However, precise position determination in SPT requires the collection of many photons of the moving tracer which sets limitations to the temporal resolution and the overall length of the recorded trajectory (due to bleaching of the dye). Yet, an unambiguous deciphering of the random walk model from fairly short SPT trajectories, often accompanied by an unfavorable spatial and temporal resolution, is challenging.

Here, we have utilized a fast and precise single-particle tracking technique to record particle trajectories with a length of 10⁵ positions and a spatio-temporal resolution of 10nm and 4ms. From trajectories in prototypical crowded and purely viscous fluids, we have determined the time- and ensemble-averaged MSD of the diffusing particle as well as the random walk’s asphericity. As a result, we have found that a transient, yet long-lasting subdiffusion emerged in a crowded but not in a purely viscous fluid. The anomaly was associated with an ergodic mode of motion as evidenced by a recently introduced ergodicity breaking parameter. Comparing the random walks’ asphericity with those predicted by computer simulations of normal Brownian motion, FBM, CTRW, and OD, we have found that our experimental data in crowded fluids are best described by the FBM model. Since FBM is closely related to viscoelasticity, we put forward the hypothesis that macromolecular crowding equips fluids with viscoelastic properties that enforce a fractional Brownian motion of diffusing tracer particles.

Single-particle tracking (SPT) is frequently limited by a poor temporal and/or spatial resolution as well as fairly short trajectories. These limitations can be overcome using a tracking technique that has been developed within the last few years:^{23–26} A Gaussian focus circles at high speed around a fluorescent particle with the particle

^aExperimental Physics IV, University of Bayreuth, 95440 Bayreuth, Germany. E-mail: juergen.koehler@uni-bayreuth.de

^bExperimental Physics I, University of Bayreuth, 95440 Bayreuth, Germany. E-mail: matthias.weiss@uni-bayreuth.de

† Electronic supplementary information (ESI) available: Experimental and Numerical Methods. See DOI: 10.1039/c2sm25220a

‡ These authors contributed equally to this work.

located at the position of the steepest gradient of the excitation intensity. Taking a diffusion step to escape this position is compensated by moving the sample stage *via* a negative feedback loop. Hence, the two-dimensional center-of-mass motion can be tracked with a high spatial and temporal resolution.

Using this approach (see the ESI† for the schematic setup and technical details), we were able to track fluorescent beads (diameter 50 nm) for up to ten minutes with a temporal resolution of $\Delta t = 4$ ms and a spatial accuracy of $\Delta r = 10$ nm. We have tracked particles in two prototypical fluids: (i) in a purely viscous solution obtained by mixing 60% sucrose (per weight) into water, and (ii) in a crowded fluid, where 30% dextran (500 kDa) was dissolved in water. For the latter, anomalous diffusion has already been reported previously.^{6,12} From a slightly higher number of acquired trajectories, we have retained for each fluid only those 21 SPT trajectories for further analysis that contained 4.5×10^4 – 1.5×10^5 positions without blanks, *i.e.* we discarded those few trajectories in which a weak emission signal lead to a transient loss of the tracked bead. The chosen trajectories did not show any signs of drift. Representative trajectories for both fluids are shown in the ESI.†

As a first step in the analysis, we calculated for each of the selected time traces $r_i \equiv r(t = i\Delta t)$ the time-averaged MSD,

$$\langle r(t)^2 \rangle_T = \frac{1}{N-k} \sum_{i=1}^{N-k} (r_i - r_{i+k})^2. \quad (1)$$

Representative time-averaged MSDs for sucrose and dextran solutions are shown in Fig. 1a. To highlight the emergence of a diffusion anomaly, we have divided out the leading order of the MSD, *i.e.* we have plotted $D(t) = \langle r(t)^2 \rangle_T / t$ as a function of t . While the purely viscous sucrose solution yielded a horizontal line, $D(t) = \text{const.}$, a transient power-law decay emerged for the crowded fluid. From the transient scaling $D(t) \sim 1/t^{0.2}$ (obtained within the grey shaded region), we inferred $\langle r(t)^2 \rangle_T \sim t^{0.8}$ for small and intermediate time scales. This observation is in quantitative agreement with previous reports¹⁵ on similar probes. Beyond $t \approx 1$ s a crossover towards normal diffusion emerges, *i.e.* $D(t)$ tends towards a horizontal line. Indeed, this behavior is expected for all of the above mentioned random walk models for subdiffusion since adapting them to a physical sample requires specification of a minimum and maximum length/time scale.

To determine the anomaly for each trajectory, we restricted the fitting process to the temporal range $50 \text{ ms} \leq t \leq 500 \text{ ms}$ which is not affected by some remaining inertia traces of the setup ($t < 50$ ms; see discussion in the ESI†) but also does not suffer from the emerging crossover to normal diffusion at large time scales. The resulting anomaly values, α , for all trajectories are summarized in Fig. 1b. A clear separation of the data for the purely viscous sucrose solution (average: $\langle \alpha \rangle = 0.98$) and the results for a crowded dextran solution (average: $\langle \alpha \rangle = 0.82$) can be seen.

From the observation $\langle r(t)^2 \rangle_T \sim t^\alpha$ we can already infer that the CTRW model with its distinct weak ergodicity breaking cannot describe the experimental data since it predicts^{17,18} $\langle r(t)^2 \rangle_T \sim t$. Indeed, even for a truncated CTRW model with only a transient scaling $p(\tau) \sim \tau^{-(1+\alpha)}$ of the distribution of waiting times one observes $\langle r(t)^2 \rangle_T \sim t$ (*cf.* ESI†). Hence, even a more realistic adaptation of the CTRW model appears incompatible with our experimental data.

Next, we calculated for all trajectories an ergodicity parameter¹⁷ that vanishes if ergodicity is preserved:

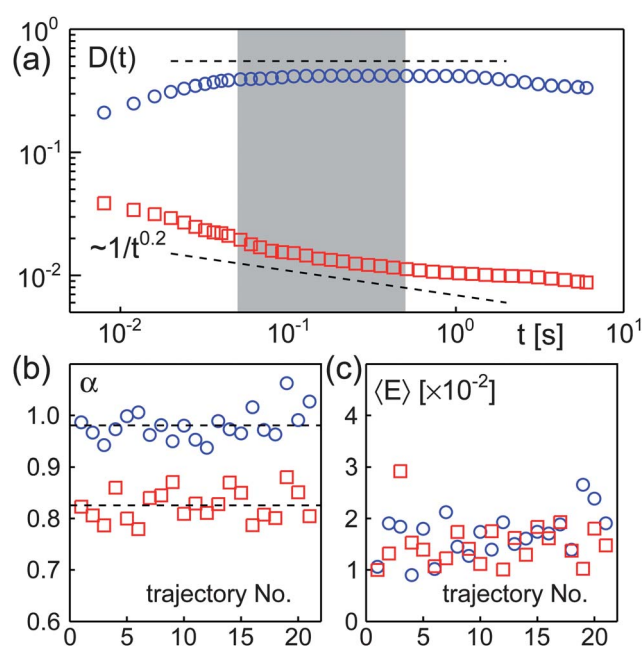


Fig. 1 (a) Representative time-averaged MSD, shown as $D(t) = \langle r(t)^2 \rangle_T / t$ to highlight the asymptotic scaling. Data for sucrose solutions (blue circles) follows the anticipated scaling for normal diffusion ($D(t) = \text{const.}$). In contrast, data for dextran solutions (red squares) shows a transient subdiffusion (dashed line, $D(t) \sim 1/t^{0.2}$). For $t > 1$ s a crossover to the asymptotic scaling ($\alpha = 1$, $D(t) = \text{const.}$) is visible. The grey shaded region indicates the temporal window in which the curves were fitted to extract the anomaly α . (b) Anomaly values α for each trajectory as obtained from fitting the time-averaged MSD in the indicated time window. A clear separation between a sucrose solution (blue circles, $\langle \alpha \rangle = 0.98$) and a crowded dextran solution (red squares, $\langle \alpha \rangle = 0.82$) is evident. (c) The ergodicity breaking parameter $\langle E \rangle$ [eqn (2)] of all trajectories was very small, indicating ergodicity.

$$E(t) = \frac{\left\langle \left\langle r(t)^2 \right\rangle_T^2 \right\rangle_E - \left\langle \left\langle r(t)^2 \right\rangle_T \right\rangle_E^2}{\left\langle \left\langle r(t)^2 \right\rangle_T \right\rangle_E^2} \quad (2)$$

To this end, we have cut each trajectory into segments of $N = 3000$ time steps and used these segments for the ensemble averaging $\langle \dots \rangle_E$. As a result, we observed that for all trajectories $\langle E \rangle \leq 0.03$ (Fig. 1c). Here, the average of $E(t)$ was taken in the same temporal window in which α was also determined. This result strongly supports the notion that all trajectories were ergodic. In particular, our data separates well from the predictions of a non-truncated CTRW model that yields a lower bound $E(\alpha \leq 0.9) \geq 0.1$.¹⁷ However, for the truncated CTRW model (*cf.* ESI†) we also obtained $E \approx 0.03$ on the experimentally relevant time scale. We attribute this effect to the truncation of $p(\tau)$ which narrows the distribution of apparent diffusion constants in $\langle r(t)^2 \rangle_T$.^{17,18} Hence, based only on E , a clear-cut decision that our experimental data is inconsistent with a truncated CTRW model is not possible.

We next inspected the trajectories' shape to gain deeper insights into the underlying type of random walk. The asphericity provides a simple yet powerful parameter to quantify the shape of fractal objects like random walks.²⁷ Diagonalizing the random walk's gyration tensor T_{ij} (*cf.* ESI†) yields the principal axes of gyration and

the corresponding eigenvalues, *i.e.* the squared principal radii of gyration, R_i^2 . Restricting ourselves to two dimensions (the experimental trajectories are two-dimensional objects), the asphericity is defined as

$$A = \langle (R_1^2 - R_2^2)^2 \rangle / \langle (R_1^2 + R_2^2)^2 \rangle. \quad (3)$$

We note that A involves an averaging over the ensemble of walks (indicated by $\langle \dots \rangle$). The limiting cases $A = 0$ and $A = 1$ resemble a perfect sphere and a simple rod, respectively. For Brownian motion in two dimensions an exact value is available:²⁷ $A = 4/7$. Hence, even an individual trajectory of a two-dimensional Brownian random walk differs drastically from a circular shape at each instant of time. The time-averaged orientation of the longest principal axis of gyration, however, is isotropic. Moreover, the isotropy of diffusion is also recovered in an ensemble of particles due to the uncorrelated random orientations of the gyration axes.

We have determined *via* simulations the values of A for FBM, OD, and a truncated CTRW at varying anomaly values α (see ESI† for details). Our simulation results revealed that for $0.5 \leq \alpha \leq 1$, which is the experimentally relevant regime, the asphericity changes almost linearly with α , *i.e.* $A = m_1\alpha + b_1$. For OD we found $m_1 = 0.120 \pm 0.006$, $b_1 = 0.458 \pm 0.004$ whereas for FBM we obtained $m_1 = 0.638 \pm 0.009$, $b_1 = -0.057 \pm 0.006$. For the truncated CTRW model we found $A \approx 4/7$ irrespective of α (*cf.* ESI†). This result can be rationalized by bearing in mind that a CTRW trajectory at any instance of time looks similar to the path of normal Brownian motion.

To compare our experimental trajectories to these predictions, we assigned the previously determined anomaly α to each trajectory (*cf.* Fig. 1b). Then, we calculated the accompanying asphericity: Since the anomaly reflects a scaling for short and intermediate times, a consistent estimate of the random walk's asphericity must relate to the same time scale. Therefore, each trajectory was cut into sequences of $N = 3000$ time steps of length Δt , and the average over these sub-trajectories yielded the (mean) asphericity [eqn (3)] of the entire trajectory on the length and time scales during which anomalous diffusion was observed. As can be seen from Fig. 2a, the cloud of data points for sucrose solutions overlaps well with the anticipated result for normal Brownian motion, *i.e.* the mean of all 21 data points ($\langle \alpha \rangle = 0.98$ and $\langle A \rangle = 0.58$) agrees quantitatively with the expectation $\alpha = 1$ and $A = 4/7 \approx 0.57$. Hence, sucrose solutions indeed feature normal Brownian trajectories also from the geometric perspective. In dextran solutions, however, we obtained $\langle \alpha \rangle = 0.82$ and $\langle A \rangle = 0.46$ which is most consistent with the simulation results for the FBM model that predicts locally a more spherical shape of the trajectory due to the anti-persistence of the random walk.

Given that FBM is closely related to the viscoelasticity of non-Newtonian and crowded fluids,^{13,28} the emergence of subdiffusion may be traced back to transient restoring forces on short length and time scales. It is hence meaningful to translate the SPT trajectories into the fluid's complex shear modulus,²⁸ $G(\omega) = G'(\omega) + iG''(\omega)$. Here, the real (imaginary) part of $G(\omega)$ represents the elastic (viscous) modulus of the fluid. Employing a semi-analytical approach, we have fitted the time-averaged MSD of each trajectory by an empirical expression $w(t) = a_0t^\alpha + a_1t$ to capture the transient anomaly and the asymptotic normal diffusion. The resulting fit parameters were then used to determine the complex shear modulus as described earlier.¹³ From the ensemble of complex shear moduli for each fluid, we have determined the minimum and maximum values of G' and G'' . As

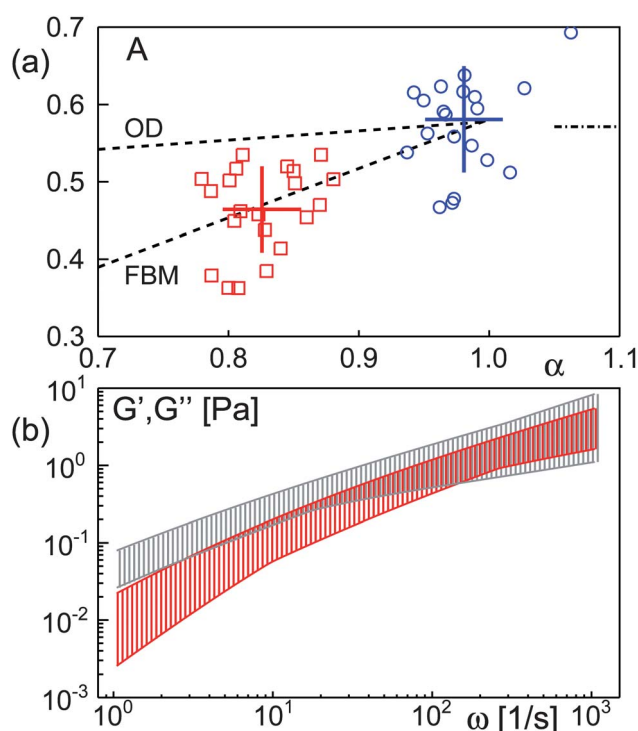


Fig. 2 (a) Asphericity A as a function of the anomaly α (data for sucrose and dextran shown as blue circles and red squares, respectively). Mean values (\pm standard deviation) are indicated by cross hairs. Dashed lines indicate simulation results for OD and FBM. Data for sucrose solutions are in very good agreement with the asymptotic value $A = 4/7$ for $\alpha = 1$ (dash-dotted mark), whereas data for dextran compare favorably to the predictions of FBM. (b) Elastic (red) and viscous (grey) moduli, G' and G'' , as obtained from the ensemble of trajectories in a crowded dextran solution. Shown are the minimum and maximum values for G' and G'' at each frequency ω , *i.e.* all trajectories lie within the indicated bands. For low frequencies the fluid is almost completely viscous whereas for $\omega > 100 \text{ s}^{-1}$, a clear viscoelastic behavior emerges.

expected, sucrose showed a vanishing elastic contribution whereas the crowded dextran solution showed a significant viscoelasticity for large frequencies (Fig. 2b). Since high frequencies are related to small times, this viscoelastic behavior is intimately linked to the transient subdiffusion observed for small and intermediate times. A similar viscoelastic behavior (related to subdiffusion) has been observed for the cytoplasm and nucleoplasm of living cells.^{13,29}

In conclusion, we have shown with an advanced SPT approach that a purely viscous sucrose solution features normal Brownian motion of tracer particles with an asphericity of the random walk that agrees very well with analytical predictions. In contrast, diffusion in a crowded dextran solution was anomalous ('subdiffusion'). Trajectories showed no signs of ergodicity breaking and their asphericity was in quantitative agreement with predictions of the FBM model. In contrast, obstructed diffusion (*i.e.*, a standard random site percolation model) and CTRW were incompatible with the experimental data. This result is corroborated by the associated complex shear modulus: A strong viscoelastic behavior of the crowded dextran solution was seen at high frequencies as expected due to the relation of FBM with viscoelastic media.

It is tempting to speculate about the reasons and consequences of our finding in the context of living matter. Since the degree of

cytoplasmic crowding appears to be conserved,²⁹ cells might have adapted to highly crowded conditions and aim at maintaining this state (*cf.* also discussion in ref. 2 and 29). Indeed, a potential benefit of FBM-like subdiffusion in cells is the increased return probability to a position in three-dimensional space. In particular, FBM with $\alpha < 2/3$ yields a bulk-filling random walk that can massively increase the capture probability to a target as compared to normal diffusion.³⁰ Moreover, an enhanced rebinding due to FBM most likely is the explanation for the recently observed phosphorylation enhancement of MAPK under crowded conditions.³⁴ As an enhanced recurrence is a generic feature of FBM-like subdiffusion, we expect that the behavior of a multitude of biochemical pathways in cells will have to be revisited and interpreted in light of our findings.

Acknowledgements

DE and JK gratefully acknowledge financial support by Research Unit FOR608. MH was partly financed by the German-Israeli Project Cooperation GA309/10. We would like to thank Stefan Hain for technical support.

References

- 1 J. Ellis and A. Minton, *Nature*, 2003, **425**, 27–28.
- 2 H. Zhou, G. Rivas and A. Minton, *Annu. Rev. Biophys.*, 2008, **37**, 375–397.
- 3 K. Aoki, M. Yamada, K. Kunida, S. Yasuda and M. Matsuda, *Proc. Natl. Acad. Sci. U. S. A.*, 2011, **108**, 12675–12680.
- 4 M. Hellmann, D. Heermann and M. Weiss, *Europhys. Lett.*, 2012, **97**, 58004.
- 5 J. Dix and A. Verkman, *Annu. Rev. Biophys.*, 2008, **37**, 247–263.
- 6 M. Weiss, M. Elsner, F. Kartberg and T. Nilsson, *Biophys. J.*, 2004, **87**, 3518–24.
- 7 I. Tolic-Norrelykke, E. Munteanu, G. Thon, L. Oddershede and K. Berg-Sorensen, *Phys. Rev. Lett.*, 2004, **93**, 078102.
- 8 I. Golding and E. Cox, *Phys. Rev. Lett.*, 2006, **96**, 098102.
- 9 S. Weber, A. Spakowitz and J. Theriot, *Phys. Rev. Lett.*, 2010, **104**, 238102.
- 10 V. Tejedor, O. Bénichou, R. Voituriez, R. Jungmann, F. Simmel, C. Selhuber-Unkel, L. Oddershede and R. Metzler, *Biohy. J.*, 2010, **98**, 1364–1372.
- 11 I. Wong, M. Gardel, D. Reichman, E. Weeks, M. Valentine, A. Bausch and D. Weitz, *Phys. Rev. Lett.*, 2004, **92**, 178101.
- 12 D. Banks and C. Fradin, *Biophys. J.*, 2005, **89**, 2960–2971.
- 13 G. Guigas, C. Kalla and M. Weiss, *Biophys. J.*, 2007, **93**, 316–23.
- 14 W. Pan, L. Filobelo, N. Pham, O. Galkin, V. Uzunova and P. Vekilov, *Phys. Rev. Lett.*, 2009, **102**, 058101.
- 15 J. Szymanski and M. Weiss, *Phys. Rev. Lett.*, 2009, **103**, 038102.
- 16 M. Saxton, *Biophys. J.*, 1994, **66**, 394–401.
- 17 Y. He, S. Burov, R. Metzler and E. Barkai, *Phys. Rev. Lett.*, 2008, **101**, 058101.
- 18 A. Lubelski, I. Sokolov and J. Klafter, *Phys. Rev. Lett.*, 2008, **100**, 250602.
- 19 M. Magdziarz, A. Weron, K. Burnecki and J. Klafter, *Phys. Rev. Lett.*, 2009, **103**, 180602.
- 20 J.-H. Jeon, V. Tejedor, S. Burov, E. Barkai, C. Selhuber-Unkel, K. Berg-Sorensen, L. Oddershede and R. Metzler, *Phys. Rev. Lett.*, 2011, **106**, 048103.
- 21 B. Hicks and K. Angelides, *J. Membr. Biol.*, 1995, **144**, 231–244.
- 22 T. Schmidt, G. Schutz, W. Baumgartner, H. Gruber and H. Schindler, *Proc. Natl. Acad. Sci. U. S. A.*, 1996, **93**, 2926–2929.
- 23 J. Enderlein, *Appl. Phys. B: Lasers Opt.*, 2000, **71**, 773–777.
- 24 K. Kis-Petikova and E. Gratton, *Microsc. Res. Tech.*, 2004, **63**, 34.
- 25 A. Berglund and H. Mabuchi, *Appl. Phys. B: Lasers Opt.*, 2004, **78**, 653.
- 26 Y. Katayama, O. Burkacky, M. Meyer, C. Brauchle, E. Gratton and D. Lamb, *ChemPhysChem*, 2009, **10**, 2458–2464.
- 27 J. Rudnick and G. Gaspari, *Science*, 1987, **237**, 384–9.
- 28 T. Mason and D. Weitz, *Phys. Rev. Lett.*, 1995, **74**, 1250–1253.
- 29 G. Guigas, C. Kalla and M. Weiss, *FEBS Lett.*, 2007, **581**, 5094–98.
- 30 G. Guigas and M. Weiss, *Biophys. J.*, 2008, **94**, 90–94.

Fractional Brownian Motion in Crowded Fluids – Supplement

Dominique Ernst¹, Marcel Hellmann², Jürgen Köhler¹, and Matthias Weiss²

¹ *Experimental Physics IV, University of Bayreuth, D-95440 Bayreuth, Germany and*

² *Experimental Physics I, University of Bayreuth, D-95440 Bayreuth, Germany*

I. EXPERIMENTAL APPROACH

Fluids for SPT experiments were obtained by dissolving dextran (500 kDa, Sigma) and sucrose (342 Da, Roth) in millipore water at concentrations of about 430 mg/ml (30% w/w) and 1500 mg/ml (60% w/w), respectively. Rhodamine-tagged tracer beads (50 nm, Polysciences) were added from a predissolved solution, resulting in a typical concentration of about 2 pM. Hence, 3-5 beads were observed in the focal plane of the microscope's widefield image ($80 \times 80 \mu\text{m}^2$).

About 35 μl of each sample was placed between acetone-cleaned coverslips and sealed on the edges with highly viscous grease to prevent evaporation or adhesion forces that would induce a flow field.

Tracking experiments were performed with a home-built single-particle tracking setup (Fig. 1) using a novel tracking technique [1–5]. Here we only describe the basic concept, technical details will be presented elsewhere.

The output of an Ar/Kr-Ion laser (Innova 70C Spectrum, Coherent) at a wavelength of 514nm with a circular polarisation (due to a $\lambda/4$ -waveplate) was used as an excitation light source. The laser beam was directed through a series of two perpendicularly arranged acousto optical deflectors (AOD, DTSX-400-532, Pegasus), responsible for the generation of an orbiting laser beam with rotation frequency f . The rotating laser beam was then passed through a telecentric lens system and directed into a home-built confocal microscope. The laser light was reflected by a dichroic beamsplitter (z532RDC, AHF) towards an infinity corrected water-immersion objective (UPLSAPO, 60x, NA=1.2, Olympus). The sample with the diffusing tracer particles was mounted on top of a three-dimensional piezo stage. This setup allowed us to create an orbit radius R in the range of 0 to $5 \mu\text{m}$ in the focal plane of the objective. Suitable dye-labeled particles in the vicinity of the rotating focal spot were excited. The emitted light was collected by the same objective, passed the dichroic beamsplitter and a further dielectric filter (HQ525LP, OD=6 @ 514nm, AHF) to suppress remaining laser light. Finally it was focussed either onto the chip of a CCD (sencam qe, PCO) or an avalanche photodiode (APD, SPCM-AQR-14, Perkin Elmer) with a sensitive area of $180 \mu\text{m}$ in diameter.

The setup was capable of working in a widefield and a confocal operation mode. For the widefield mode an optional lens in front of the microscope was flipped into the optical path to defocus the excitation to an area of about $80 \times 80 \mu\text{m}^2$ in the plane of the sample. In this mode the deflection unit is set to a neutral state (no deflection). The diffusing particles are located within the

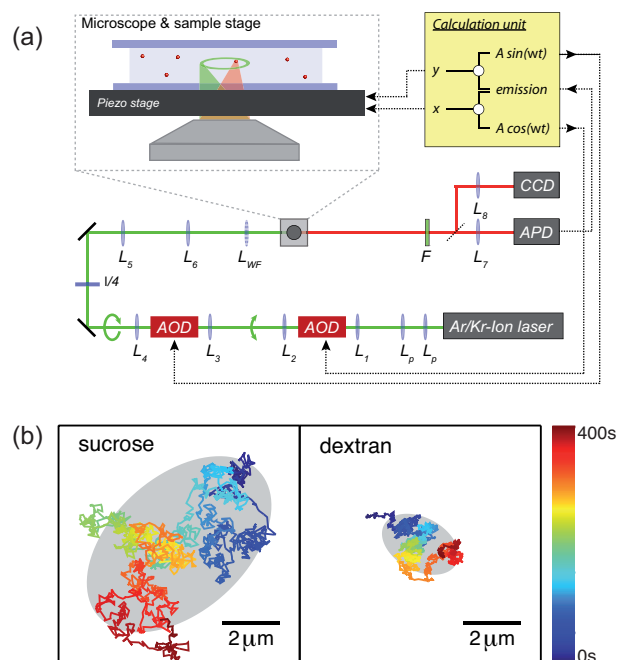


FIG. 1: (a) Sketch of the experimental setup with lenses for beam profile optimization (L_p), a widefield lens (L_{WF}), a dielectric filter (F), and an acousto optical deflector (AOD). Signals were collected either with a CCD camera or an avalanche photodiode (APD). The calculation unit provided the drive signals for the AODs, gathered the emission intensity, calculated the positions x and y , and fed the negated position to a piezo stage. (b) Representative trajectories in a purely viscous sucrose solution (left) and a crowded dextran fluid (right); color-coding blue to red highlights the temporal direction of the trajectory. The gyration ellipsoids which reflect the random walks' asphericity are superimposed in grey. Due to a higher mobility in the sucrose solution, the ellipsoids differ in size.

CCD image and are moved by the piezo stage to a proper position near the centre of the laser orbit. The confocal mode is subsequently used to perform the measurements. By flipping the optional lens back, the emission is now detected with the APD and the deflection unit is switched on. The emission intensity of the moving particle is modulated with the known frequency of the laser orbit.

Using a tracking software based on a lock-in technique [1, 3] we were able to reconstruct the two-dimensional motion of particles from the frequency-modulated fluorescence signal: From the detected photons the position with respect to the orbit center was calculated, and the piezo stage was fed with a signal corresponding to the

negated position. The whole trajectory of the tracer can be reconstructed by monitoring the feedback signal of the piezo.

Experiments were done with an orbit frequency of $f = 1\text{ kHz}$. Every four periods of rotation the position was calculated resulting in a time resolution of $\Delta t = 4\text{ ms}$. The radius for best tracking performance depends on the beam waist w of the focal spot and was found to be $R = w/\sqrt{2}$ [6]. A typical width of $w = 270\text{ nm}$ lead to a radius of $R = 190\text{ nm}$.

II. EVALUATION WINDOW OF EXPERIMENTAL DATA

We have chosen to evaluate the scaling properties of the experimental data in the temporal range 50-500ms, e.g. when inspecting the MSD. Enlarging the window in which the anomaly α and the corresponding asphericity A were determined will alter the stated numbers. Extending the fit range to larger times will include more of the crossover towards the asymptotic normal diffusion and hence $\alpha \rightarrow 1$ and $A \rightarrow 4/7$. This underlines the transient nature of the anomaly. In better words, significant elastic restoring forces are only present in crowded fluids for large frequencies, i.e. for rapid motion on short length and time scales.

Extending the fit range to smaller times will include particular features of the measurement process. The accuracy of the position measurement in SPT depends on the number of photons acquired. If too few photons are detected, small diffusion steps are masked by noise and the MSD appears to converge to a constant for $t \rightarrow 0$ [7, 8]. This behavior may mimic a subdiffusive characteristics at small times ('false positives'). In our experiments photon statistics was sufficiently high to make this effect negligible, i.e. the scaling exponent of a purely viscous fluid deviated from unity only by less than 2%. But even when having enough photon statistics and normal diffusion, an apparently anomalous characteristics may emerge: Since diffusion does not stop during the acquisition process (given by the acquisition time Δt), the MSD will take on a form $\langle r(t)^2 \rangle = 4D(t - \Delta t/3)$ [9]. Due to the subtraction of a constant, the MSD hence may mimic a superdiffusive scaling for short times. To avoid all these contributions, we have restricted ourselves to the indicated fit window which is least affected by the above mentioned processes.

From the two-dimensional trajectory with N position and a time resolution of Δt , we obtained the gyration tensor via

$$T_{ij} = \frac{1}{N} \sum_{n=1}^N (r_i(n\Delta t) - \langle r_i \rangle) (r_j(n\Delta t) - \langle r_j \rangle). \quad (1)$$

Here, $\langle r_i \rangle$ denotes the i -th component of the center of mass. Diagonalizing T_{ij} yields the principal axes of gyration and the corresponding eigenvalues, i.e. the squared principal radii of gyration, R_i^2 .

III. SIMULATIONS

We have considered two different models for anomalous diffusion, namely diffusion in a percolation system (obstructed diffusion, OD) and fractional Brownian motion (FBM). Computer simulations of the respective process provide numerical values for the shape parameters that can be compared to experimental data.

Obstructed diffusion was simulated on a square lattice (350×350 sites) with periodic boundary conditions. A fixed fraction f of randomly chosen sites were occupied by static obstacles and tracer particles were allowed to move on the remaining free sites according to the blind ant algorithm (see, e.g. [10]). Depending on the occupied volume fraction f , the support becomes a fractal [11], and diffusion can become (transiently) anomalous. For a critical concentration of obstacles $f_p = 0.40726$ [12], the *percolation threshold* in two dimensions, subdiffusion with $\alpha \approx 0.69$ is observed on all time scales whereas for $f < f_p$ a transient, yet long-lasting subdiffusion with a finite-size corrected anomaly α emerges. Indeed, for $f < f_p$ normal diffusion is asymptotically restored. For $f > f_p$, tracers are confined to finite domains, i.e. an initial subdiffusion is observed but asymptotically the particle is bound to a certain region in space. In our simulations, we varied the occupied volume fraction in the range $0.33 \leq f \leq 0.42$ which resulted in straight power laws of the particles' MSD within the simulation period. For every value of f , we simulated 1.5×10^6 random walks, where for every 1000th run a new environment was created. Each random walk was started at a randomly chosen vacant site. Occasionally, particles were trapped in a small subvolume of the lattice due to the random placement of obstacles. We identified such situations and removed trapped trajectories from the analysis.

For the simulation of FBM we used the circulant method [13] which is in principle exact, i.e. the deviations between 'true' and simulated FBM are due to computational limitations like finite numerical accuracy. The method relies on the embedding of the covariance matrix of FBM into a circulant matrix that is diagonalized by a discrete Fourier transform. Using a fast Fourier transform (FFT), the simulation time for a trajectory of length N scales as $N \log N$. We generated 10^6 independent trajectories, each having $N = 2^{13}$ positions. The anomaly was varied in the range $0.5 \leq \alpha \leq 0.9$. For normal diffusion ($\alpha = 1$), we relied on Brownian Dynamics simulations [14] that are based on the overdamped Langevin equation, $\mathbf{r}(t + \Delta t) = \mathbf{r}(t) + \xi(\Delta t)$ with ξ being a random variable with white noise characteristics.

IV. RESULTS ON A TRUNCATED CTRW MODEL

To overcome the somewhat artificial features of the CTRW model due to its asymptotic scaling of the distribution of waiting times, $p(\tau) \sim 1/\tau^{1+\alpha}$, we have con-

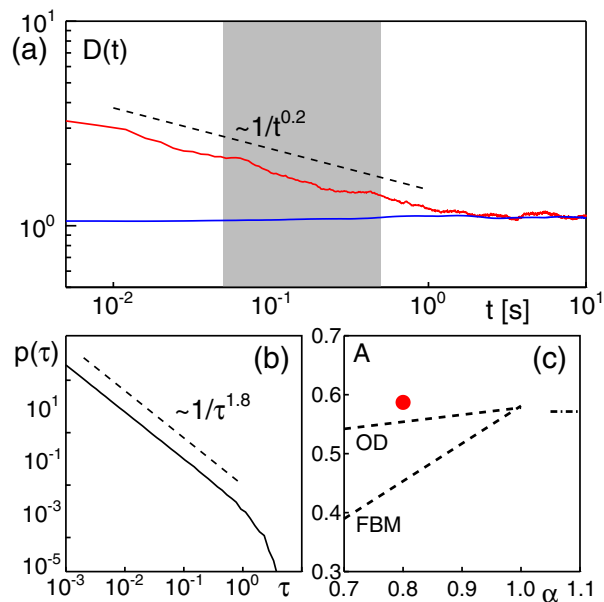


FIG. 2: (a) Representative time-averaged MSD of truncated CTRW model ($\alpha = 0.8$), shown as $D(t) = \langle r(t)^2 \rangle / t$ to highlight the asymptotic scaling. Data for the time- and ensemble-averaged MSD are shown in blue and red, respectively. For the ensemble-averaged quantity a transient scaling $D(t) \sim 1/t^{0.2}$ in the experimentally relevant interval is observed before asymptotically reaching the normal diffusion limit ($D \rightarrow \text{const.}$). Hence, the truncated CTRW model only shows transiently a weak ergodicity breaking. (b) The probability distribution function of waiting times, $p(\tau)$ used for the truncated CTRW model. After a transient power-law scaling, the distribution displays an exponential tail that enforces an asymptotic convergence of the MSD to normal diffusion. (c) The asphericity of the truncated CTRW model for $\alpha = 0.8$ (red dot) deviates considerably from the predictions of the OD and FBM models (dashed lines). It is most consistent with the limiting value $A = 4/7$ for normal diffusion and hence incompatible with the experimental data found for a crowded dextran solution.

structured a truncated CTRW model. In particular, we followed previous reports that had implied exponentially truncated power-law distributions [15]. A truncated $p(\tau)$ is expected to yield a long-lasting transient subdiffusion which asymptotically converges to normal diffusion.

We therefore have simulated a two-dimensional CTRW with $\alpha = 0.8$ and a truncated distribution of waiting times with parameters that yielded a close match with the experimental MSD data. The chosen waiting time distribution and the resulting behavior of the MSD (again shown as $D(t) = \langle r(t)^2 \rangle / t$) are reported in Fig. 2. As can be seen in Fig. 2a, the time-averaged $D(t)$ is approximately constant whereas the ensemble-averaged quantity shows a transient scaling $\sim 1/t^{0.2}$ (i.e. $\langle r(t)^2 \rangle_E \sim t^{0.8}$) before converging to the asymptotic limit of normal diffusion. Hence, the CTRW's feature of a linear scaling of the time-averaged MSD persists even for the truncated model. The associated waiting time distribution (Fig. 2b) shows a power-law decay over several orders of magnitude before being exponentially truncated.

We next determined the asphericity for the truncated CTRW model. Since the trajectory of a CTRW at any instance of time geometrically looks like the path of normal Brownian motion, we expected a value $A \approx 4/7$ for the truncated CTRW model. Indeed, our expectation turned out to be correct (Fig. 2c). Furthermore, A did not change significantly with the imposed anomaly α (data not shown). Shifting the truncation to larger and larger times resulted in a slight increase of A rather than reducing the value. Therefore, based on the scaling of $\langle r(t)^2 \rangle_T$ and the asphericity, we can not only rule out OD and the full CTRW model but also a (truncated) CTRW model as an explanation of the experimentally observed anomalous diffusion.

-
- [1] J. Enderlein, Appl. Phys. B **71**, 773 (2000).
 [2] J. Enderlein, Single Mol. **1**, 225 (2000).
 [3] K. Kis-Petikova and E. Gratton, Microsc. Res. Tech. **63**, 34 (2004).
 [4] K. McHale, A. J. Berglund, and H. Mabuchi, Nano Lett. **7**, 3535 (2007).
 [5] A. Berglund and H. Mabuchi, Appl. Phys. B **78**, 653 (2004).
 [6] A. Berglund and H. Mabuchi, Appl. Phys. B **83**, 127 (2006).
 [7] D. Martin, M. Forstner, and J. Kas, Biophys. J. **83**, 2109 (2002).
 [8] M. Hellmann, D. Heermann, and M. Weiss, EPL **94**, 18002 (2011).
 [9] M. Goulian and S. Simon, Biophys. J. **79**, 2188 (2000).
 [10] M. Saxton, Biophys. J. **66**, 394 (1994).
 [11] S. Havlin and D. Ben-Avraham, Adv. Phys. **36**, 695 (1987).
 [12] M. Newman and R. Ziff, Phys. Rev. Lett. **85**, 4104+ (2000).
 [13] A. Wood and G. Chan, J. Comp. Graph. Stat. **3**, 409 (1994).
 [14] D. Ermak, J. Chem. Phys. **62**, 4189 (1975).
 [15] C. Gonzalez, MC and Hidalgo and A. Barabasi, Nature **453**, 779 (2008).